

2

AD-A221 034

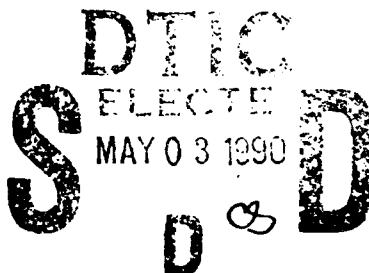
WRDC-TR-90-3007

LOW-DENSITY FLOW EFFECTS FOR HYPERVELOCITY
VEHICLES (PHASE II)



ROOP N. GUPTA
SCIENTIFIC RESEARCH & TECHNOLOGY, INC.
109 LAKE HERRIN CT.
TABB, VA 23602

SUDHEER N. NAYANI
VIGYAN, INC.
30 RESEARCH DRIVE
HAMPTON, VA 23666



MARCH 1990

FINAL REPORT FOR PERIOD JAN 1988 - DEC 1989

Approved for public release; distribution unlimited.

FLIGHT DYNAMICS LABORATORY
WRIGHT RESEARCH DEVELOPMENT CENTER
AIR FORCE SYSTEMS COMMAND
WRIGHT-PATTERSON AIR FORCE BASE, OHIO 45433-6553

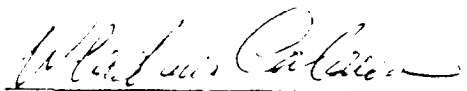
90 05 02 037

NOTICE

WHEN GOVERNMENT DRAWINGS, SPECIFICATIONS, OR OTHER DATA ARE USED FOR ANY PURPOSE OTHER THAN IN CONNECTION WITH A DEFINITELY GOVERNMENT-RELATED PROCUREMENT, THE UNITED STATES GOVERNMENT INCURS NO RESPONSIBILITY OR ANY OBLIGATION WHATSOEVER. THE FACT THAT THE GOVERNMENT MAY HAVE FORMULATED OR IN ANY WAY SUPPLIED THE SAID DRAWINGS, SPECIFICATIONS, OR OTHER DATA, IS NOT TO BE REGARDED BY IMPLICATION, OR OTHERWISE IN ANY MANNER CONSTRUED, AS LICENSING THE HOLDER, OR ANY OTHER PERSON OR CORPORATION; OR AS CONVEYING ANY RIGHTS OR PERMISSION TO MANUFACTURE, USE, OR SELL ANY PATENTED INVENTION THAT MAY IN ANY WAY BE RELATED THERETO.

THIS REPORT HAS BEEN REVIEWED BY THE OFFICE OF PUBLIC AFFAIRS (ASD/PA) AND IS RELEASABLE TO THE NATIONAL TECHNICAL INFORMATION SERVICE (NTIS). AT NTIS IT WILL BE AVAILABLE TO THE GENERAL PUBLIC INCLUDING FOREIGN NATIONS.

THIS TECHNICAL REPORT HAS BEEN REVIEWED AND IS APPROVED FOR PUBLICATION.

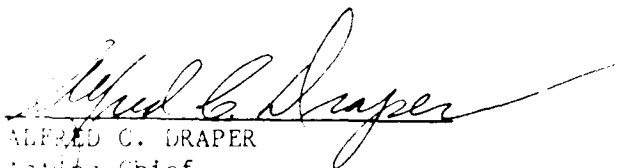


WLADIMIRO CALARESE
Project Engineer



VALENTINE DAHLEM, Chief
High Speed Aero Performance Branch
Aeromechanics Division

FOR THE COMMANDER



ALFRED C. DRAPER
Acting Chief
Aeromechanics Division

IF YOUR ADDRESS HAS CHANGED, IF YOU WISH TO BE REMOVED FROM OUR MAILING LIST, OR IF THE ADDRESSEE IS NO LONGER EMPLOYED BY YOUR ORGANIZATION PLEASE NOTIFY WRDC/ELMG, WRIGHT-PATTERSON AFB, OH 45433-6553 TO HELP MAINTAIN A CURRENT MAILING LIST.

COPIES OF THIS REPORT SHOULD NOT BE RETURNED UNLESS RETURN IS REQUIRED BY SECURITY CONSIDERATIONS, CONTRACTUAL OBLIGATIONS, OR NOTICE ON A SPECIFIC DOCUMENT.

Unclassified

SECURITY CLASSIFICATION OF THIS PAGE

REPORT DOCUMENTATION PAGE				Form Approved OMR No 0704 0188	
1a REPORT SECURITY CLASSIFICATION Unclassified			1b RESTRICTIVE MARKINGS		
2a SECURITY CLASSIFICATION AUTHORITY			3 DISTRIBUTION/AVAILABILITY OF REPORT Approved for Public Release; Distribution unlimited		
2b DECLASSIFICATION/DOWNGRADING SCHEDULE					
4 PERFORMING ORGANIZATION REPORT NUMBER(S)			5 MONITORING ORGANIZATION REPORT NUMBER(S) WRDC-TR-90-3007		
6a NAME OF PERFORMING ORGANIZATIONS 1. Scientific Res. & Tech., Inc. 2. Vigyan, Inc.		6b OFFICE SYMBOL (If applicable)		7a NAME OF MONITORING ORGANIZATION Flight Dynamics Laboratory (WRDC/FIMG) Wright Research and Development Center	
6c ADDRESS (City, State, and ZIP Code) 1. 109 Lake Herrin Ct., Tabb, VA 23602 2. 30 Research Drive, Hampton, VA 23666		7b ADDRESS (City, State, and ZIP Code) Wright-Patterson Air Force Base OH 45433-6553			
8a NAME OF FUNDING/SPONSORING ORGANIZATION		8b OFFICE SYMBOL (If applicable)		9 PROCUREMENT INSTRUMENT IDENTIFICATION NUMBER F33615-87-C-3020	
8c ADDRESS (City, State, and ZIP Code)		10 SOURCE OF FUNDING NUMBERS			
		PROGRAM ELEMENT NO 65502F		PROJECT NO 3005	TASK NO 40
				WORK UNIT ACCESSION NO 10	
11 TITLE (Include Security Classification) Low Density Flow Effects For Hypervelocity Vehicles (Phase II)					
12 PERSONAL AUTHOR(S) Roop N. Gupta, Sudheer N. Nayani					
13a TYPE OF REPORT Final		13b TIME COVERED FROM Jan 88 to Dec 89		14 DATE OF REPORT (Year, Month, Day) 1990, March 2	
15 PAGE COUNT 87					
16 SUPPLEMENTARY NOTATION This is a Small Business Innovative Research Program, Phase II report.					
17 COSATI CODES			18 SUBJECT TERMS (Continue on reverse if necessary and identify by block number)		
FIELD	GROUP	SUB-GROUP	Hypervelocity Vehicles; Low Density Flow Fields; Viscous Shock Layer Equations;		
0101	2004	2013			
19 ABSTRACT (Continue on reverse if necessary and identify by block number) Detailed flowfield results have been obtained for sphere-cone shaped bodies at various angles of attack with a 3D nonequilibrium viscous-shock-layer code. Recently obtained surface and shock-slip boundary conditions are implemented to account for the low-density effects. These boundary conditions may also be employed with the Navier-Stokes equations with or without a shock-fitting solution technique. A method is suggested for obtaining the input shock shape for the 3D nonequilibrium viscous flow. This approach gives a superior convergence of results, especially under the low-density flow conditions and makes the VSL method self-starting. The analytic algebraic grid implemented with the equations does not add any numerical dissipation. Obtained results show the effect of low density on the surrounding flowfield and surface quantities for a hypervelocity vehicle. Good agreement is obtained with the available numerical results (including the Direct Simulation Monte-Carlo predictions) and experimental data for the low-density flight conditions.					
20 DISTRIBUTION/AVAILABILITY OF ABSTRACT <input checked="" type="checkbox"/> UNCLASSIFIED/UNLIMITED <input type="checkbox"/> SAME AS RPT. <input type="checkbox"/> DTIC USERS			21 ABSTRACT SECURITY CLASSIFICATION Unclassified		
22a NAME OF RESPONSIBLE INDIVIDUAL Wladimiro Calarese			22b TELEPHONE (Include Area Code) (513) 255-2052		22c OFFICE SYMBOL WRDC/FIMG

Acknowledgment

The authors would like to express their sincere appreciation to Mr. R. A. Thompson of NASA Langley Research Center. Without his help on numerous occasions, this work could not have been completed in the present form. We are also grateful to Dr. W. Calarese of WRDC, Wright-Patterson Air Force Base, Ohio for sharing his technical expertise on various occasions and for providing constant inspiration which made this work more rewarding. This work has been supported by U. S. Air Force Contract No. F33615-87-C-3020. Dr. Calarese served as the Technical Monitor for this project.

NBS		<input checked="" type="checkbox"/>
OASD		<input type="checkbox"/>
DAS		<input type="checkbox"/>
J-1		
By		
Date		
Title		
Dist		
A-1		



Table of Contents

	<u>Page</u>
Introduction	1
Analysis	3
Governing Equations	4
Boundary Conditions	11
Chemical Reaction Model	18
Thermodynamic and Transport Properties	18
Method of Solution	19
Calculation of Input Shock Shape	22
Surface Quantities	24
Results and Discussion	25
Concluding Remarks	31
References	33
Figures	40

Nomenclature

A_n	Coefficient of model parabolic equation, $n=0,1,\dots,5$
C_i	mass fraction of species i , ρ_i^*/ρ^*
C_{F_ξ}	skin-friction coefficient in the streamwise direction, $2\tau_\xi^*/\rho_\infty^*U_\infty^{*2}$
C_{F_ζ}	skin-friction coefficient in the cross-flow direction, $2\tau_\zeta^*/\rho_\infty^*U_\infty^{*2}$
C_H	heat-transfer coefficient, $2q_w^*/\rho_\infty^*U_\infty^{*3}$
\tilde{C}_p	pressure coefficient, $2p^*/\rho_\infty^*U_\infty^{*2}$
C_p	frozen specific heat of mixture, $\sum_i C_i C_{p,i}$
$C_{p,i}$	specific heat of species i , $C_{p,i}^*/C_{p,\infty}^*$
D_{ij}^*	binary diffusion coefficient
$\hat{e}_x, \hat{e}_r, \hat{e}_\phi$	unit vectors along x, r, ϕ
g	stretching function
H	stagnation enthalpy, H^*/U_∞^{*2}
h	mixture enthalpy, $\sum_i C_i h_i$
h_1, h_2, h_3	scale factors for a surface-normal coordinate system
h_i	enthalpy of species i , h_i^*/U_∞^{*2}
k_w^*	surface catalytic recombination rate
K	thermal conductivity of mixture, $K^*/\mu_{ref}^* C_{p,\infty}^*$
Le_i	Lewis number, $\rho^* D_{ij}^* C_i^*/K^*$
M_∞	freestream Mach number
n_{sh}	shock standoff distance, n_{sh}^*/R_N^*
\hat{N}	vector normal to the shock surface (figs. 2a and 2b)
NS	number of reacting species
p	pressure, $p^*/\rho_\infty^*U_\infty^{*2}$

Pr	Prandtl number, $\mu^* C_p^* / K^*$
q_w	wall heat-transfer rate, $q_w^* / \rho_\infty^* U_\infty^{*3}$
Re_∞	Reynolds number, $\rho_\infty^* U_\infty^* R_N^* / \mu_\infty^*$
R_N^*	nose radius
s, n, ϕ	nondimensional surface-oriented coordinate system (fig. 1), $s = s^* / R_N^*$, $n = n^* / R_N^*$, $\phi \equiv \phi$ in deg
St	Stanton number
T	temperature, T^* / T_{ref}^*
\hat{T}	vector tangent to the bow shock (figs. 2a and 2b)
T_{ref}^*	reference temperature, $U_\infty^{*2} / C_{p,\infty}^*$
u, v, w	streamwise, normal and crossflow velocity components nondimensionalized by the freestream velocity
U_∞^*	freestream velocity
W	dependent variable
W_i	molecular weight of species i
\bar{W}	molecular weight of mixture
\dot{w}_i	mass rate of formation of species i , $\dot{w}_i^* R_N^* / \rho_\infty^* U_\infty^*$
x^*	axial distance from blunt nose (body axis)
x^*, r^*, θ	cylindrical coordinates
α	angle of attack
$\bar{\alpha}$	mesh refinement parameter
β	shock angle in meridional plane (fig. 1)
$\bar{\beta}$	mesh refinement parameter
β_{sh}	angle between the components of freestream velocity and the total velocity behind the shock in meridional plane (fig. 2c)
ϕ	crossflow-plane or azimuthal angle measured from windward plane
γ_i	catalytic recombination coefficient

$\bar{\gamma}$	ratio of specific heats, C_p^*/C_v^*
δ_{sh}	shock thickness
ϵ	Reynolds number parameter, $\epsilon^2 = \mu_{ref}^*/\rho_\infty^* U_\infty^* R_N^*$
ξ, η, ζ	transformed surface-oriented coordinates, $\xi \equiv s$, $\eta = g(\bar{\eta})$, $\zeta \equiv \phi$
\bar{n}	normalized surface-normal coordinate, n/n_{sh}
κ_ξ, κ_ζ	body curvature in streamwise and crossflow direction, $\kappa_\xi = \kappa_\xi^* R_N^*$, $\kappa_\zeta = \kappa_\zeta^* R_N^*$
μ_{ref}^*	reference viscosity, $\mu^*(T_{ref}^*)$
ρ	density, ρ^*/ρ_∞^*
ψ	source term (Eq. 15)
σ'	angle between the freestream velocity vector and \hat{T} (fig. 2b)
τ_ξ, τ_ϕ	shear stress in the streamwise and crossflow direction
θ	accommodation coefficient
θ_ξ	body angle in the streamwise direction
θ_2	angle by which the streamline is turned in crossing the shock (fig. 2b)
$\Delta\xi, \Delta\phi$	stepsizes in the streamwise and crossflow directions

Subscripts

aw	adiabatic wall condition
body	coordinate system with origin at the geometric stagnation point
B	body value
i	ith species
ref	reference conditions
ξ, η, ζ	streamwise, normal and crossflow directions
s	Knudsen-layer edge value
sh	shock value

TP	tangency point
w	wall value
wind	coordinate system with origin at the aerodynamic stagnation point
x, r, ϕ	cylindrical coordinate directions
∞	freestream condition

Superscripts

'	derivative with respect to ξ
*	dimensional quantity
-	normalized variable
~	shock-oriented velocity components
^	vector quantity
s	Knudsen-layer edge value

Abbreviations

DSMC	Direct Simulation Monte-Carlo
VSL	viscous shock layer
VSL2DNQ	two-dimensional nonequilibrium viscous shock layer
VSL3DNQ	three-dimensional nonequilibrium viscous shock layer
2D	two-dimensional
3D	three-dimensional

INTRODUCTION

The recently increased interest in space for civilian and defense purposes has resulted in new concepts for the hypersonic vehicles. Since most of the currently planned and future hypersonic vehicles will be operating in the upper atmosphere, the 'low density effects' will play a major role in establishing the lift, drag, moments, and aerodynamic heating of a hypersonic vehicle. In phase I of this study, these low density effects were analyzed for axially symmetric flows. These effects, generally referred to as the surface- and shock-slip boundary conditions, were incorporated into a newly developed viscous shock-layer perfect-gas code. The results obtained from this code were quite accurate and compared well with the experimental data. Phase II work is intended to analyze the low-density flow effects for bodies at angle of attack with finite-rate chemistry in the flowfield.

Tree, et al.,¹ included the low-density effects in analyzing the hypersonic ionizing viscous shock-layer flow past axially symmetric bodies. This analysis was limited to an equilibrium catalytic wall and contained the errors of reference 2 (as explained in reference 3) in the specification of surface slip boundary conditions. The shock-slip boundary condition also did not account for the derivatives of the shock quantities in the shock-oriented coordinate system among other errors. This introduces errors in analyzing flows past slender bodies. Swaminathan, et al.,⁴ and Song, et al.,⁵ have considered the surface- and shock-slip effects for the three-dimensional flows. Their shock-slip formulation contains the error mentioned earlier, whereas their surface-slip model is taken from reference 6, which also contains errors as explained in reference 3. Further, the frozen-flow approximation employed in the shock-slip boundary conditions of references 4

and 5 is not a very physically appealing approximation for a thick shock under the low density conditions, where the characteristic flow times are large enough to initiate chemical activity through the shock. Unlike references 5 and 6, it is also desirable to solve the flowfield equations with equal step sizes in the computational plane to keep the same order of accuracy for the computed results. Finally, to make the computer code robust and to speed up global convergence, the input shock shape for the low-density nonequilibrium viscous shock-layer calculations should be obtained from a corresponding approximate flowfield calculation in place of using an equilibrium shock shape.^{4,5} Thus, there is a need to develop an accurate and robust viscous shock-layer code for the three-dimensional flows with nonequilibrium chemistry and physically realistic surface and shock-slip boundary conditions for a wide range of flow conditions.

Present work was undertaken to study the low-density, nonequilibrium three-dimensional flowfields around axially-symmetric bodies at angle of attack. This study was carried out to develop a viscous shock-layer code with the recently obtained surface- and shock-slip boundary conditions. The results are obtained with an analytic grid built into the equations with zero numerical dissipation of its own. Latest transport properties are employed for the air species with appropriate mixing laws for the ionized mixture. Detailed comparison is made with other numerical predictions (including the Direct Simulation Monte-Carlo results) and the available flight data. There are not enough data available for the three-dimensional nonequilibrium flow, especially under the low-density conditions.

ANALYSIS

Since its first application by Davis,² the viscous-shock-layer (VSL) flow model has been extensively used for numerical solution of hypersonic flows over bodies for a range of body shapes and freestream conditions. Because of the simplicity of VSL technique with the capability of modeling fairly detailed flowfield physics, many physical models have been incorporated into VSL codes for a variety of flow problems and detailed flowfield calculations. Applications of VSL codes include predictions of flowfields around planetary entry bodies with massive ablation and radiation,⁷ transitional and turbulent flows over slender vehicles,^{8,9} and flows with nonequilibrium chemistry around complex reentry vehicles.¹⁰ The VSL technique is quite attractive because of the computational advantage it offers. The viscous shock-layer equations are obtained from the steady-state Navier-Stokes equations by keeping terms up to second-order in the inverse square root of the Reynolds number ϵ . Consequently, one set of equations is solved for both the inviscid and viscous regions. Further, parabolic approximations are made in the streamwise direction. In the case of a three-dimensional flow, the crossflow momentum equation is also parabolized. Thus, the equations can be solved in both the streamwise and crossflow directions by marching techniques which are efficient in terms of computer time and storage requirements. The equations are limited, however, to attached flows, in both streamwise and crossflow directions, unlike some higher order approximations.

A 3D nonequilibrium VSL code was originally developed in reference 10. Subsequent study¹¹ indicated the need for modifications and corrections. The modified version of reference 11 serves as the basis for this study.

Governing Equations

The viscous shock-layer equations for a reacting multi-component gas mixture are obtained from the basic conservation equations^{12,13} by the method mentioned earlier. These equations in the orthogonal, body-oriented transformed coordinates (fig. 1) and normalized form are provided here. Most of the flowfield variables are normalized with their local shock values to keep them of the order of one. The normal coordinate is normalized with the local shock stand-off distance to obtain a constant number of grid points between the body and shock. The second-order partial differential equations, namely, ξ (or s)-momentum, ζ (or ϕ)-momentum, energy, and the species continuity equations are written in the following form:

$$\begin{aligned} \frac{\partial^2 W}{\partial \bar{n}^2} + \frac{(A_0 \partial^2 g / \partial \bar{n}^2 + A_1 \partial g / \partial \bar{n})}{A_0 (\partial g / \partial \bar{n})^2} \frac{\partial W}{\partial \bar{n}} + \frac{A_2}{A_0 (\partial g / \partial \bar{n})^2} + \frac{A_3}{A_0 (\partial g / \partial \bar{n})^2} \\ + \frac{A_4}{A_0 (\partial g / \partial \bar{n})^2} \frac{\partial W}{\partial \xi} + \frac{A_5}{A_0 (\partial g / \partial \bar{n})^2} \frac{\partial W}{\partial \zeta} = 0 \end{aligned} \quad (1)$$

where $(\partial g / \partial \bar{n})$ and $\partial^2 g / \partial \bar{n}^2$ are the first and second derivatives of the stretching function $g(\bar{n})$. The quantity W represents \bar{u} in the ξ -momentum equation, w in the ζ -momentum equation, T in the energy equation, and C_i in the species continuity equation. The coefficients A_0 to A_5 are written as follows:

ξ -momentum, $W = \bar{u}$:

$$A_0 = - \frac{\epsilon^2 \mu_{sh} \bar{\mu}}{n_{sh}^2} \quad (2a)$$

$$\begin{aligned}
A_1 = & -\frac{\epsilon^2 \mu_{sh}}{n_{sh}^2} \frac{\partial \bar{\mu}}{\partial \eta} \frac{\partial g}{\partial \eta} - \frac{\epsilon^2 \mu_{sh} \bar{\mu}}{n_{sh}^2} \frac{1}{h_1} \frac{\partial h_1}{\partial \eta} - \frac{\rho_{sh} u_{sh} \bar{\rho} \bar{u} \bar{n}}{h_1 n_{sh}} \frac{\partial n_{sh}}{\partial \xi} \\
& + \frac{\rho_{sh} \bar{\rho}}{n_{sh}} v - \frac{\rho_{sh} \bar{\rho} \bar{n} w}{h_3} \frac{\partial n_{sh}}{\partial \zeta} - \epsilon^2 \frac{\mu_{sh} \bar{\mu}}{h_3 n_{sh}^2} \frac{\partial h_3}{\partial \eta}
\end{aligned} \quad (2b)$$

$$\begin{aligned}
A_2 = & \frac{\rho_{sh} \bar{\rho} \bar{u}}{h_1} \frac{\partial u_{sh}}{\partial \xi} + \frac{\rho_{sh} \bar{\rho} w}{h_3 u_{sh}} \frac{\partial u_{sh}}{\partial \zeta} + \frac{\rho_{sh} \bar{\rho} v}{h_1 n_{sh}} \frac{\partial h_1}{\partial \eta} + \frac{\rho_{sh} \bar{\rho} w}{h_1 h_3} \frac{\partial h_1}{\partial \zeta} \\
& - \frac{\rho_{sh} \bar{\rho} w \bar{n}}{h_1 h_3 n_{sh}} \frac{\partial n_{sh}}{\partial \zeta} \frac{\partial h_1}{\partial \eta} + \epsilon^2 \frac{\mu_{sh}}{n_{sh}^2 h_1} \frac{\partial h_1}{\partial \eta} \frac{\partial \bar{\mu}}{\partial \eta} \frac{\partial g}{\partial \eta} \\
& + \epsilon^2 \frac{\mu_{sh}}{n_{sh}^2 h_1^2} \bar{\mu} \left(\frac{\partial h_1}{\partial \eta} \right)^2 + \epsilon^2 \frac{\mu_{sh} \bar{\mu}}{h_1 h_3 n_{sh}^2} \frac{\partial h_1}{\partial \eta} \frac{\partial h_3}{\partial \eta}
\end{aligned} \quad (2c)$$

$$\begin{aligned}
A_3 = & -\frac{\rho_{sh} \bar{\rho} w^2}{h_1 h_3 u_{sh}} \frac{\partial h_3}{\partial \xi} + \frac{\rho_{sh} \bar{\rho} \bar{n} w^2}{h_1 n_3 u_{sh} n_{sh}} \frac{\partial h_3}{\partial \eta} \frac{\partial n_{sh}}{\partial \xi} \\
& + \frac{1}{u_{sh}} \left(\bar{p} \frac{\partial p_{sh}/\partial \xi}{h_1} + \frac{p_{sh}}{h_1} \frac{\partial \bar{p}}{\partial \xi} - \frac{p_{sh} \bar{n}}{h_1 n_{sh}} \frac{\partial n_{sh}}{\partial \xi} \frac{\partial \bar{p}}{\partial \eta} \frac{\partial g}{\partial \eta} \right)
\end{aligned} \quad (2d)$$

$$A_4 = \rho_{sh} u_{sh} \bar{\rho} \bar{u}/h_1 \quad (2e)$$

$$A_5 = \rho_{sh} \bar{\rho} w/h_3 \quad (2f)$$

ζ -momentum: $W = w$

$$A_0 = -\epsilon^2 \frac{\mu_{sh} \bar{\mu}}{n_{sh}^2} \quad (3a)$$

$$\begin{aligned}
A_1 = & - \frac{\rho_{sh} u_{sh} \bar{\rho} \bar{u} \bar{\eta}}{n_{sh} h_1} \frac{\partial n_{sh}}{\partial \xi} + \frac{\rho_{sh} v \bar{\rho}}{n_{sh}} - \frac{\rho_{sh} \bar{\rho} \bar{\eta} w}{n_{sh} h_3} \frac{\partial n_{sh}}{\partial \zeta} - \epsilon^2 \frac{\mu_{sh}}{n_{sh}^2} \frac{\partial \bar{\mu}}{\partial \eta} \frac{\partial \bar{g}}{\partial \bar{\eta}} \\
& - \epsilon^2 \frac{\mu_{sh} \bar{\mu}}{h_3 n_{sh}^2} \frac{\partial h_3}{\partial \bar{\eta}} - \epsilon^2 \frac{\mu_{sh} \bar{\mu}}{n_{sh}^2 h_1} \frac{\partial h_1}{\partial \bar{\eta}}
\end{aligned} \quad (3b)$$

$$\begin{aligned}
A_2 = & \frac{\rho_{sh} u_{sh} \bar{\rho} \bar{u}}{h_1 h_3} \frac{\partial h_3}{\partial \xi} - \frac{\rho_{sh} u_{sh} \bar{\rho} \bar{u} \bar{\eta}}{h_1 h_3 n_{sh}} \frac{\partial n_{sh}}{\partial \xi} \frac{\partial h_3}{\partial \bar{\eta}} + \frac{\rho_{sh} v \bar{\rho}}{h_3 n_{sh}} \frac{\partial h_3}{\partial \bar{\eta}} \\
& + \epsilon^2 \frac{\mu_{sh} \bar{\mu}}{n_{sh}^2 h_3^2} \left(\frac{\partial h_3}{\partial \bar{\eta}} \right)^2 + \epsilon^2 \frac{\mu_{sh}}{n_{sh}^2 h_3} \frac{\partial \bar{\mu}}{\partial \eta} \frac{\partial \bar{g}}{\partial \bar{\eta}} \frac{\partial h_3}{\partial \bar{\eta}} + \epsilon^2 \frac{\mu_{sh} \bar{\mu}}{n_{sh}^2 h_1 h_3} \frac{\partial h_1}{\partial \bar{\eta}} \frac{\partial h_3}{\partial \bar{\eta}}
\end{aligned} \quad (3c)$$

$$\begin{aligned}
A_3 = & - \frac{\rho_{sh} u_{sh}^2 \bar{\rho} \bar{u}^2}{h_1 h_3} \frac{\partial h_1}{\partial \zeta} + \frac{\rho_{sh} u_{sh}^2 \bar{\rho} \bar{u}^2}{n_{sh} h_1 h_3} \bar{\eta} \frac{\partial n_{sh}}{\partial \rho} \frac{\partial h_1}{\partial \eta} + \frac{\partial \bar{p}}{\partial \zeta} \frac{p_{sh}}{h_3} \\
& - \frac{p_{sh} \bar{\eta}}{n_{sh} h_3} \frac{\partial n_{sh}}{\partial \zeta} \frac{\partial \bar{p}}{\partial \eta} \frac{\partial \bar{g}}{\partial \bar{\eta}}
\end{aligned} \quad (3d)$$

$$A_4 = \rho_{sh} u_{sh} \bar{\rho} \bar{u} / h_1 \quad (3e)$$

$$A_5 = \rho_{sh} \bar{\rho} w / h_3 \quad (3f)$$

Energy, $W = T$:

$$A_0 = - \epsilon^2 \frac{K_{sh}}{n_{sh}^2} \bar{K} \quad (4a)$$

$$\begin{aligned}
A_1 = & \frac{\rho_{sh} \bar{\rho} \bar{v} \bar{C}_p C_{p,sh}}{n_{sh}} - \frac{\rho_{sh} u_{sh} C_{p,sh} \bar{\rho} \bar{u} \bar{C}_p \bar{n}}{h_1 n_{sh}} \frac{\partial n_{sh}}{\partial \xi} \\
& - \frac{\rho_{sh} \bar{\rho} \bar{w} C_{p,sh} \bar{C}_p \bar{n}}{h_3 n_{sh}} \frac{\partial n_{sh}}{\partial \zeta} - \epsilon^2 \frac{k_{sh}}{n_{sh}} \frac{\partial K}{\partial \eta} \frac{\partial g}{\partial \bar{\eta}} - \epsilon^2 \frac{k_{sh}}{n_{sh}^2} \bar{K} \frac{\partial h_3}{\partial \bar{\eta}} \\
& - \epsilon^2 \frac{k_{sh}}{n_{sh}^2} \bar{K} \frac{\partial h_1}{\partial \bar{\eta}} - \epsilon^2 \frac{NS}{n_{sh}} \sum_{i=1} \frac{C_{p,i} \mu_{sh} \bar{\mu} Le_i}{n_{sh} Pr_{sh} \bar{Pr}} \frac{\partial C_i}{\partial \eta} \frac{\partial g}{\partial \bar{\eta}} \quad (4b)
\end{aligned}$$

$$A_2 = \dot{\bar{w}}_2 = \rho_{sh} \bar{\rho} \sum_{i=1}^{NS} h_i \left[\frac{\partial}{\partial T} \left(\frac{\dot{\bar{w}}_i}{\rho} \right) \right] \quad (4c)$$

$$\begin{aligned}
A_3 = & - \frac{p_{sh} u_{sh} \bar{u}}{h_1} \frac{\partial \bar{p}}{\partial \xi} - \frac{u_{sh} \bar{u} \bar{p}}{h_1} \frac{\partial p_{sh}}{\partial \xi} + \frac{p_{sh} u_{sh} \bar{u} \bar{n}}{n_{sh} h_1} \frac{\partial n_{sh}}{\partial \xi} \frac{\partial \bar{p}}{\partial \eta} \frac{\partial g}{\partial \bar{\eta}} \\
& - \frac{p_{sh} \bar{v}}{n_{sh}} \frac{\partial \bar{p}}{\partial \eta} \frac{\partial g}{\partial \bar{\eta}} - \frac{w_{sh} \bar{p}}{h_3} \frac{\partial \bar{p}}{\partial \zeta} + \frac{p_{sh} w_{sh} \bar{n}}{h_3 n_{sh}} \frac{\partial n_{sh}}{\partial \zeta} \frac{\partial p}{\partial \eta} \frac{\partial g}{\partial \bar{\eta}} \\
& - \epsilon^2 \frac{\mu_{sh} \bar{\mu}}{n_{sh}^2} \left(u_{sh} \frac{\partial \bar{u}}{\partial \eta} \frac{\partial g}{\partial \bar{\eta}} - \frac{u_{sh} \bar{u}}{h_1} \frac{\partial h_1}{\partial \bar{\eta}} \right)^2 \\
& - \epsilon^2 \frac{\mu_{sh} \bar{\mu}}{n_{sh}^2} \left(\frac{\partial w_{sh}}{\partial \eta} \frac{\partial g}{\partial \bar{\eta}} - \frac{w_{sh}}{h_3} \frac{\partial h_3}{\partial \bar{\eta}} \right)^2 + \dot{\bar{w}}_1 \quad (4d)
\end{aligned}$$

$$A_4 = \rho_{sh} u_{sh} \bar{\rho} \bar{u} C_{p,sh} \bar{C}_p / h_1 \quad (4e)$$

$$A_5 = \rho_{sh} \bar{\rho} \bar{w} C_{p,sh} \bar{C}_p / h_3 \quad (4f)$$

With

$$\sum_{i=1}^{NS} h_i \dot{\bar{w}}_i = \dot{\bar{w}}_1 + T \dot{\bar{w}}_2 \quad (4g)$$

Species Continuity, $W = C_i$:

$$A_0 = \epsilon^2 \frac{\mu_{sh} \bar{\mu} Le_i}{Pr_{sh} \bar{Pr} n_{sh}^2} \quad (5a)$$

$$A_1 = \epsilon^2 \frac{1}{n_{sh}^2} \left\{ \frac{\partial}{\partial \eta} \left(\frac{\mu_{sh} \bar{\mu} Le_i}{Pr_{sh} \bar{Pr}} \right) \right\} \frac{\partial g}{\partial \eta} + \epsilon^2 \frac{\mu_{sh} \bar{\mu} Le_i}{Pr_{sh} \bar{Pr} n_{sh}^2} \frac{1}{h_1 h_3} \frac{\partial (h_1 h_3)}{\partial \eta} \\ + \frac{\bar{\rho} \rho_{sh} w \bar{\eta}}{n_{sh} h_3} \frac{\partial n_{sh}}{\partial \zeta} + \frac{\bar{\rho} \rho_{sh} \bar{u} u_{sh} \bar{\eta}}{n_{sh} h_1} \frac{\partial n_{sh}}{\partial \xi} - \frac{\bar{\rho} \rho_{sh} v}{n_{sh}} \quad (5b)$$

$$A_2 = -\bar{\rho} \rho_{sh} \dot{w}_i^1 \quad (5c)$$

$$A_3 = \bar{\rho} \rho_{sh} \dot{w}_i^0 \quad (5d)$$

$$A_4 = -\bar{\rho} \rho_{sh} u_{sh} \bar{u}/h_1 \quad (5e)$$

$$A_5 = -\rho_{sh} \bar{\rho} w/h_3 \quad (5f)$$

With

$$\frac{\dot{w}_i}{\rho} = \dot{w}_i^0 - \dot{w}_i^1 C_i \quad (5g)$$

The remaining first-order partial differential equations are written as follows:

Global Continuity:

$$\begin{aligned} \frac{\partial}{\partial \xi} (\rho_{sh} u_{sh} \bar{\rho} \bar{u} h_3) - \frac{\bar{\eta}}{n_{sh}} \frac{\partial n_{sh}}{\partial \xi} \frac{\partial}{\partial \eta} (\rho_{sh} u_{sh} \bar{\rho} \bar{u} h_3) \frac{\partial g}{\partial \eta} + \frac{1}{n_{sh}} \frac{\partial}{\partial \eta} (h_1 h_3 \rho_{sh} \bar{\rho} v) \frac{\partial g}{\partial \eta} \\ + \frac{\partial}{\partial \zeta} (\rho_{sh} \bar{\rho} w h_1) - \frac{\bar{\eta}}{n_{sh}} \frac{\partial n_{sh}}{\partial \zeta} \frac{\partial}{\partial \eta} (\rho_{sh} \bar{\rho} w h_1) \frac{\partial g}{\partial \eta} = 0 \end{aligned} \quad (6)$$

η -momentum:

$$\begin{aligned} \frac{\rho_{sh} u_{sh} \bar{\rho} \bar{u}}{h_1} \frac{\partial v}{\partial \xi} + \frac{\rho_{sh} \bar{\rho} v}{n_{sh}} \frac{\partial v}{\partial \eta} \frac{\partial g}{\partial \eta} - \frac{\rho_{sh} u_{sh} \bar{\rho} \bar{u} \bar{\eta}}{h_1 n_{sh}} \frac{\partial n_{sh}}{\partial \xi} \frac{\partial v}{\partial \eta} \frac{\partial g}{\partial \eta} \\ + \frac{\rho_{sh} \bar{\rho} w}{h_3} \frac{\partial v}{\partial \zeta} - \frac{\rho_{sh} \bar{\rho} w \bar{\eta}}{h_3 n_{sh}} \frac{\partial n_{sh}}{\partial \zeta} \frac{\partial v}{\partial \eta} \frac{\partial g}{\partial \eta} - \frac{\rho_{sh} u_{sh}^2 \bar{\rho} \bar{u}^2}{h_1 n_{sh}} \frac{\partial h_1}{\partial \eta} \\ - \frac{\rho_{sh} \bar{\rho} w^2}{h_3 n_{sh}} \frac{\partial h_3}{\partial \eta} + \frac{p_{sh}}{n_{sh}} \frac{\partial \bar{p}}{\partial \eta} \frac{\partial g}{\partial \eta} = 0 \end{aligned} \quad (7)$$

Equation of State

$$\bar{p} = \bar{\rho} \bar{T} \frac{\bar{w}_{sh}}{\bar{w}} \quad (8)$$

It may be mentioned here that the normal and crossflow velocities v and w , respectively, are not normalized. This has been done to avoid division by small numbers. Also, the temperature and species concentrations are not normalized. The species rate of production term (appearing in the energy and species continuity equations is written in the forms given by Eqs. (4g) and (5g) so that the temperature and species concentration appear as one of the unknowns. These equations help in the convergence of the numerical method.

The scale factors, h_1 , h_2 , and h_3 , appearing in Eqs. (2) through (8) are given by:

$$h_1 = 1 + \kappa_\xi n \quad (9a)$$

$$h_2 = 1 \quad (9b)$$

$$h_3 = r_B (1 + \bar{n} n_{sh} \cos \theta_\xi) \quad (9c)$$

Further, Eqs. (1) through (7) contain the following independent transformation

$$\eta = g\left(\frac{n}{n_{sh}}\right) = g(\bar{\eta}) \quad (10a)$$

where the stretching function $g(\bar{\eta})$ is given by

$$g(\bar{\eta}) = 1 - \left[\bar{\alpha} + \frac{(1 - \bar{\alpha})}{\ln[(\bar{\beta}+1)/(\bar{\beta}-1)]} \ln \left\{ \frac{\bar{\beta} - \bar{\eta}(2\bar{\alpha}+1) + 1}{\bar{\beta} + \bar{\eta}(2\bar{\alpha}+1) - 1} \right\} \right] \quad (10b)$$

and its first and second derivatives are

$$\frac{dg}{d\bar{\eta}} = \frac{(1-\bar{\alpha})(2\bar{\alpha}+1)}{\ln[(\bar{\beta}+1)/(\bar{\beta}-1)]} \left\{ \frac{1}{[\bar{\beta} - \bar{\eta}(2\bar{\alpha}+1) + 1]} + \frac{1}{[\bar{\beta} + \bar{\eta}(2\bar{\alpha}+1) - 1]} \right\} \quad (10c)$$

$$\frac{d^2g}{d\bar{\eta}^2} = \frac{(1-\bar{\alpha})(2\bar{\alpha}+1)^2}{\ln[(\bar{\beta}+1)/(\bar{\beta}-1)]} \left\{ \frac{1}{[\bar{\beta} - \bar{\eta}(2\bar{\alpha}+1) + 1]^2} - \frac{1}{[\bar{\beta} + \bar{\eta}(2\bar{\alpha}+1) - 1]^2} \right\} \quad (10d)$$

Equation (10b) permits the mesh to be refined near the body with $\bar{\alpha}=0$ or refined equally near both the body and shock with $\bar{\alpha}=1/2$ in the physical plane. A value of $\bar{\alpha}=1/2$ has been used here for the low-density flows. Parameter $\bar{\beta}$ controls the amount of refinement with values near 1 giving the largest amount of stretching. Equation (10b) may be inverted to obtain the physical coordinate $\bar{\eta}$ from the transformed η coordinate:

$$\bar{\eta} = \frac{1}{(2\bar{\alpha}+1)} \left[1 - \beta \left\{ \left(\frac{\bar{\beta}+1}{\bar{\beta}-1} \right)^{\frac{1-\bar{\eta}-\bar{\alpha}}{1-\bar{\alpha}}} - 1 \right\} / \left\{ \left(\frac{\bar{\beta}+1}{\bar{\beta}-1} \right)^{\frac{1-\bar{\eta}-\bar{\alpha}}{1-\bar{\alpha}}} + 1 \right\} \right] \quad (10e)$$

The transformation of Eq. (10a) ensures a uniform mesh in the computational coordinate and has zero built-in numerical dissipation due to its analytic nature.

Boundary Conditions

The following wall and shock boundary conditions are employed:

Surface Slip Conditions (employed at $\eta = \eta_s$)

The equations relating the slip values to wall values and gradients at the edge of the Knudsen layer ($\eta = \eta_s$) are:³

Tangential Velocity Slip:

$$\begin{aligned} \bar{u}_s = \epsilon^2 \left(1 / \sum_{i=1}^{NS} \sqrt{\frac{\bar{w}_i}{\bar{w}_s}} C_i^s \right) \left\{ \sqrt{\frac{\pi}{2}} \left(\frac{2-\theta}{\theta} \right) \frac{\mu_{sh}}{\sqrt{p_{sh} \rho_{sh}}} \frac{\bar{u}_s}{\sqrt{\bar{p}_s \bar{\rho}_s}} \right. \\ \left. \times \sqrt{\frac{\bar{w}_\infty}{\bar{w}_s}} \left(\frac{1}{n_{sh}} \frac{\partial \bar{u}}{\partial \eta} \frac{\partial \bar{g}}{\partial \bar{\eta}} - \frac{\kappa_\xi \bar{u}}{1 + n_{sh} \bar{\eta} \kappa_\xi} \right) \right\} \end{aligned} \quad (11)$$

Circumferential Velocity Slip:

$$\begin{aligned} \bar{w}_s = \epsilon^2 \left(1 / \sum_{i=1}^{NS} \sqrt{\frac{\bar{w}_i}{\bar{w}_s}} C_i^s \right) \left\{ \sqrt{\frac{\pi}{2}} \left(\frac{2-\theta}{\theta} \right) \frac{\mu_{sh}}{\sqrt{p_{sh} \rho_{sh}}} \frac{\bar{u}_s}{\sqrt{\bar{p}_s \bar{\rho}_s}} \right. \\ \left. \times \sqrt{\frac{\bar{w}_\infty}{\bar{w}_s}} \left(\frac{1}{n_{sh}} \frac{\partial \bar{w}}{\partial \eta} \frac{\partial \bar{g}}{\partial \bar{\eta}} - \frac{\kappa_\zeta \bar{w} \cos \theta_\xi}{1 + \kappa_\zeta n_{sh} \bar{\eta} \cos \theta_\xi} \right) \right\} \end{aligned} \quad (12)$$

Temperature Slip (with frozen internal energy during reflection from surface):

$$\begin{aligned}
 T_s = T_w + \frac{1}{2} \sqrt{\frac{\pi}{2}} \left(\frac{2-\theta}{\theta} \right) \left(\frac{\bar{\gamma}}{\bar{\gamma}-1} \right) \frac{\epsilon^2}{n_{sh} \bar{Pr} Pr_{sh} \sqrt{\bar{p}_{sh} \rho_{sh}}} \frac{\bar{\mu}_s}{\sqrt{\bar{p}_s \rho_s}} \\
 \times \left(1 / \sum_{i=1}^{NS} \left(\frac{\bar{w}_s}{\bar{w}_i} \right)^{3/2} C_i^s \frac{\partial T}{\partial \eta} \frac{\partial g}{\partial \bar{\eta}} + \epsilon^2 \sqrt{\frac{\pi}{2}} \frac{\mu_{sh} Le_{sh} \bar{Le}_s}{n_{sh} Pr_{sh} \sqrt{\bar{p}_{sh} \rho_{sh}} \bar{Pr}} \right. \\
 \times \frac{\bar{\mu}_s}{\sqrt{\bar{p}_s \rho_s}} \left(1 / \sum_{i=1}^{NS} \left(\frac{\bar{w}_s}{\bar{w}_i} \right)^{3/2} C_i^s \right) \left(\frac{5}{4} \frac{2-\theta}{\theta} T_s + T_w \right) \\
 \left. \times \sum_{i=1}^{NS} \left[\frac{\partial C_i}{\partial \eta} \frac{\partial g}{\partial \bar{\eta}} - (1 - C_i) \sum_{q=1}^{NS} \left(\frac{\bar{w}_s}{\bar{w}_q} \right) \frac{\partial C_q}{\partial \eta} \frac{\partial g}{\partial \bar{\eta}} \right] \right) \quad (13)
 \end{aligned}$$

Pressure Slip:

$$\begin{aligned}
 \bar{p}_s = \bar{p}_w + \frac{4}{5\sqrt{2\pi}} \left(\frac{2-\theta}{\theta} \right) \left(\frac{\bar{\gamma}}{\bar{\gamma}-1} \right) \frac{\epsilon^2}{n_{sh} Pr_{sh} \bar{Pr}_s \sqrt{\bar{p}_{sh} \rho_{sh}}} \sqrt{\frac{\bar{p}_s}{\rho_s}} \\
 \times \frac{1}{T} \frac{\partial T}{\partial \eta} \frac{\partial g}{\partial \bar{\eta}} \sum_{i=1}^{NS} \left(\frac{\bar{w}_s}{\bar{w}_i} \right)^{3/2} C_i^s \bar{\mu}_i \mu_{sh} \quad (14)
 \end{aligned}$$

Concentration Slip:

$$\begin{aligned}
 C_i^w = C_i^s \left(\frac{\bar{p}_s}{\bar{p}_w} \right) \sqrt{\frac{T_s}{T_w}} + \epsilon^2 \sqrt{\frac{\pi}{2T_w}} \left(\frac{\mu_{sh} Le_{sh}}{Pr_{sh}} \right) \left(\frac{\bar{Le}_s \bar{\mu}}{\bar{Pr}} \right) \frac{1}{s \sqrt{\bar{p}_{sh} \rho_{sh}}} \\
 \times \sqrt{\frac{T_s}{\bar{p}_{sh} \rho_s}} \left(\frac{\bar{p}_s}{\bar{p}_w} \right) \left(\frac{\bar{w}_i}{\bar{w}_s} \right)^{3/2} \left[\frac{1}{n_{sh}} \frac{\partial C_i}{\partial \eta} \frac{\partial g}{\partial \bar{\eta}} + \frac{(1 - C_i)}{n_{sh}} \sum_{q=1}^{NS} \frac{\bar{w}_s}{\bar{w}_q} \frac{\partial C_q}{\partial \eta} \frac{\partial g}{\partial \bar{\eta}} \right] \quad (15a)
 \end{aligned}$$

where

$$C_i^s = 1 + \left(\frac{\partial C_i}{\partial \eta} \frac{\partial g}{\partial \eta} + \frac{W_A}{W_i} n_{sh} \psi_i \right)_s / \sum_{q=1}^{NS} \left(\frac{\bar{W}}{W_q} \frac{\partial C_q}{\partial \eta} \frac{\partial g}{\partial \eta} \right)_s \quad (15b)$$

with

$$\text{and } \left. \begin{array}{ll} A = 0 & \text{for } i = O_2 \\ A = N & \text{for } i = N_2 \end{array} \right\} \quad (15c)$$

$$\psi_A^s = - \frac{1}{\epsilon} \frac{1}{2} \sqrt{\frac{2}{\pi}} \left(\frac{\gamma_A}{2 - \gamma_A} \right)_s \frac{\sqrt{p_{sh} p_{sh}}}{\mu_s h} \frac{Pr_{sh} Pr_s}{\bar{Le}_s Le_{sh}} \frac{\sqrt{\bar{p}_s \bar{p}_s}}{\bar{\mu}_s} \left(\frac{\bar{W}_s}{W_A} \right)^{3/2} C_A^s ; \quad (A = 0, N) \quad (15d)$$

$$\psi_M^s = - \psi_A^s ; \quad \left(\begin{array}{l} A = 0 \text{ for } M = O_2 \\ A = N \text{ for } M = N_2 \end{array} \right) \quad (15e)$$

$$\psi_i^s = 0 , \quad (\text{for all other species}) \quad (15f)$$

The recombination rate coefficient, γ_A , appearing in Eq. (15d) is obtained from Scott¹⁴ for $A = \text{atomic nitrogen (N)}$ and from Zoby, Gupta, and Simmonds¹⁵ for $A = \text{atomic oxygen (O)}$ for finite catalytic wall having the shuttle-type thermal protection system (TPS). The shuttle TPS may be assumed noncatalytic to the recombination of other air species.

For a noncatalytic surface, $\bar{\gamma}_A = 0$ in Eq. (15d) and Eq. (15b) with $\psi_i = 0$ for all the species gives:³

$$\frac{\partial C_i}{\partial \eta} = 0 \quad (16)$$

For a fully catalytic surface, an appropriate boundary condition is

$$(C_i)_s = (C_i)_\infty \quad (17)$$

Shock Slip Conditions (at $\eta = 1$)

Continuity: $\rho_{sh} \tilde{v}_{sh} = - \sin \beta \quad (18)$

\tilde{s} -momentum:

$$\epsilon^2 \mu_{sh} \left\{ \frac{1}{n_{sh}} \left[\cos(\beta - \theta_\xi) + \frac{\partial n_{sh}}{\partial \xi} \sin(\beta - \theta_\xi) \right] \left(\frac{\partial g}{\partial \eta} \frac{\partial \tilde{u}}{\partial \eta} \right)_{sh} - \left(\frac{\partial \tilde{u}}{\partial \xi} \right)_{sh} \sin(\beta - \theta_\xi) \right\} + \sin \beta \tilde{u}_{sh} = \cos \beta \sin \beta \quad (19a)$$

where

$$\left(\frac{\partial \tilde{u}}{\partial \eta} \right)_{sh} = \left\{ \left(\frac{\partial u}{\partial \eta} \right)_{sh} \cos(\beta - \theta_\xi) + \left(\frac{\partial v}{\partial \eta} \right)_{sh} \sin(\beta - \theta_\xi) \right\} / \cos \phi_{sh} \quad (19b)$$

and

$$\left(\frac{\partial \tilde{u}}{\partial \xi} \right)_{sh} = \left\{ \left(\frac{\partial u}{\partial \xi} \right)_{sh} \cos(\beta - \theta_\xi) + \left(\frac{\partial v}{\partial \xi} \right)_{sh} \sin(\beta - \theta_\xi) \right\} / \cos \phi_{sh} \quad (19c)$$

\tilde{n} -momentum:

$$p_{sh} = p_\infty + \sin \beta (\sin \beta + \tilde{v}_{sh}) \quad (20)$$

Energy:

$$\begin{aligned}
& \frac{\epsilon^2 K_{sh}}{\sin \beta} \left\{ \frac{1}{n_{sh}} \left[\cos(\beta - \theta_\xi) + \frac{\partial n_{sh}}{\partial \xi} \sin(\beta - \theta_\xi) \right] \left(\frac{\partial T}{\partial \eta} \frac{\partial g}{\partial \eta} \right)_{sh} - \left(\frac{\partial T}{\partial \xi} \right)_{sh} \sin(\beta - \theta_\xi) \right\} \\
& + \sum_{i=1}^{NS} C_{i,sh} h_{i,sh} - \frac{1}{2} [(\tilde{u}_{sh} - \cos \beta)^2 + (\sin^2 \beta - \tilde{v}_{sh}^2)] + \frac{\epsilon^2}{\sin \beta} \\
& \times \frac{\mu_{sh}}{Pr_{sh}} \sum_{i=1}^{NS} Le_{i,sh} h_{i,sh} \left\{ \frac{1}{n_{sh}} \left[\cos(\beta - \theta_\xi) + \frac{\partial n_{sh}}{\partial \xi} \sin(\beta - \theta_\xi) \right] \right. \\
& \times \left. \left(\frac{\partial C_i}{\partial \eta} \frac{\partial g}{\partial \eta} \right)_{sh} - \left(\frac{\partial C_i}{\partial \xi} \right)_{sh} \sin(\beta - \theta_\xi) \right\} = \sum_{i=1}^{NS} C_{i,\infty} h_{i,\infty} \quad (21)
\end{aligned}$$

Species Continuity:

$$\begin{aligned}
& \frac{\epsilon^2 \mu_{sh} Le_{i,sh}}{Pr_{sh}} \left\{ \frac{1}{n_{sh}} \left[\cos(\beta - \theta_\xi) + \frac{\partial n_{sh}}{\partial \xi} \sin(\beta - \theta_\xi) \right] \left(\frac{\partial C_i}{\partial \eta} \frac{\partial g}{\partial \eta} \right)_{sh} - \left(\frac{\partial C_i}{\partial \xi} \right)_{sh} \sin(\beta - \theta_\xi) \right\} \\
& + \sin \beta (C_{i,sh} - C_{i,\infty}) = \int_{sh}^{\infty} \dot{w}_i d\eta = \dot{w}_{i,ave} \delta_{sh} \quad (22a)
\end{aligned}$$

with

$$\dot{w}_{i,ave} = \dot{w}_{i,sh}/2 \quad (22b)$$

and

$$\delta_{sh} = (\eta_\infty - \eta_{sh}) \quad (22c)$$

The shock thickness, δ_{sh} , to a good degree of approximation may be obtained from

$$\delta_{sh} = 0.174 M_\infty \epsilon^2 \quad (22d)$$

Equation (22d) has been approximated from references 16 and 17. This equation has been further verified by integrating the equations for a merged stagnation shock layer of nonequilibrium dissociating gas¹⁸ with the same properties as those used here. The shock thickness, δ_{sh} , obtained in reference 18 from integrating through the shock keeping the \dot{w}_i term is very close to that obtained from Eq. (22d). If the shock is thin (i.e., δ_{sh} is of order 10^{-2}) the mass rate of production of atoms, \dot{w}_i , may be assumed negligible across the shock. This assumption makes the right-hand side of Eq. (22a) zero.

Since velocity components tangent and normal to the shock (see Fig. 1) are not the same as those tangent and normal to the body, the following transformations are needed to obtain velocity components at the shock in the body-oriented coordinates from the shock-oriented coordinates:

$$u_{sh} = \tilde{u}_{sh} \cos \phi_{sh} \cos(\beta - \theta_\xi) - \tilde{v}_{sh} \cos \phi_{sh} \sin(\beta - \theta_\xi) \quad (23)$$

$$v_{sh} = \tilde{u}_{sh} \cos \phi_{sh} \sin(\beta - \theta_\xi) + \tilde{v}_{sh} \cos \phi_{sh} \cos(\beta - \theta_\xi) \quad (24)$$

$$w_{sh} = -\sin \phi_{sh} \sqrt{\tilde{u}_{sh}^2 + \tilde{v}_{sh}^2} \quad (25)$$

where β and θ_ξ are the shock and body angles, respectively, and ϕ_{sh} is the crossflow angle (see fig. 2a) defined as:¹⁹

$$\sin \phi_{sh} = \frac{w}{U_\infty} \quad (26a)$$

$$= -\sin(\sigma' - \theta_2') N_\phi + \cos(\sigma' - \theta_2') T_\phi \quad (26b)$$

In Eq. (26b), $(\sigma' - \theta_2')$ is the angle which the velocity vector after crossing the shock makes with the shock-tangent vector, \hat{T} , in the \hat{N} - \hat{T} plane (see fig. 2b) and N_ϕ and T_ϕ are the components of normal and tangential vectors \hat{N} and \hat{T} , respectively, in the crossflow direction (see fig. 2a). For a 2D flow over an axisymmetric body at zero degree angle of attack, Eqs. (23) and (24) reduce to those given in reference 20 with $\phi_{sh} = 0$ degree.

Alternately, the following relations can also be used to relate the velocity components at the shock in the body- and shock-oriented coordinate systems:

$$u_{sh} = \cos \phi_{sh} \cos(\beta_{sh} - \theta_\xi) \sqrt{\tilde{u}_{sh}^2 + \tilde{v}_{sh}^2} \quad (27)$$

$$v_{sh} = \cos \phi_{sh} \sin(\beta_{sh} - \theta_\xi) \sqrt{\tilde{u}_{sh}^2 + \tilde{v}_{sh}^2} \quad (28)$$

$$w_{sh} = -\sin \phi_{sh} \sqrt{\tilde{u}_{sh}^2 + \tilde{v}_{sh}^2} \quad (29)$$

where β_{sh} is the flow angle from the body axis in a meridional (or $\phi = \text{constant}$) plane¹⁹ (see fig. 2c):

$$\tan \beta_{sh} = \frac{-\sin(\sigma' - \theta_2')N_r + \cos(\sigma' - \theta_2')T_r}{-\sin(\sigma' - \theta_2')N_x + \cos(\sigma' - \theta_2')T_x} \quad (30)$$

with angles σ' and θ_2' defined in figure 2b and N_x , T_x , and N_r , T_r are the components of vectors \hat{N} and \hat{T} in the body-axis and radial directions, respectively.

Angle $(\beta_{sh} - \theta_\xi)$ appearing in Eqs. (27) and (28) may be obtained from (see fig. 2c):

$$\tan(\beta_{sh} - \theta_\xi) = \frac{v_{sh}^*}{u_{sh}^*} = \frac{v_{sh}}{u_{sh}} \quad (31)$$

Chemical Reaction Model

The net mass rate of production of a chemical species per unit volume, \dot{w}_i^* , is obtained from the usual kinetic relations.^{21,22} For the seven species (O_2, N_2, O, N, NO, NO^+ , and e^-) air calculations in the present code, the reaction model is similar to that used in references 22 and 23. The species production terms appearing in the energy and species continuity equations are written in terms of temperature and concentration following the approach of references 21 and 22. The reaction rate constants and the relative efficiencies of the catalytic third bodies are obtained from reference 22. These rate equations and constants are similar to those used in previous studies^{4,5,11,23}. These are also identical to those used in 2D VSL studies^{15,24}.

Thermodynamic and Transport Properties

Thermodynamic properties for the multicomponent air mixture are obtained by assuming a thermally perfect gas. The equation of state for the gas mixture is given earlier as Eq. (8). Thermodynamic properties for the individual species are obtained by interpolation in the data of Browne.^{25,27} More details of the formulation employed in the present calculations can be found in reference 23, which follows the thermodynamic models of references 25 to 27.

Transport properties for the gas mixture are obtained using the methods of reference 28 for viscosity and that of reference 29 for thermal conductivity. Individual species viscosity and frozen thermal conductivity are based on the more recent work of reference 30. These data are believed to be more accurate at higher temperatures, encountered in nonequilibrium

calculations. It may also be mentioned that the present mixture thermal conductivity relation²⁹ accounts for the contribution from the internal modes similar to reference 11, whereas, the relation³² used in reference 31 does not.

In this study, a variable Prandtl number is used, whereas, the Lewis number is set equal to 1.4. For the ionized species, ambipolar type of diffusion is employed.³³ For such a diffusion the binary diffusion coefficients must be doubled in the calculations. Accordingly, a Lewis number of 2.4 has been used for the ionized species. Previous studies^{4,5,31} ignored this effect.

Method of Solution

The numerical solution of the viscous-shock-layer equations was presented by Davis^{2,21} for the axisymmetric and two-dimensional (2D) flows. An implicit finite-difference scheme was used which was efficient in terms of both computer time and storage. In developing the three-dimensional (3D) viscous-shock-layer method for a perfect gas, Murray and Lewis³⁴ adopted a similar scheme for the numerical solution, as did references 4,5,11, and 31 for the nonequilibrium three-dimensional formulation. The same finite-difference method is used here to solve the ξ -momentum, ζ -momentum, energy, and species continuity equations, namely, equations (1) through (5). By using two-point backward differences in the ξ -direction, the zig-zag finite-difference expressions of Krause³⁵ in the ζ -direction, and central differences in the η -direction in the second-order parabolic equations (1) through (5), a tridiagonal finite-difference form is obtained which can be solved by the Thomas algorithm for each of the dependent variable represented by W . The

solution to this second-order set of equations is obtained in an uncoupled cascading scheme similar to that used by Davis.² The first-order differential equations (6) and (7) of continuity and normal momentum, respectively, are solved by a similar method, but they are coupled together.³⁴ The coupled solution of these two equations promotes convergence and ensures stability in the marching solution, especially, for the slender bodies.

There are a few points in the flowfield where the governing equations become singular and the limiting form must be evaluated. Along the stagnation streamline, the ξ -derivatives of the pressure and shock stand-off distance are zero and the tangential component of velocity behind the shock, u_{sh} , is also zero. These result in a singularity in the coefficients of ξ -momentum equation. The continuity equation also becomes singular with ξ approaching zero. These singularities are removed by using the series expansions of references 36 and 37. Further, the crossflow velocity, w , is zero along the windward and leeward streamlines and the value of $\partial w / \partial \zeta$ is needed in the continuity equation. This is obtained by taking the ζ -derivative of the crossflow equation and solving for the new dependent variable $\partial w / \partial \zeta$. In the windward and leeward planes, the ζ -derivatives of all dependent variables except that of w are zero, and the second derivative of w is zero. The equation for $\partial w / \partial \zeta$ is solved by writing it in the standard parabolic form, namely, Eq. (1).

The present viscous shock-layer solution begins on the spherical nose cap at the aerodynamic stagnation point where an axisymmetric solution in a wind-fixed coordinate system is obtained. The axisymmetric (one plane) solution on the sphere is marched downstream to encompass the aerodynamic and geometric stagnation points. The wind-fixed solution is then rotated around the sphere

and interpolated to obtain the shock-layer profiles in the body-fixed (three-dimensional) coordinate system. These are used as the initial profiles for the 3D solution. The 3D solution begins in the windward plane at a specified streamwise (or ξ) location and marches around the body obtaining a converged solution at each circumferential (or ζ)-direction step. The governing equations are solved at each point in the flowfield in the following order: species continuity, crossflow (or ζ)-momentum, energy, streamwise-momentum, integration of global continuity for shock standoff distance, n_{sh} , and the coupled normal (or η)-momentum and continuity equations. After integration of the continuity equation, the new shock standoff distance is used to update the shock-layer profiles for the next local iteration while the shock slope, $\partial n_{sh} / \partial \xi$, remains fixed at the input value. The equations are iterated in this manner until each of the flowfield variables is converged through the entire shock-layer at the given ξ - and ζ -stations.

The solution procedure at a given ξ -station on the axisymmetric part (or nose region) is shown in figure 3. Figure 4 depicts the solution procedure used on the body (beyond the tangency point) at a given ξ -station for various values of $\zeta(\phi)$ or cross-flow planes.

Global convergence of the VSL solutions is satisfied by repeating the calculation over the entire body using the computed shock standoff distance obtained during the previous pass to provide the new shock shape (i.e., shock standoff distance and its slope). Global iterations are repeated until the input and output shock shapes are converged.

Calculation of Input Shock Shape

The global iteration process outlined in the previous paragraph requires an initial value of the shock slope, $\partial n_{sh}/\partial \xi$, and $\partial v/\partial \xi$, which introduce an elliptic effect into the equations. In the present scheme, $\partial n_{sh}/\partial \xi$, is obtained either from an inviscid equilibrium air solution³⁸ (which is scaled by a constant) or from a viscous nonequilibrium analysis. The values of $\partial v/\partial \xi$ are calculated from a backward difference approximation. The scaling factor used with the inviscid equilibrium solution for the shock standoff distance is in the range of 1.2 to 1.25. The initial input shock shape obtained from this scaling accounts for the nonequilibrium effects on the flowfield and limits the shock-shape correction and, therefore, decreases the required global iterations.

Even though the results obtained from using an inviscid equilibrium shock shape with a scaling factor are satisfactory for nonequilibrium viscous flows at high Reynolds numbers, convergence problems are encountered at freestream Reynolds numbers (based on the nose radius) less than about 2000. These values of the Reynolds number are encountered under the low-density flight conditions. Under these conditions, the entire shock-layer becomes viscous. An alternate method for obtaining a 3D viscous, nonequilibrium input shock shape is, therefore, suggested here. Starting point is the generation of 2D viscous nonequilibrium shock shapes for an axisymmetric body (see fig. 5) with effective body angles of $(\theta_{\xi} + \alpha)$ (for simulating the flowfield on the windward side) and $(\theta_{\xi} - \alpha)$ (for simulating the flowfield on the leeward side). The 2D VSL solutions can be obtained from the 3D VSL code by running it in the 2D mode. For the body at an angle of attack, α , these solutions are used from the aerodynamic stagnation point up to the tangency point (where the nose of

the body is axisymmetric) in the wind-fixed coordinates (see fig. 6). Beyond the tangency point, the shock shape (for the body solutions) is specified in the body fixed coordinates. The relationship between the wind-fixed and body-fixed coordinates (shown in figs. 1 and 5) along the windward and leeward streamlines, respectively, is

$$(s_{\text{wind}}^*)_{\zeta(\phi)=0} = s_{\text{body}}^* - \alpha \quad (32a)$$

$$(s_{\text{wind}}^*)_{\zeta(\phi)=\pi} = s_{\text{body}}^* + \alpha \quad (32b)$$

Having obtained the windward-side and leeward-side values of the shock standoff distance and shock slope from the 2D solutions of bodies with effective body angles, their distributions around the body ($0 < \zeta(\phi) < \pi$) for body solution (i.e., beyond the tangency point) may be obtained from:

$$\begin{aligned} [n_{\text{sh}}^*]_{(s_{\text{body}}^*)_{\text{TP}}} &= [(n_{\text{sh}}^*)_{\theta_{\xi} + \alpha}]_{(s_{\text{body}}^*)_{\text{TP}} - \alpha} \left(\frac{1 + \cos \phi}{2} \right) \\ &+ [(n_{\text{sh}}^*)_{\theta_{\xi} - \alpha}]_{(s_{\text{body}}^*)_{\text{TP}} + \alpha} \left(\frac{1 - \cos \phi}{2} \right) \end{aligned} \quad (33)$$

$$\begin{aligned} \left[\frac{\partial n_{\text{sh}}^*}{\partial s^*} \right]_{(s_{\text{body}}^*)_{\text{TP}}} &= \left[\left(\frac{\partial n_{\text{sh}}^*}{\partial s^*} \right)_{\theta_{\xi} + \alpha} \right]_{(s_{\text{body}}^*)_{\text{TP}} - \alpha} \left(\frac{1 + \cos \phi}{2} \right) \\ &+ \left[\left(\frac{\partial n_{\text{sh}}^*}{\partial s^*} \right)_{\theta_{\xi} - \alpha} \right]_{(s_{\text{body}}^*)_{\text{TP}} + \alpha} \left(\frac{1 - \cos \phi}{2} \right) \end{aligned} \quad (34)$$

The same relations are valid for $s_{\text{body}}^* > (s_{\text{body}}^*)_{\text{TP}}$.

Surface Quantities

The following surface quantities may be computed from the flowfield profiles obtained from solutions of the governing equations described earlier.

(i) Stanton Number:

$$St = \frac{-q_w}{\rho_\infty U_\infty (H_\infty - H_w)} \quad (35)$$

(ii) Heat Transfer Coefficient:

$$C_H = \frac{-q_w}{\rho_\infty U_\infty C_{p,\infty} (T_{aw} - T_w)} \quad (36)$$

(iii) Wall Heat-Transfer Rate:

$$\begin{aligned} q_w = & - \left(\frac{\mu_{sh} T_{sh}}{Pr_{sh} n_{sh}} \right) \frac{\bar{\mu}_s}{\bar{Pr}_s} \left(\frac{\partial \bar{T}}{\partial \eta} \frac{\partial \bar{g}}{\partial \eta} \right)_s \\ & - \epsilon^2 \frac{\mu_{sh}}{\mu_s} \frac{n_{sh}}{n_{sh}} \left\{ u_{sh}^2 \bar{u}_s \left(\frac{\partial \bar{u}}{\partial \eta} \frac{\partial \bar{g}}{\partial \eta} - \bar{u} \frac{\partial h_1}{\partial \eta} \right)_s \right. \\ & + w_{sh}^2 \bar{w}_s \left(\frac{\partial \bar{w}}{\partial \eta} \frac{\partial \bar{g}}{\partial \eta} - \bar{w} \frac{\partial h_3}{\partial \eta} \right)_s \left. \right\} \\ & - \epsilon^2 \frac{\mu_{sh}}{n_{sh} Pr_{sh}} \sum_{i=1}^{NS} \left(\frac{\bar{\mu} Le_i}{\bar{Pr}} \right)_s \left(h_i \frac{\partial C_i}{\partial \eta} \frac{\partial \bar{g}}{\partial \eta} \right)_s \end{aligned} \quad (37)$$

(iv) Skin-friction Coefficient in the Streamwise Direction:

$$C_{f_\xi} = \frac{2\epsilon^2 \mu_{sh} u_{sh}}{n_{sh}} \bar{\mu}_s \left(\frac{\partial \bar{u}}{\partial \eta} \frac{\partial \bar{g}}{\partial \eta} - \bar{u} \frac{\partial h_1}{\partial \eta} \right)_s \quad (38)$$

(v) Skin-friction Coefficient in the Transverse Direction:

$$C_{f_z} = \frac{2\epsilon^2 \mu_{sh} w_{sh}}{n_{sh}} \bar{\mu}_s \left(\frac{\partial \bar{w}}{\partial \eta} \frac{\partial g}{\partial \bar{\eta}} - \frac{\bar{w}}{h_3} \frac{\partial h_3}{\partial \bar{\eta}} \right) \quad (39)$$

(vi) Pressure Coefficient:

$$C_p = \frac{2}{\gamma M_\infty^2} \left(\frac{p_w}{p_\infty} - 1 \right) \quad (40)$$

RESULTS AND DISCUSSION

Detailed flowfield results have been obtained here for sphere-cone shaped bodies at various angles of attack with a 3D nonequilibrium viscous-shock-layer code (VSL3DNQ). Obtained results show the effect of low density on the flowfield around hypervelocity vehicles. Present predictions have been compared with the available experimental data and other numerical predictions, including those from the Direct Simulation Monte Carlo Method (DSMC).

Perfect-gas Results With and Without Slip

Perfect-gas calculations were carried out first to check the computational grid implemented here. Figure 6 shows comparison of the laminar heating distributions with the experimental data of cleary (ref. 39) for a 15-deg sphere cone at 20-deg angle of attack. The present prediction compares quite well both for the windward ($\zeta(\phi)=0^\circ$) and side ($\zeta(\phi)=90^\circ$) meridionals. Figure 7 contains the surface heat transfer distributions for these two meridional planes with and without slip. Similar to figure 6 these

results are also for a 15-deg sphere cone at 20-deg angle of attack. Only difference here (in fig. 7) is the value of freestream Reynolds number, which is much lower due to the low value of the density employed here. The Reynolds number parameter, ϵ , which is a measure of low-density effects, has a value of 0.138 here. We should mention here that the axisymmetric solutions over the spherical nose are given in the wind-fixed coordinates (see fig. 1), whereas the 3D (or body) solutions obtained beyond the tangency point are given in body-fixed coordinates. Figures 6 and 7 illustrate that fairly accurate and consistent results are obtained for the windward and side meridional planes with and without slip.

Results for Nonequilibrium Flow Without Slip

These results have been obtained to check the accuracy of solutions with the new grid and transport properties as well as to study the effect of input shock shape. As mentioned earlier, the input shock shape plays a major role in obtaining good quality solutions and their global convergence.

Effect of input shock shape. Figure 8 shows the input shock shapes for the leeward and windward sides obtained from the inviscid equilibrium and viscous nonequilibrium flowfield calculations. As mentioned earlier, the inviscid equilibrium shock shape is obtained from the code of reference 38. The viscous nonequilibrium shock shape is obtained from 2D calculations using the effective body angles for the windward and leeward sides and employing a cosine distribution to obtain shock shapes for other meridional planes. As expected, the shock standoff distance obtained from the inviscid equilibrium calculations is smaller than the one obtained from the viscous nonequilibrium computations. The difference between the two values increases with the

decrease in density. Figure 9 gives the same shock standoff distance by employing the two different shock shapes of figure 8 for this relatively high density case. It may be mentioned here that for moderately high-density nonequilibrium flowfield calculations, an input shock shape obtained from inviscid equilibrium flow calculations serves as a good initial guess with a scaling factor of about 1.2. However, for the fairly low density flows ($R_{e,\infty} < 2000$ or so), solutions may never converge with an inviscid equilibrium input shock shape.

Figures 10 and 11 show the convergence history of the shock slope using the viscous nonequilibrium and inviscid equilibrium input shock shapes, respectively. Clearly, the shock slope converges faster with a viscous nonequilibrium input shock shape. Surface heat transfer coefficient employing the two input shock shapes converges to almost same value as shown in figure 12, with inviscid equilibrium input shock shape requiring an additional global pass for this case.

Comparison with 2D results. Figures 13 through 18 show comparisons of the results obtained for a 20-deg sphere cone at zero-deg angle of attack by employing the present 3D nonequilibrium viscous-shock-layer (VSL3DNQ) code and an earlier developed (ref. 40) 2D nonequilibrium viscous-shock-layer (VSL2DNQ) code. Both of these codes employ similar computational grids, reaction-rate kinetics, transport and thermodynamic properties. Therefore, the two codes predict, as expected, almost the same velocity, temperature, and species concentration profiles as shown in figures 13 through 18.

3D calculations. Figures 19 through 25 contain the 3D results obtained for a 20-deg sphere cone at 5-deg angle of attack. Figures 19 and 20 show the skin-friction coefficient and surface heat-transfer coefficient distributions,

respectively. Results for the axisymmetric spherical nose are shown in wind-fixed coordinates (see fig.1) whereas the 3D results for different cross flow planes beyond the tangency point are in body-fixed coordinates in these two figures. Figures 21 through 25 contain flowfield profiles of various species at different crossflow (or meridional) planes for a given streamwise body location of $\xi(s) = 2.02$. For the calculations shown in these figures, the wall is assumed to be noncatalytic and the species are assumed frozen at the freestream value behind the shock i.e., at $n/n_{sh}=1$. These figures also show that maximum dissociation and ionization (as depicted by the electron number density provided in fig. 25) occurs along the windward meridional plane ($\zeta(\phi) = 0^\circ$).

Effect of angle of attack. The shock slope and the surface heat transfer coefficient for a 9-deg sphere cone at three different angles of attack (5° , 8° , and 11°) are given in figures 26 and 27, respectively. The results are shown only for the leeward and windward meridional planes. As before, the axisymmetric results for the spherical nose are given in wind-fixed coordinates, whereas the 3D results beyond the tangency point are given in body-fixed coordinates. The maximum heating at the aerodynamic stagnation point is obtained for the 5-deg angle-of-attack case. Also, the heating is higher both for the windward and leeward sides of the body at 5-deg angle of attack than at higher angles of attack.

Results for Nonequilibrium Flow with Slip

Comparison with experimental data. Before carrying out the extensive nonequilibrium calculations for the low density flows, RAM C-II and RAM C-III (refs. 41 and 42) flight data were used to verify the accuracy of VSL3DNQ

predictions with slip. These were two of the three "Radio Attenuation Measurement" test vehicles for the investigation of flowfield plasma under reentry conditions. The vehicle was a 9-deg spherically-blunted cone and was instrumented to measure electron number density across the shock layer. Microwave reflectometers were used to measure the peak values of electron number densities in the shock layer at several locations along the cone. A Langmuir probe rake that extended across the shock layer at the base of the cone measured electron number density profiles. Details of the vehicle and experiment are given in references 41 and 42. RAM C flight data are the only data for the flowfield profiles under the high-energy, low-density flight conditions. Figure 28 shows an excellent comparison between the flight-data and the present predictions with surface and shock slip. Similarly, the present predictions of peak electron number density within the shock layer compare very well with the experimental data as shown in figure 29. These comparisons show that the accuracy of the low-density predictions with the present slip-formulation is quite good.

Comparisons with DSMC and other calculations. Figure 30 gives a comparison between the present predictions and those of reference 43 from the direct Simulation Monte Carlo (DSMC) method. Present results are shown with and without the surface and shock slip boundary conditions. These predictions (with corrections) are based on the surface boundary conditions of reference 3 and shock slip conditions presented here. These predictions also employ the computational grid of Eq. (10). The results without corrections are those obtained from the code of reference 11 with slip formulation of references 4 and 5. These results are used in reference 43 for comparison with the DSMC predictions. Clearly, the present VSL3DNQ-slip predictions (with corrections)

are in fair agreement with the DSMC results and have the similar behavior at high altitudes. The differences between two results may be due to the surface interaction models, the transport properties, and the computational grid employed in the calculations. Present predictions as well as the DSMC results approach the no-slip VSL predictions under the high-density flow conditions, as expected. We should mention here that substantial computer resources (both computational time and storage) are required to obtain the DSMC results, especially, at moderately high densities such as those shown between 60- and 75-km altitudes in figure 30. Comparison between the present predictions and DSMC results (of ref. 43) for the surface pressure coefficient is given in figure 31. Unfortunately, only one computed result is available from the DSMC method for the conditions of this figure. Still, the predictions compare favorably.

Figures 32 through 34 show further comparisons with the code of reference 11 (containing the slip formulations of refs. 4 and 5) and the present results. Present results are shown 'with corrections'. Present slip formulation gives lower flowfield temperatures and lower surface heat-transfer rates, particularly, in the stagnation region.

Low density effects on 3D calculations. Finally, detailed flowfield results are obtained to analyze the effects of low density on 3D calculations. Figures 35 through 46 contain these results for a 9-deg sphere-cone at 5-deg angle of attack for a fully catalytic surface. From the results presented in figures 35 through 38, the surface pressure coefficient (fig. 38) is impacted the least by the slip effects. The effect of slip on other surface quantities is also not much due to the fully catalytic wall boundary condition employed here. Of all the flowfield quantities, temperature (fig. 40) and density

(fig. 41) appear to contain the maximum slip effects near the surface. Species mass fractions near the fully catalytic surface are the same as those in the freestream as shown in figures 42 through 46.

CONCLUDING REMARKS

Results from this study can be summarized as follows:

1. A 3D nonequilibrium viscous-shock-layer (VSL3DNQ) code has been modified for analyzing the low-density, nonequilibrium flow past hypervelocity vehicles. This code is robust, dependable and fairly accurate.
2. Recently obtained surface and shock-slip boundary conditions are implemented to account for the low-density effects.
3. The governing equations are solved in the computational domain with a uniform grid. The grid-transformation employed gives finer resolution at both surface and shock and does not add any numerical dissipation to the results.
4. Input shock shape obtained from the viscous nonequilibrium flow results in a superior convergence history, especially for the low-density flows.
5. Very good agreement is obtained with the cleary's perfect-gas data for the high Reynolds number case.
6. Results for the zero-deg angle-of-attack case are in excellent agreement with those obtained from an earlier developed 2D nonequilibrium code.
7. Excellent agreement is obtained with the RAM C flight data for the low-density high-energy flow conditions.

8. Present results compare favorably with those obtained from the Direct-Simulation Monte Carlo (DSMC) method for the low-density hypersonic flows.

Finally, despite its certain limitations, viscous shock-layer method has been shown to be computationally efficient and a valuable tool for analyzing the low-density flows. With the method suggested here for obtaining the input shock shape for the 3D nonequilibrium viscous flows, the VSL method becomes self-starting unlike the parabolized Navier-Stokes (PNS) methods. The VSL method has been used for obtaining the starting profiles for some of the PNS calculations. The surface slip conditions presented here may also be used for low-density calculations employing the Navier-Stokes equations. Further, if a shock-fitting approach is used for such calculations to keep the computer storage requirement reasonably small, the present shock-slip formulation can be utilized.

REFERENCES

- [1] Tree, I. K., Melson, N. D., and Lewis, C. H., "Low Reynolds Number Hypersonic Ionizing Viscous Shock-Layer Flows Over the Jovian Probe," AIAA Paper No. 79-1080, June 1979.
- [2] Davis, R. T., "Numerical Solution of the Hypersonic Viscous Shock-Layer Equations," AIAA Journal, Vol. 8, No.5, May 1970, pp. 843-851.
- [3] Gupta, R. N., Scott, C. D. and Moss, J. N., "Slip-Boundary Equations for Multicomponent Nonequilibrium Air Flow," NASA TP 2452, Nov. 1985.
- [4] Swaminathan, S., Song, D. J. and Lewis, C. H., "Effects of Slip and Chemical Reaction Models on Three-Dimensional Nonequilibrium Viscous Shock-Layer Flows," Journal of Spacecraft and Rockets, Vol. 21, Nov.-Dec. 1984, pp. 521-527.
- [5] Song, D. J. and Swaminathan, S., and Lewis, C. H., "High Altitude Effects on Three-Dimensional Nonequilibrium Viscous Shock-Layer Flows," Journal of Spacecraft and Rockets Vol. 22, Nov.-Dec. 1985, pp. 614-619.
- [6] Hendricks, W. L., "Slip Conditions with Wall Catalysis and Radiation for Multicomponent Nonequilibrium Gas Flow," NASA TMX-64942, 1974.
- [7] Moss, J. N. and Simmonds, A. L., "Galileo Probe Forebody Flowfield Predictions During Jupiter Entry," AIAA Paper 82-0874, June 1982.

- [8] Gupta, R. N., Lee, K. P., Zoby, E. V., Moss, J. N., and Thompson, R. A., "Hypersonic Viscous Shock-Layer Solutions Over Long Slender Bodies: Part I-High Reynolds Number Flows," AIAA Paper 87-2487, Monterey, CA 1987; also to appear in Journal of Spacecraft and Rockets, Dec. 1987.
- [9] Thareja, R. R., Szema, K. Y., and Lewis, C. H., "Chemical Equilibrium Laminar or Turbulent Three-Dimensional Viscous Shock-Layer Flows," Journal of Spacecraft and Rockets Vol. 20, Sep.-Oct. 1983, pp. 454-460.
- [10] Swaminathan, S., Kim, M. D., and Lewis, C. H., "Three-Dimensional Nonequilibrium Viscous Shock-Layer Flows Over Complex Geometries," AIAA Paper 83-0212, Jan. 1983.
- [11] Thompson, R. A., "Three-Dimensional Viscous Shock-Layer Applications for the Space Shuttle Orbiter," Thermophysical Aspects of Re-Entry Flows, edited by J. N. Moss and C. D. Scott, Vol. 103 of Progress in Astronautics and Aeronautics, 1986, pp. 541-570.
- [12] Williams, F. A., Combustion Theory, Addison-Wesley Pub, Co., Inc., 1965.
- [13] Bird, R. B., Stewart, W. E., and Lightfoot, E. N., Transport Phenomena, John Wiley & Sons, Inc., 1960.
- [14] Scott, C. D., "Catalytic Recombination of Oxygen and Nitrogen in High Temperature Reusable Surface Insulation," Aerothermodynamics and Planetary Entry, edited by A. L. Crosbie, Vol. 77 of Progress in Astronautics and Aeronautics, 1981, pp. 192-212.

- [15] Zoby, E. V., Gupta, R. N., and Simmonds, A. L., "Temperature-Dependent Reaction Rate Expressions for Oxygen Recombination," Thermal Design of Aeroassisted Orbital Transfer Vehicles, edited by H. F. Nelson, Vol. 96 of Progress in Astronautics and Aeronautics, 1985, pp. 445-465.
- [16] Kogan, M. N., Rarefied Gas Dynamics, Plenum Press, New York, 1969.
- [17] Adams, M. C. and Probstein, R. F., "On the Validity of Continuum Theory for Satellite and Hypersonic Flight Problems at High Altitudes," Jet Propulsion, February 1958, pp. 86-89.
- [18] Gupta, R. N. and Simmonds, A. L., "Hypersonic Low-Density Solutions of the Navier-Stokes Equations with Chemical Nonequilibrium and Multicomponent Surface Slip," AIAA Paper #86-1349, Boston, June, 1986.
- [19] Rakich, J. V., "A Method of Characterstics for steady Three-Dimensional Supersonic Flow with Application to Inclined Bodies of Revolution," NASA TND-5341, October, 1969.
- [20] Lee, K. P., Gupta, R. N., Moss, J. N. and Zoby, E. V., "Viscous Shock-Layer Solutions for the Low-Density Hypersonic Flow Past Long Slender Bodies," AIAA Paper #88-0460, Reno, Jan. 1988.
- [21] Davis, R. T., "Hypersonic Flow of a Chemically Reacting Binary Mixture Past a Blunt Body," AIAA Paper No. 70-805, July 1970.

- [22] Blottner, F. G., Johnson, M. and Ellis, M., "Chemically Reacting Viscous Flow Program for Multi-Component Gas Mixtures," Sandia Laboratories Report SC-RR-70-754, December 1971.
- [23] Miner, E. W. and Lewis, C. H., "Hypersonic Ionizing Air Viscous Shock-Layer Flows Over Nonanalytical Blunt Bodies," NASA CR-2550, May 1975.
- [24] Zoby, E. V., Lee, K. P., Gupta, R. N., Thompson, R. A., and Simmonds, A. L., "Viscous Shock-Layer Solutions with Nonequilibrium Chemistry for Hypersonic Flows Past Slender Bodies," Journal of Spacecraft and Rockets, Vol. 26, No. 4, July-Aug. 1989, pp. 221-228.
- [25] Browne, W. G., "Thermodynamic Properties of Some Atoms and Atomic Ions," MSD Engineering Physics TM2, General Electric Co., Philadelphia, PA.
- [26] Browne, W. G., "Thermodynamic Properties of some Diatomic and Linear Polyatomic Molecules," MSD Engineering Physics TM3, General Electric Co., Philadelphia, PA.
- [27] Browne, W. G., "Thermodynamic Properties of Some Diatoms and Diatomic Ions at High Temperature," MSD Advanced Aerospace Physics TM8, General Electric Co., Philadelphia, PA, May 1962.
- [28] Armaly, B. F. and Sutton, K., "Viscosity of Multicomponent Partially Ionized Gas Mixtures Associated with Jovian Entry," Aerothermodynamics and Planetary Entry, edited by A. L. Crosbie, Vol. 77, Progress in Astronautics and Aeronautics, 1982.

- [29] Mason, E. A. and Saxena, S. C., "Approximate Formula for the Thermal Conductivity of Gas Mixtures," Physics of Fluids, Vol. 1, No. 5, 1958, p. 361.
- [30] Gupta, R. N., Yos, J. M., Thompson, R. A., and Lee, K. P., "A Review of Reaction Rates and Thermodynamic and Transport Properties for the 11-species Air Model for Chemical and Thermal Nonequilibrium Calculations to 30000K," NASA TM-101528, 1989; updated as NASA RP 1232, 1990.
- [31] Kim, M. D., Swaminathan, S., and Lewis, C. H., "Three-Dimensional Nonequilibrium Viscous Shock Layer Flows Over the Space Shuttle Orbiter," AIAA paper 83-0487, Jan. 1983.
- [32] Armaly, B. F. and Sutton, K., "Thermal Conductivity of Partially Ionized Gas Mixtures," Thermophysics of Atmospheric Entry, edited by T. E. Horton, Vol. 82, Progress in Astronautics and Aeronautics, 1982.
- [33] Blottner, F. G., "Nonequilibrium Laminar Boundary Layer Flow of Ionized Air," AIAA J., Vol. 2, No. 11, Nov. 1964, pp. 1921-1927.
- [34] Murray, A. L. and Lewis, C. H., "Hypersonic Three-Dimensional Viscous Shock-Layer Flows Over Blunt Bodies," AIAA J., Vol. 16, December 1978, pp. 1279-1286.
- [35] Krause, E., "Comment on 'Solution of a Three-Dimensional Boundary-Layer Flow with Separation'," AIAA J., Vol. 6, March 1969, pp. 575-576.

- [36] Moss, J. N., "Reacting Viscous Shock-Layer Solutions with Multicomponent Diffusion and Mass Injection," NASA TR R-411, June 1974.
- [37] Murray, A. L. and Lewis, C. H., "Hypersonic Three-Dimensional Viscous Shock-Layer Flows Over Blunt Bodies," AIAA J., Vol. 16, Dec. 1978, pp. 1279-1286.
- [38] Solomon, J. M., Ciment, M., Ferguson, R. E., Bell, J. B., and Wardlaw, A. B., Jr., "A Program for Computing Steady Inviscid Three-Dimensional Supersonic Flow on Reentry Vehicles, Vol. I, Analysis and Programming; Vol. II, User's Manual," Rept. No. NSWC/WOL/TR 77-28, February 1977.
- [39] Cleary, J. W., "Effects of Angle of Attack and Bluntness on Laminar Heating-Rate Distributions of a 15-deg Cone at a Mach Number of 10.6," NASA TND-5450, October 1969.
- [40] Zoby, E. V., Lee, K. P., Gupta, R. N., Thompson, R. A., Simmonds, A. L., "Viscous Shock-Layer Solutions with Nonequilibrium Chemistry for Hypersonic Flows past Slender Bodies," Journal of Spacecraft and Rockets, Vol. 26, No. 4, July-Aug. 1989, pp. 221-228.
- [41] Kang, S. -W., Jones, W. L., and Dunn, M. G., "Theoretical and Measured Electron-Density Distributions at High Altitudes," AIAA Journal, Vol. 11, No. 2, pp. 141-149, Feb. 1973.

- [42] Jones, W. L. and Cross, A. E., "Electrostatic Probe Measurements of Plasma Parameters for Two Reentry Flight Experiments at 25,000 ft/sec," NASA TN D-6617, April, 1972.
- [43] Moss, J. N., Cuda, V., and Simmonds, A. L., "Nonequilibrium Effects for Hypersonic Transitional Flows," AIAA Paper No. 87-0404, Jan. 1987.

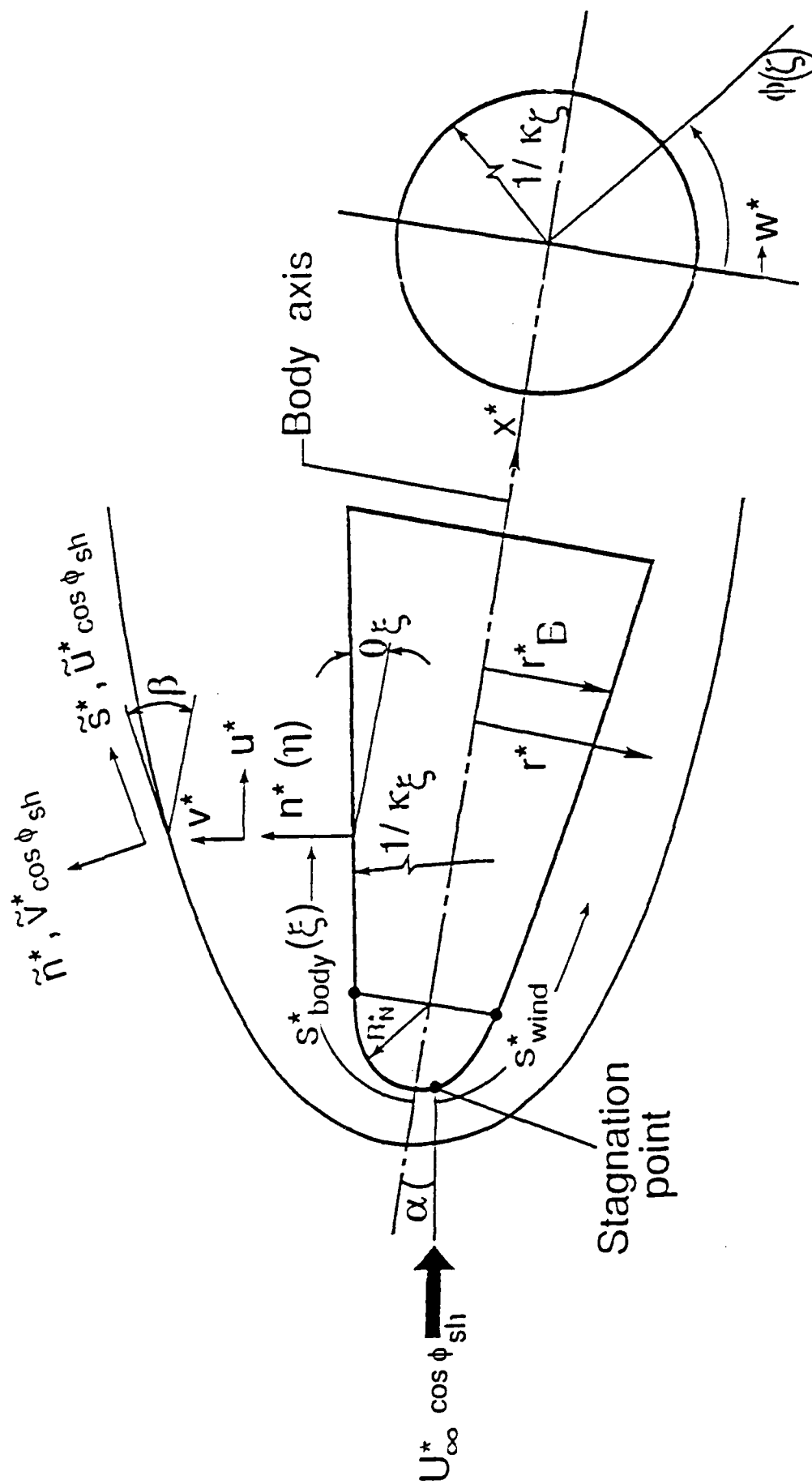


Figure 1. BODY AND SHOCK-ORIENTED COORDINATE SYSTEMS IN A MERIDIONAL PLANE

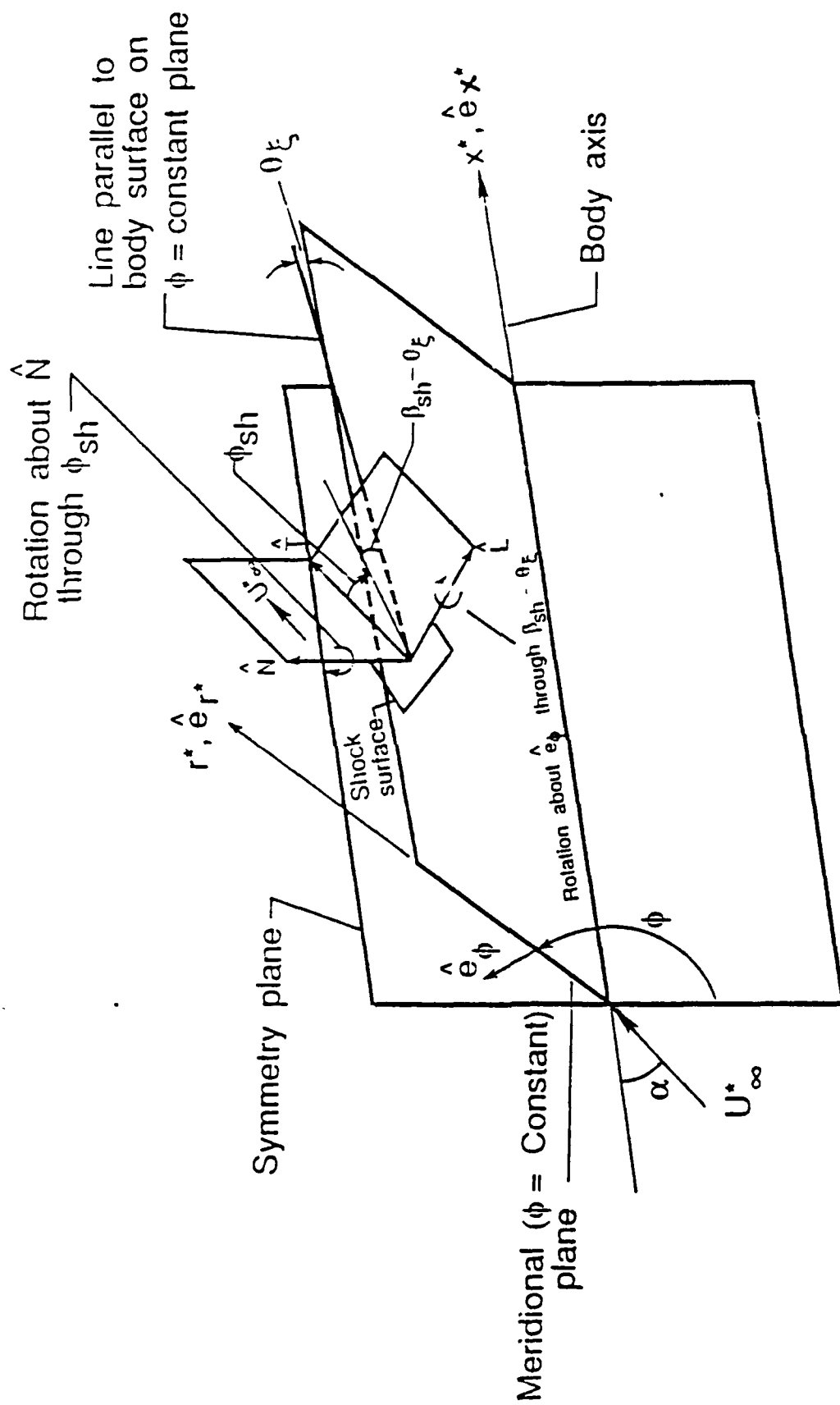


Figure 2a. SHOCK-WAVE NORMAL AND TANGENT VECTORS AND ROTATION ANGLES ABOUT \hat{n} AND e_ϕ VECTORS

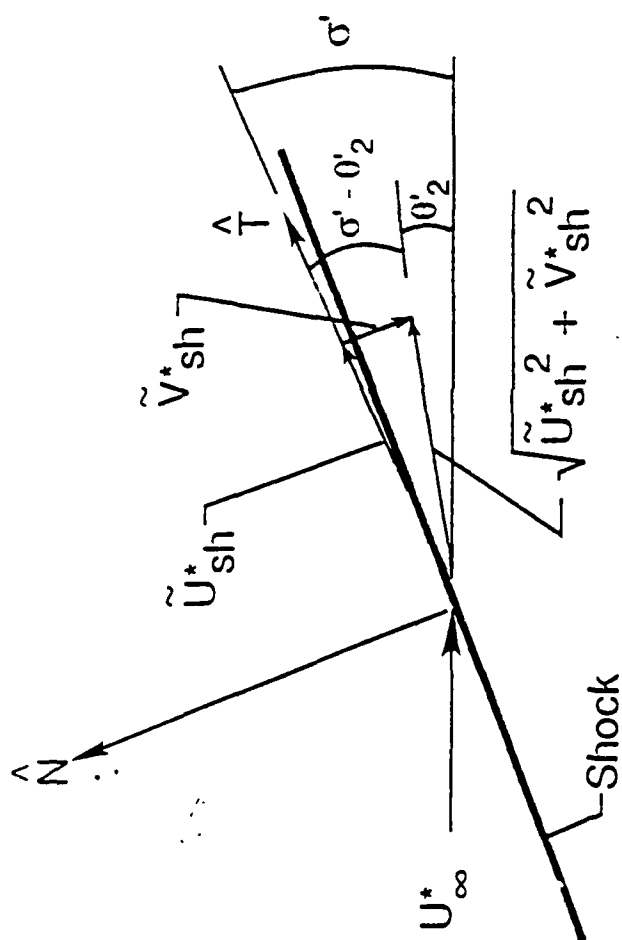


Figure 2b. SHOCK AND FLOW ANGLES IN THE \hat{N} - \hat{T} PLANE

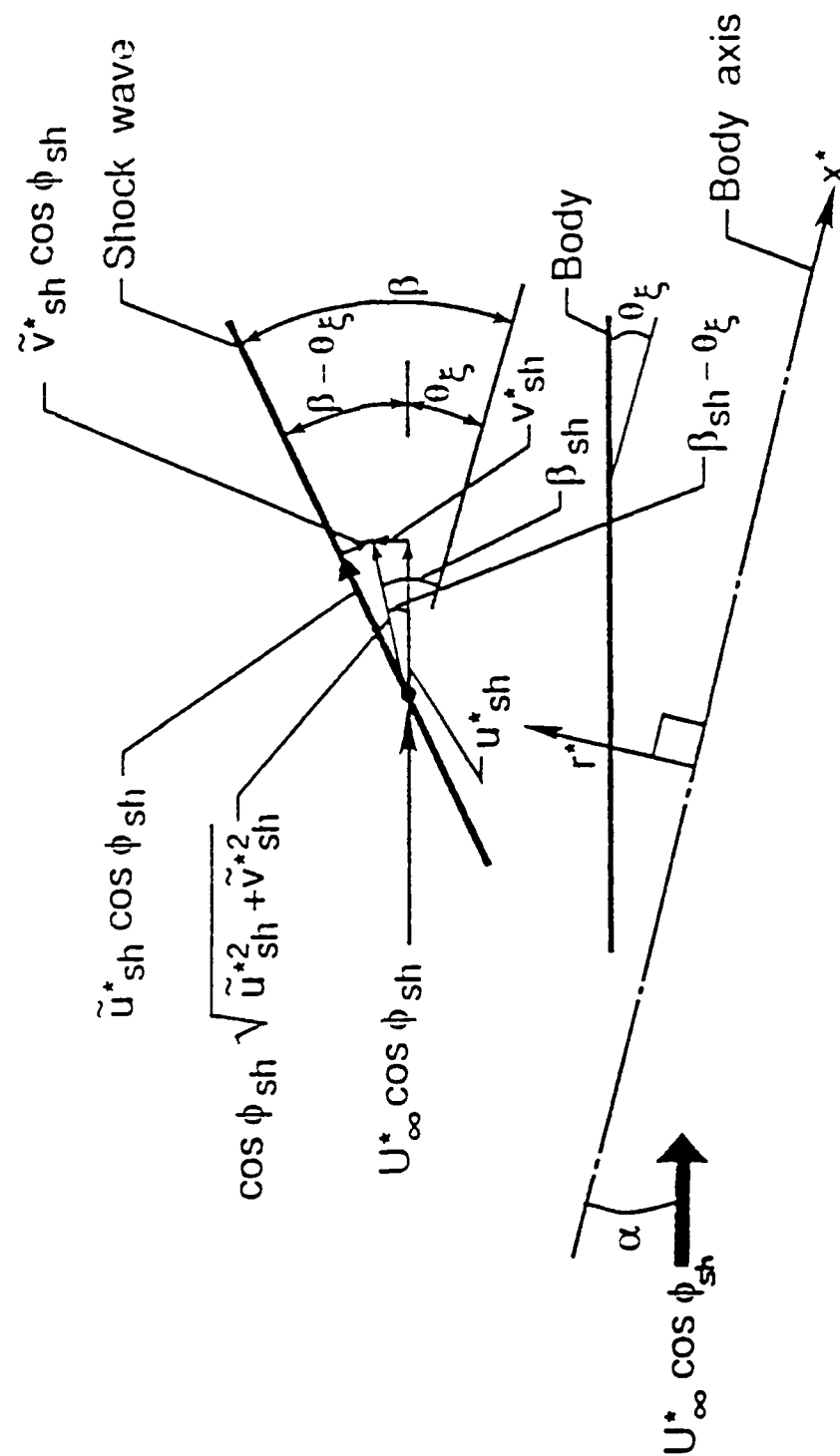


Figure 2c. VELOCITY COMPONENTS AND ANGLES EMPLOYED FOR SHOCK-BOUNDARY CONDITIONS IN A MERIDIONAL ($\phi = \text{CONSTANT}$) PLANE

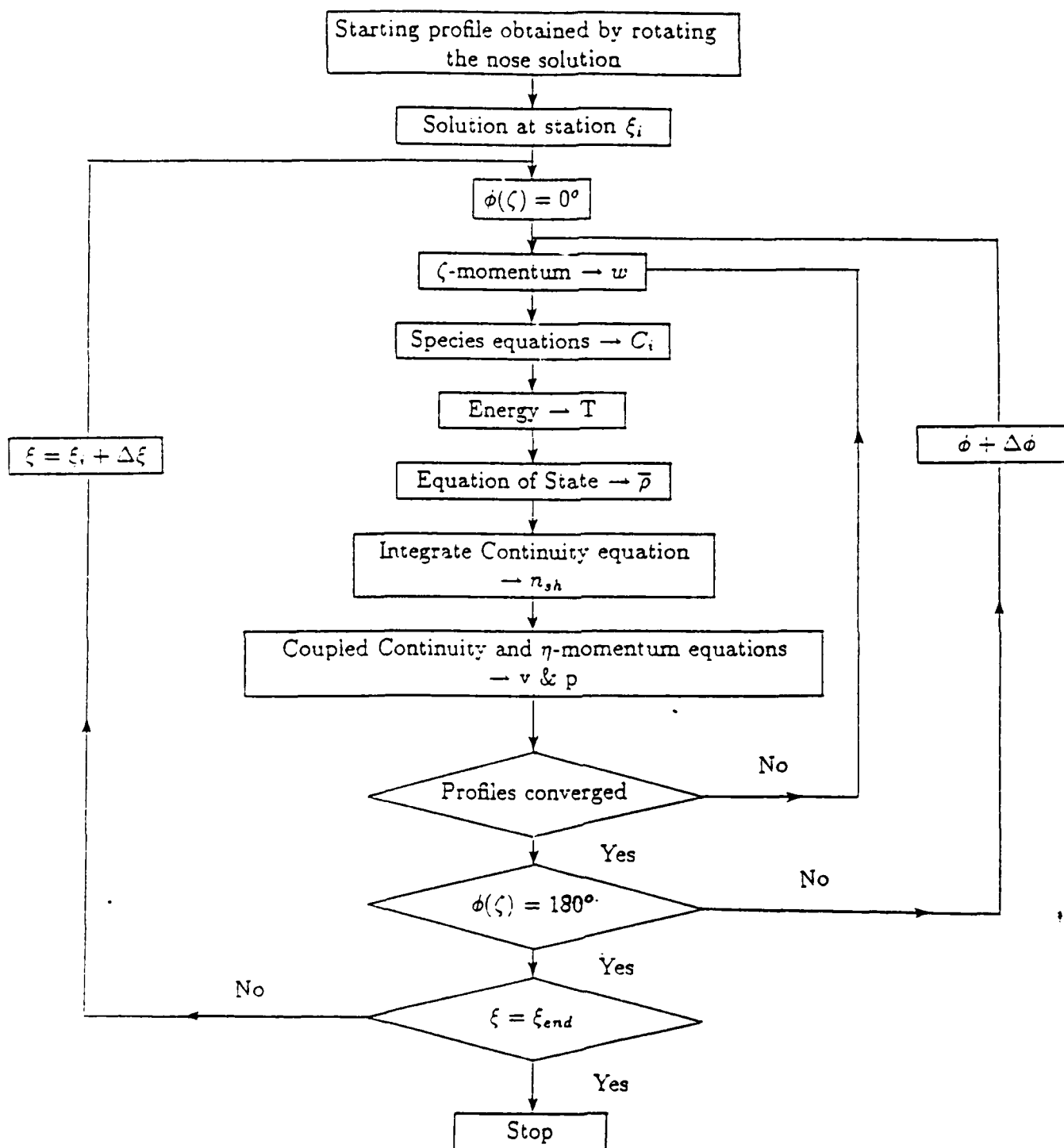


Figure 3. SOLUTION OF VISCOUS SHOCK LAYER EQUATIONS ON THE BODY (OR CONICAL PART)

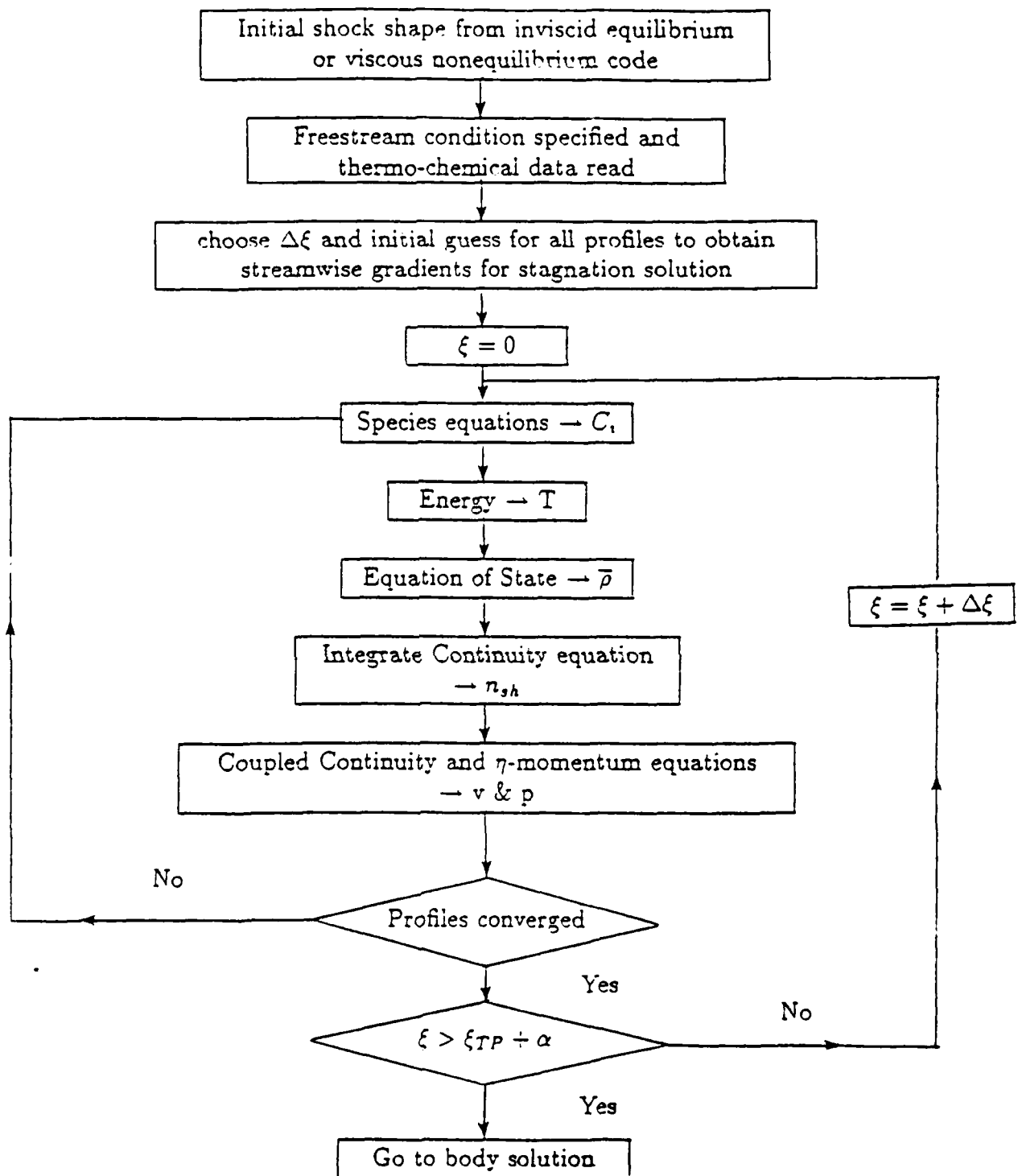


Figure 4. SOLUTION OF NOSE REGION (OR SPHERICAL PART)

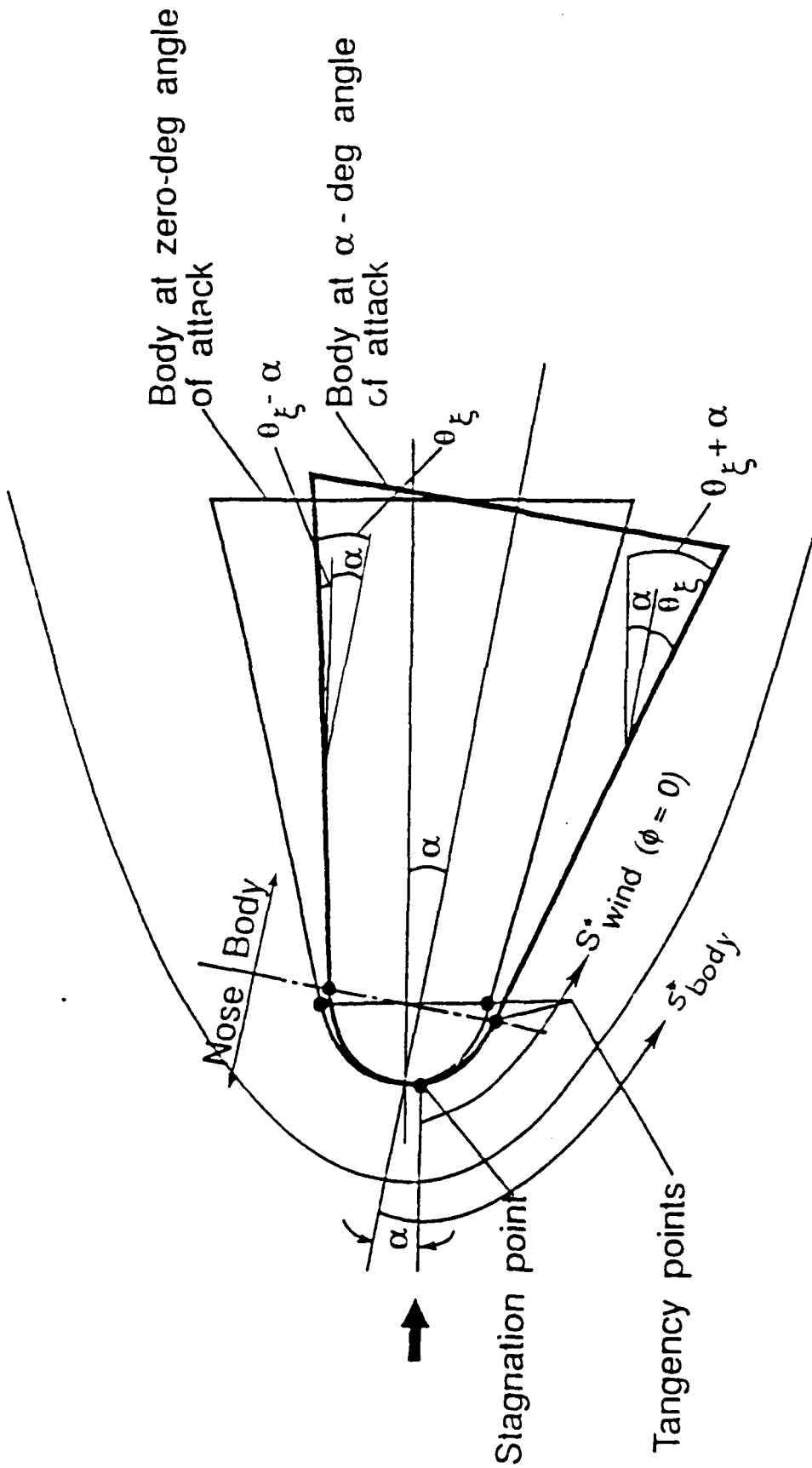


Figure 5. COORDINATES AND BODIES AT ZERO AND α -DEG ANGLES OF ATTACK

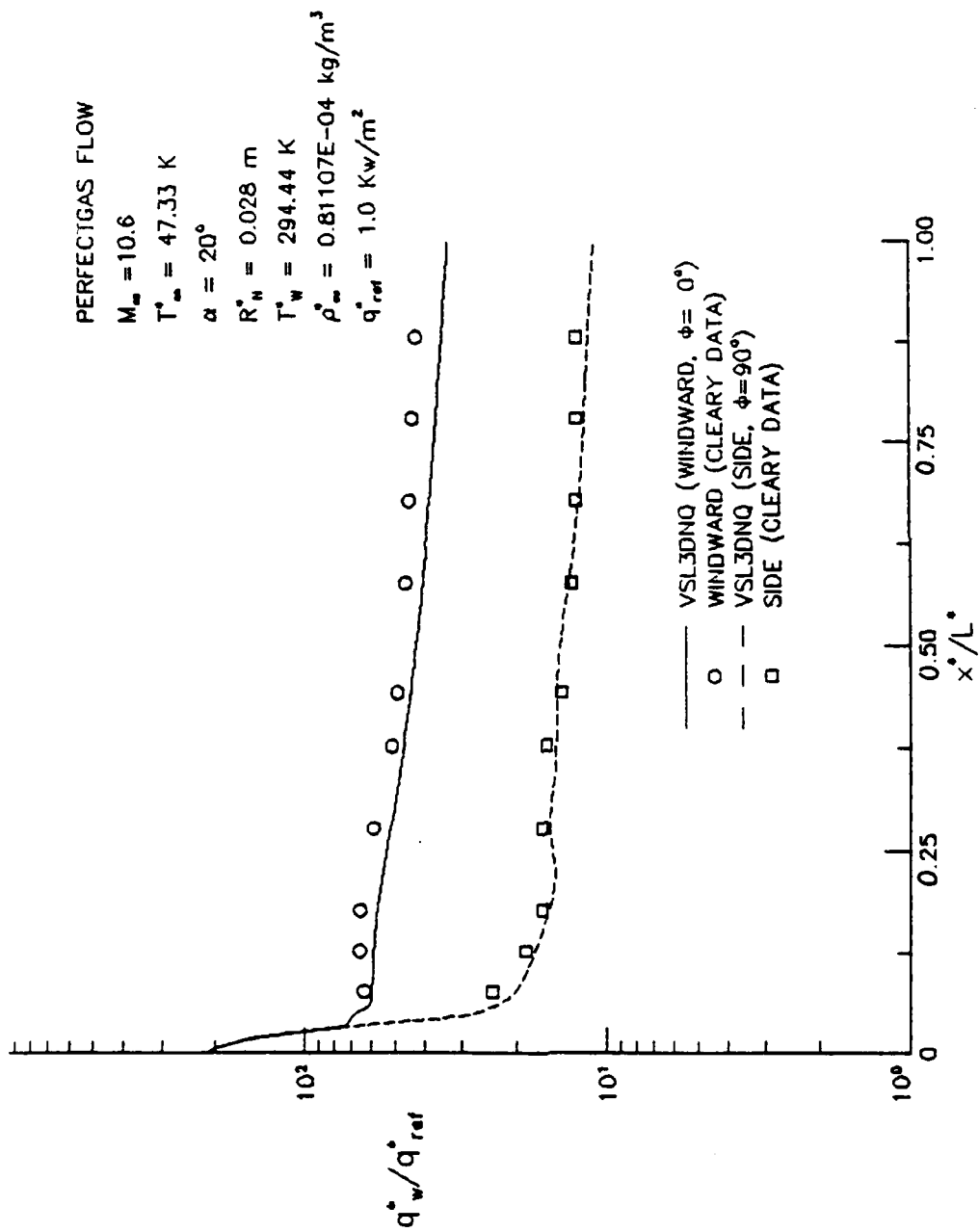


Figure 6 . COMPARISON OF SURFACE HEAT TRANSFER RATIO BETWEEN EXPERIMENTAL AND NUMERICAL RESULTS FOR A 15° SPHERE-CONE

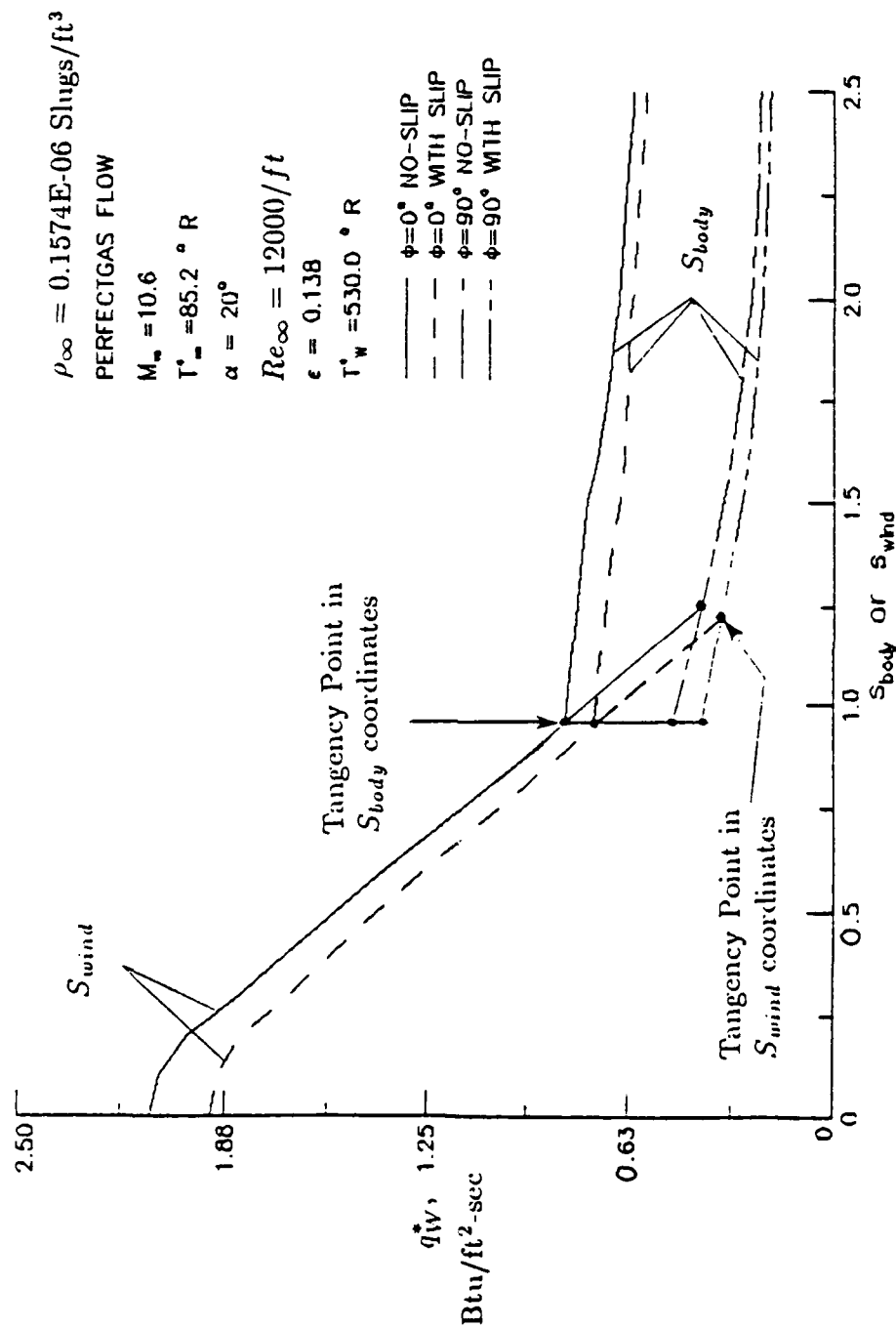


Figure 7. COMPARISON OF SURFACE HEAT TRANSFER AT DIFFERENT CROSSFLOW PLANES FOR A 15° SPHERE-CONE WITH AND WITHOUT SLIP

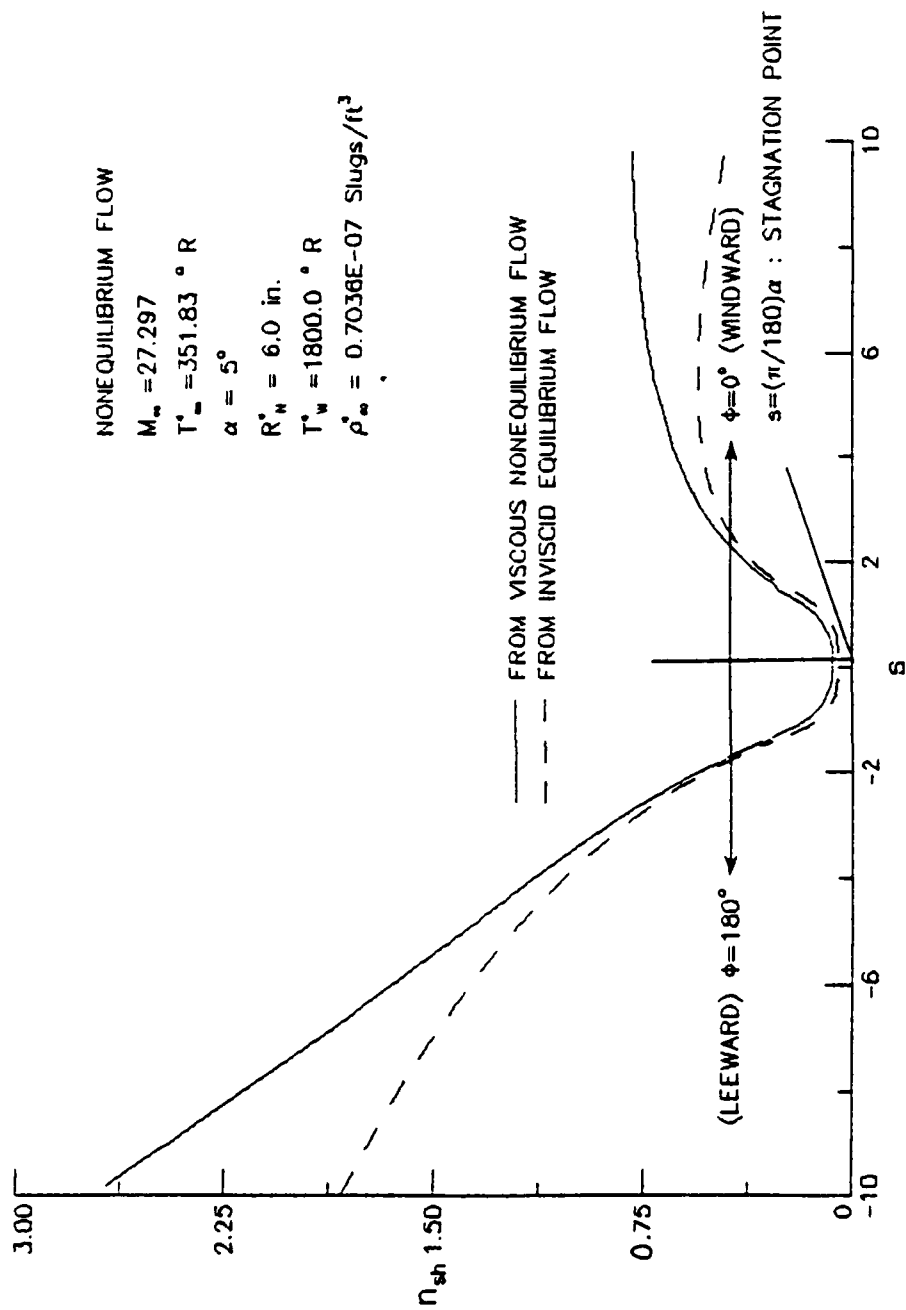


Figure 8 . COMPARISON OF INPUT SHOCK LAYER THICKNESS FOR A 9°
SPHERE-CONE WITH TWO DIFFERENT APPROACHES

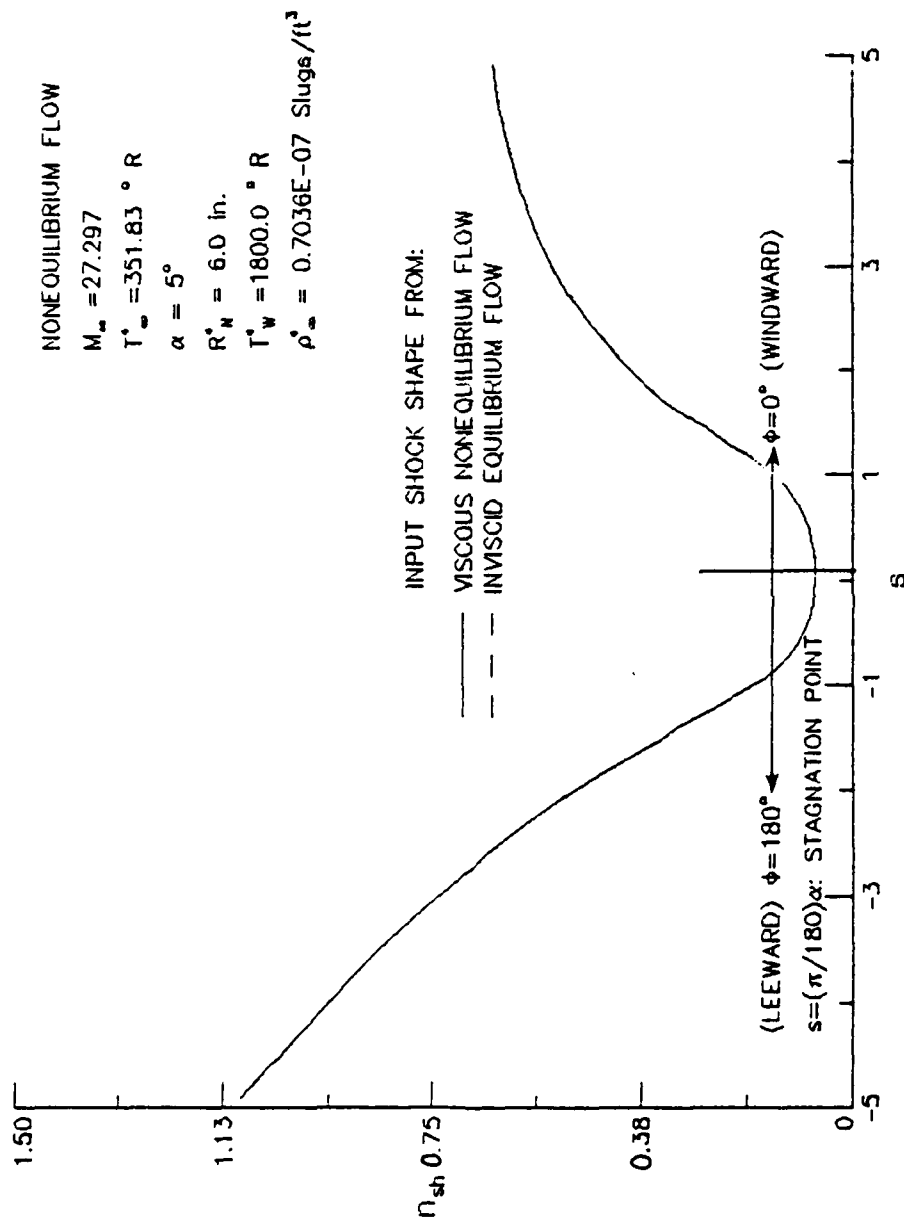


Figure 9 . COMPARISON OF OUTPUT SHOCK LAYER THICKNESS FOR A 9°
 SPHERE-CONE WITH TWO DIFFERENT APPROACHES

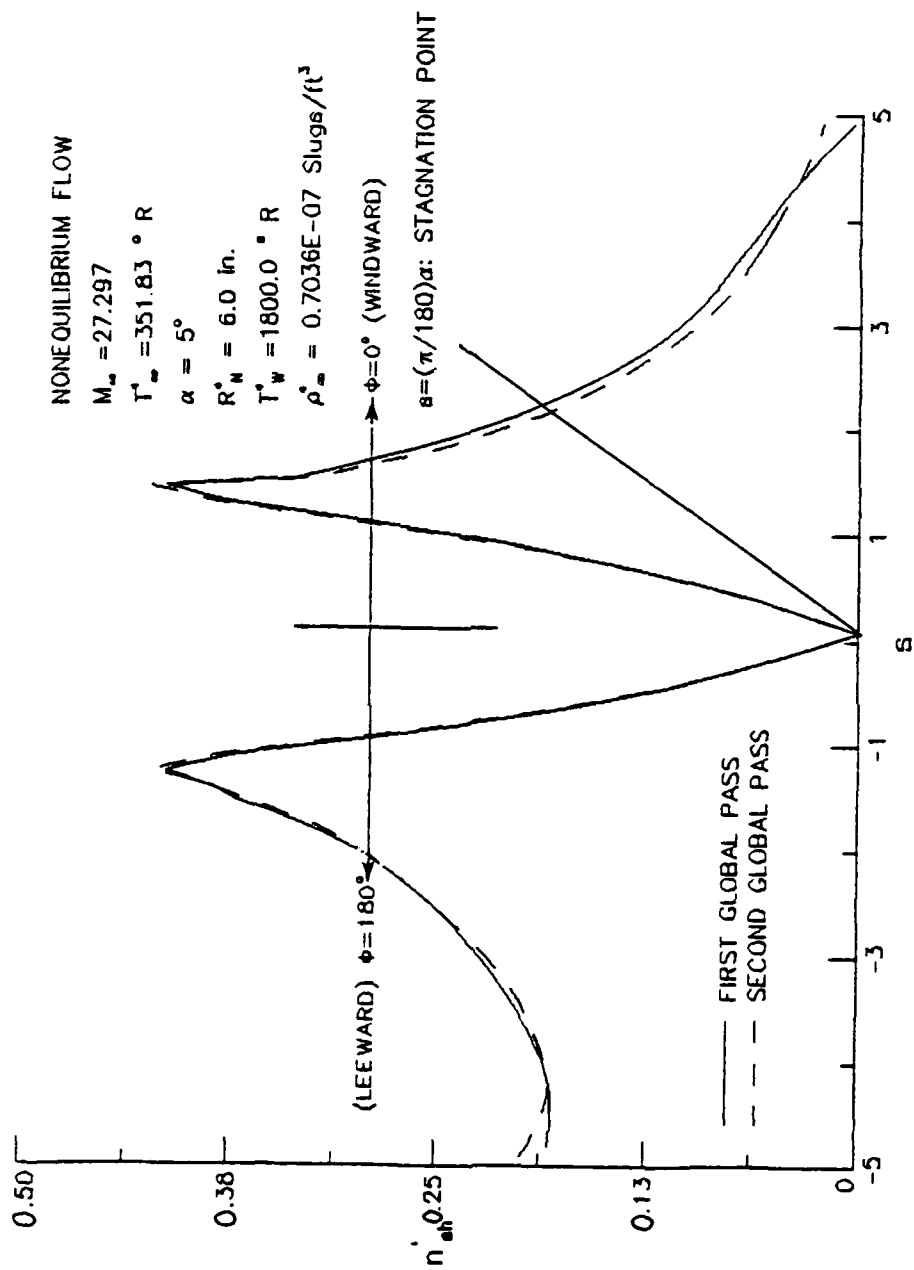


Figure 10 . SHOCK CONVERGENCE HISTORY FOR A 9° SPHERE-CONE USING
VISCIOUS NONEQUILIBRIUM INPUT SHOCK SHAPE

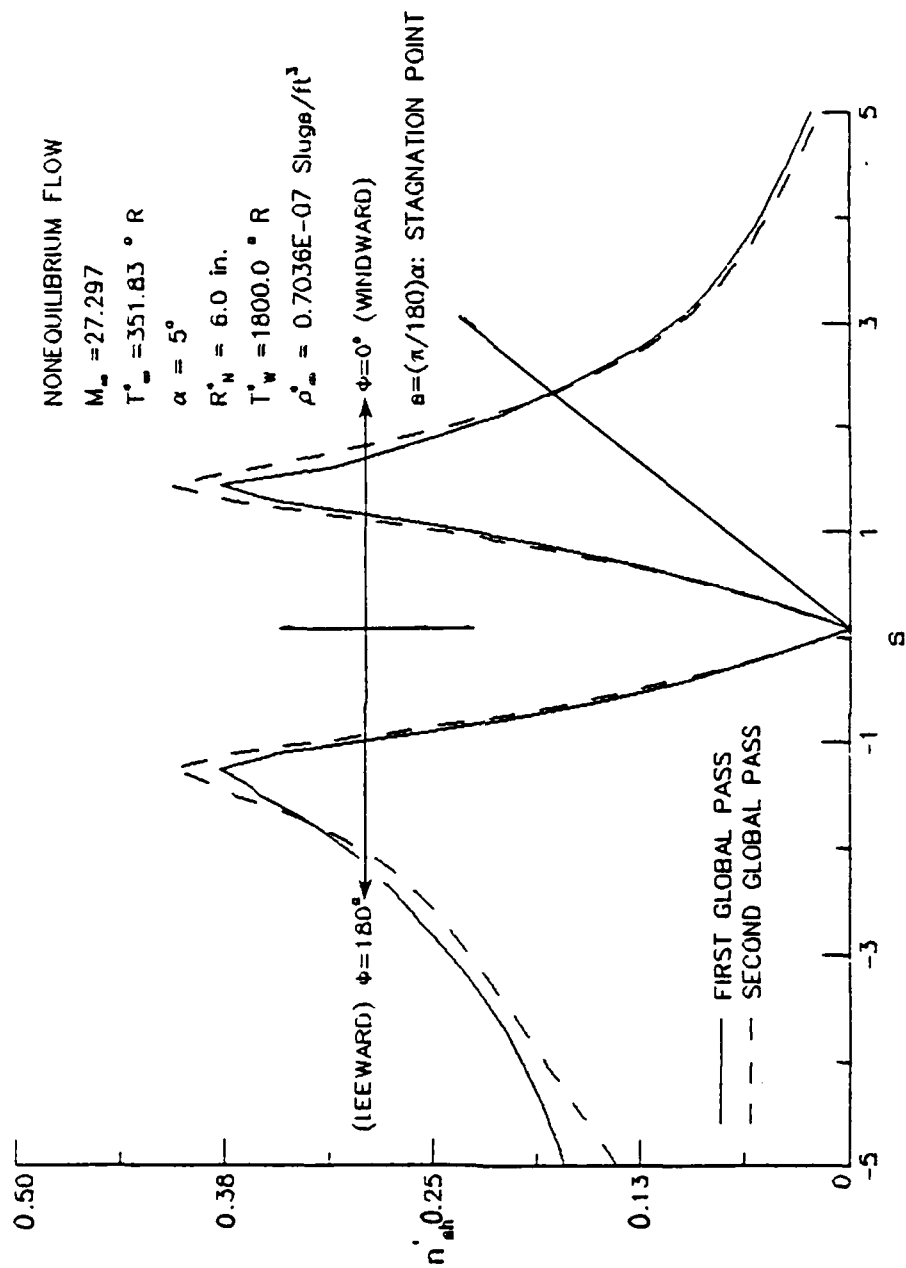


Figure 11 . SHOCK CONVERGENCE HISTORY FOR A 9° SPHERE-CONE USING INVISCID EQUILIBRIUM INPUT SHOCK SHAPE

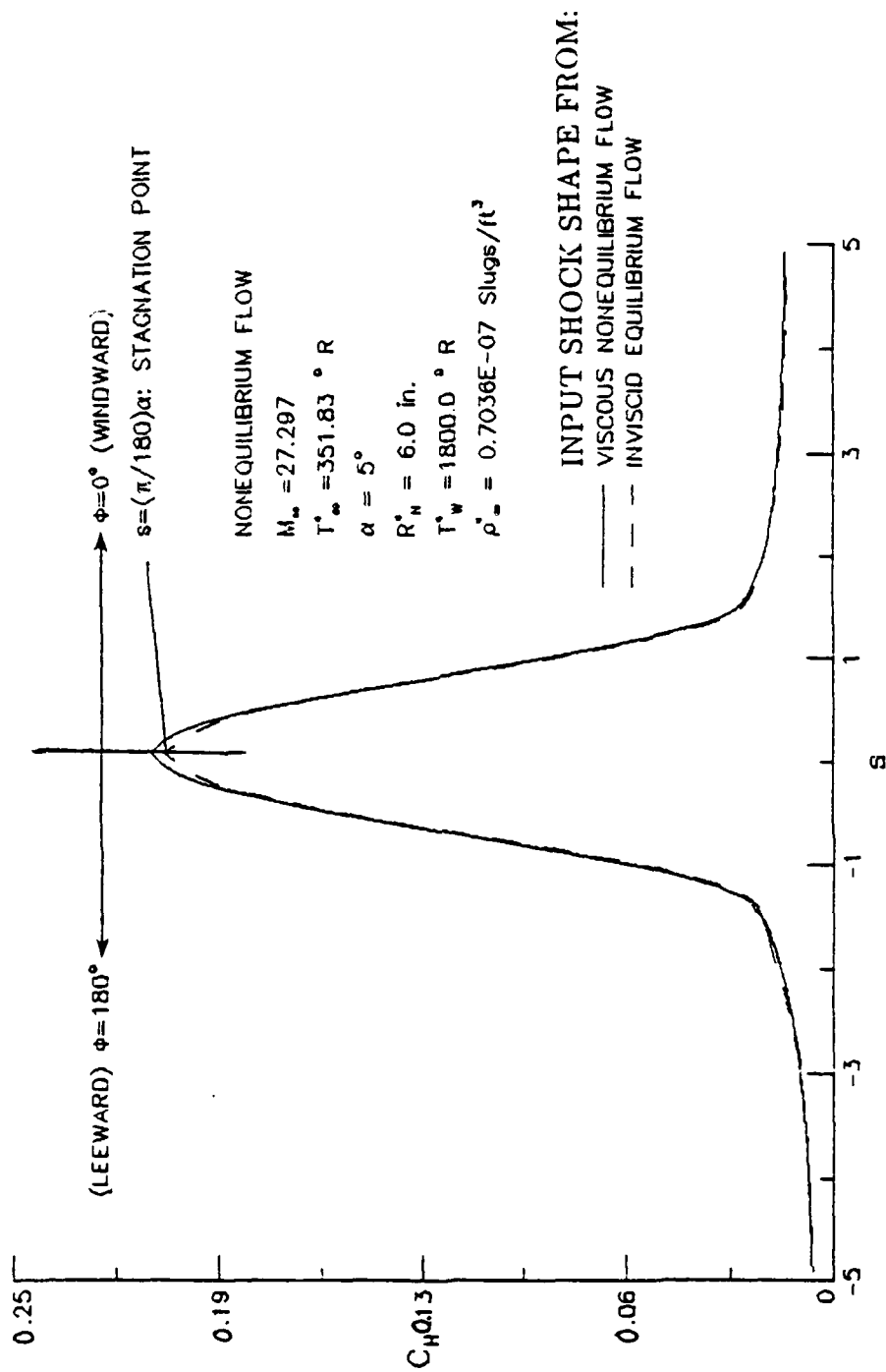


Figure 12 . COMPARISON OF HEAT TRANSFER COEFFICIENT FOR A 9° SPHERE -
 CONE WITH TWO DIFFERENT INPUT SHOCK SHAPES

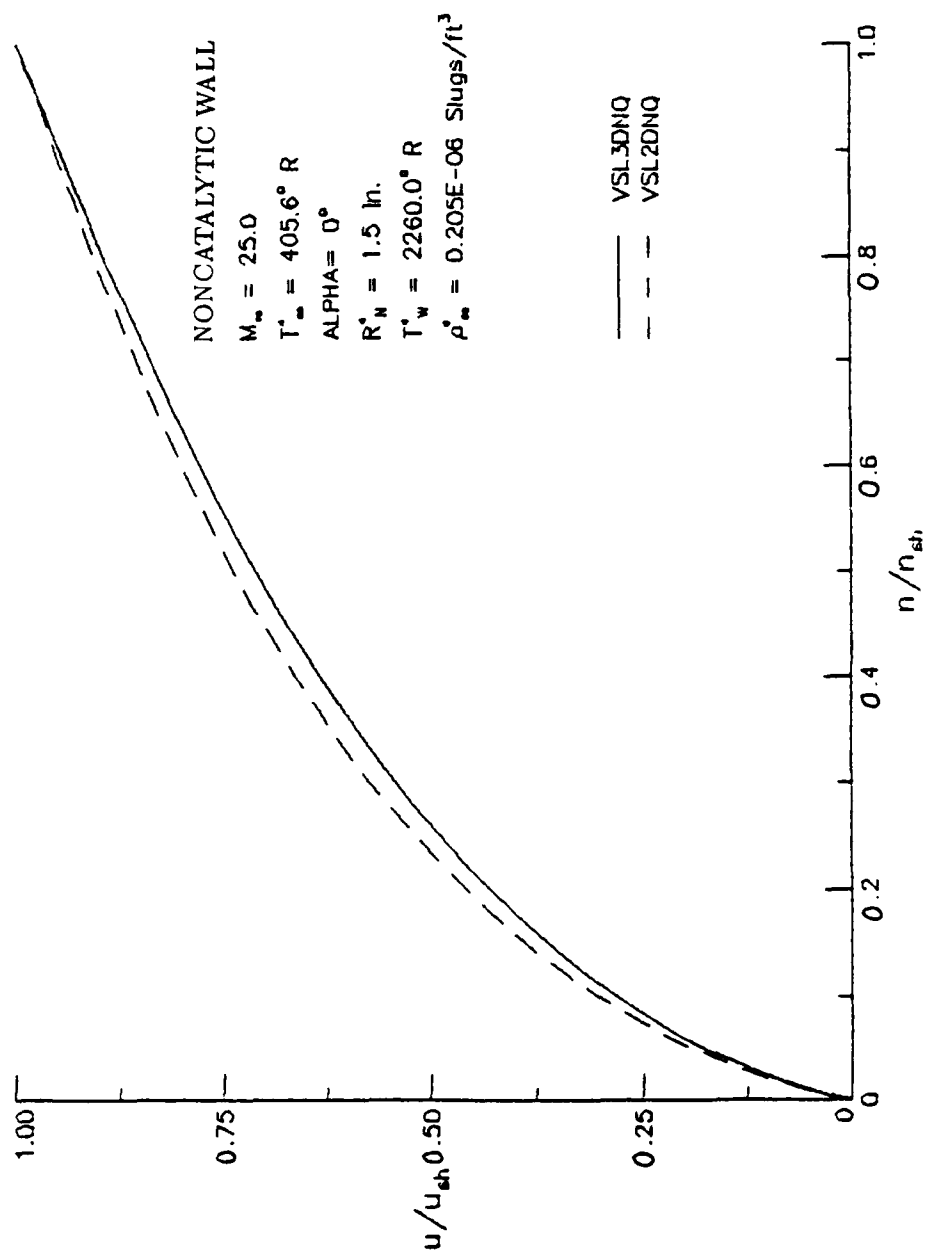


Figure 13 . COMPARISON OF VELOCITY DISTRIBUTION AT $s=0.0$ FOR A 20° SPHERE—CONE BETWEEN 2-D AND 3-D NONEQUILIBRIUM CODES

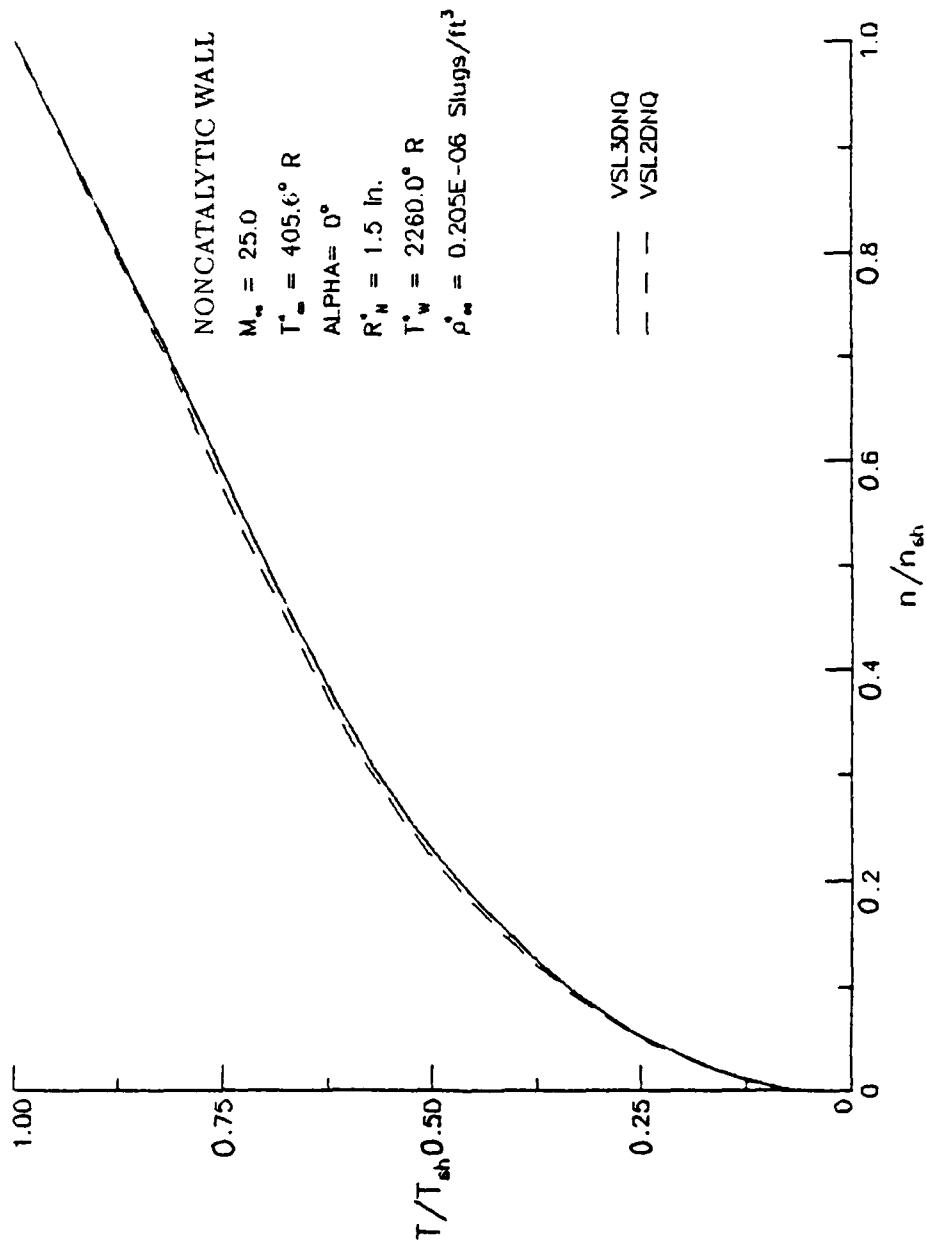


Figure 14 . COMPARISON OF TEMPERATURE DISTRIBUTION AT $\epsilon=0.0$ FOR A 20° SPHERE-CONE BETWEEN 2-D AND 3-D NONEQUILIBRIUM CODES

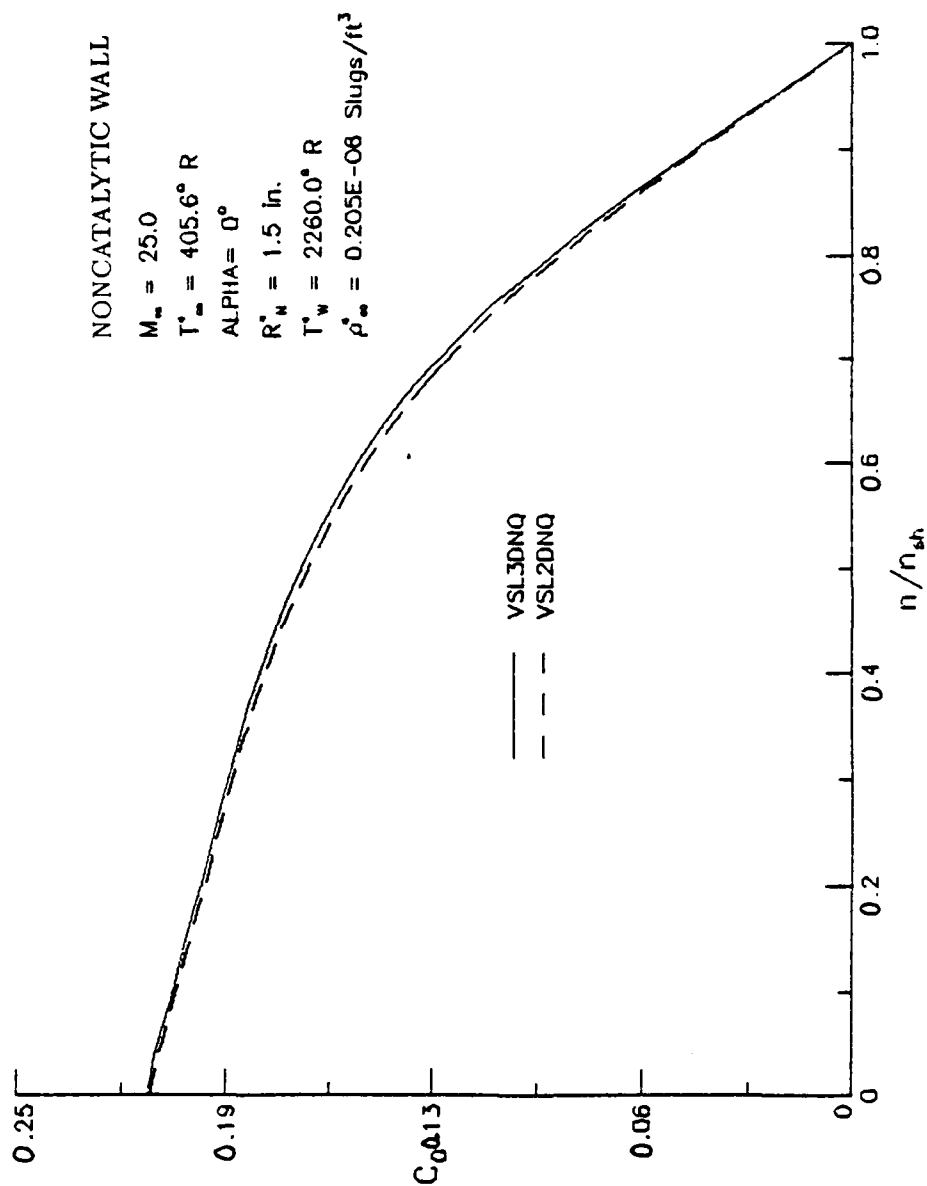


Figure 15 . COMPARISON OF MASS FRACTION DISTRIBUTION OF ATOMIC OXYGEN AT $s=0.0$ FOR A 20° SPHERE-CONE BETWEEN 2-D AND 3-D NON-EQUILIBRIUM CODES

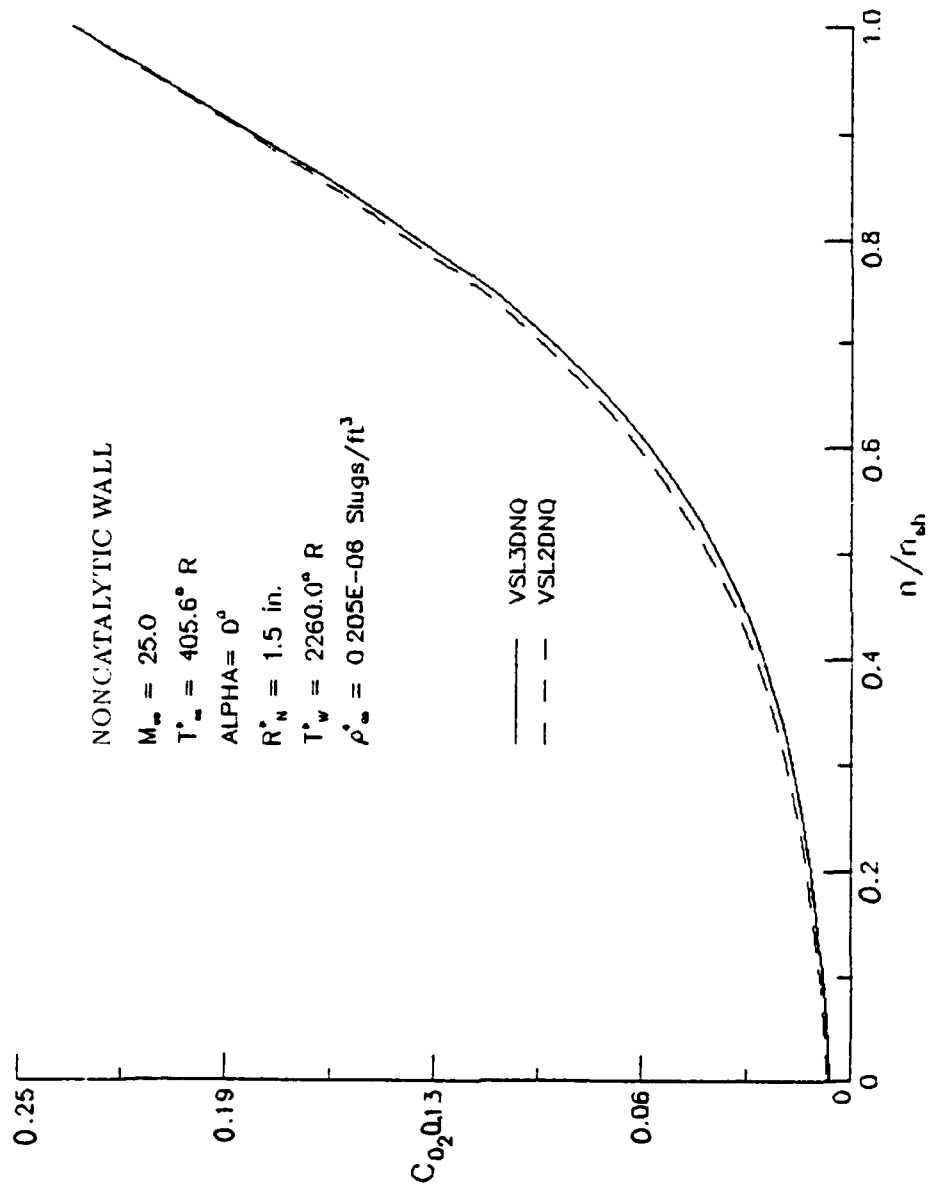


Figure 16 . COMPARISON OF MASS FRACTION DISTRIBUTION OF MOLECULAR OXYGEN AT $s=0.0$ FOR A 20° SPHERE-CONE BETWEEN 2-D AND 3-D NON-EQUILIBRIUM CODES

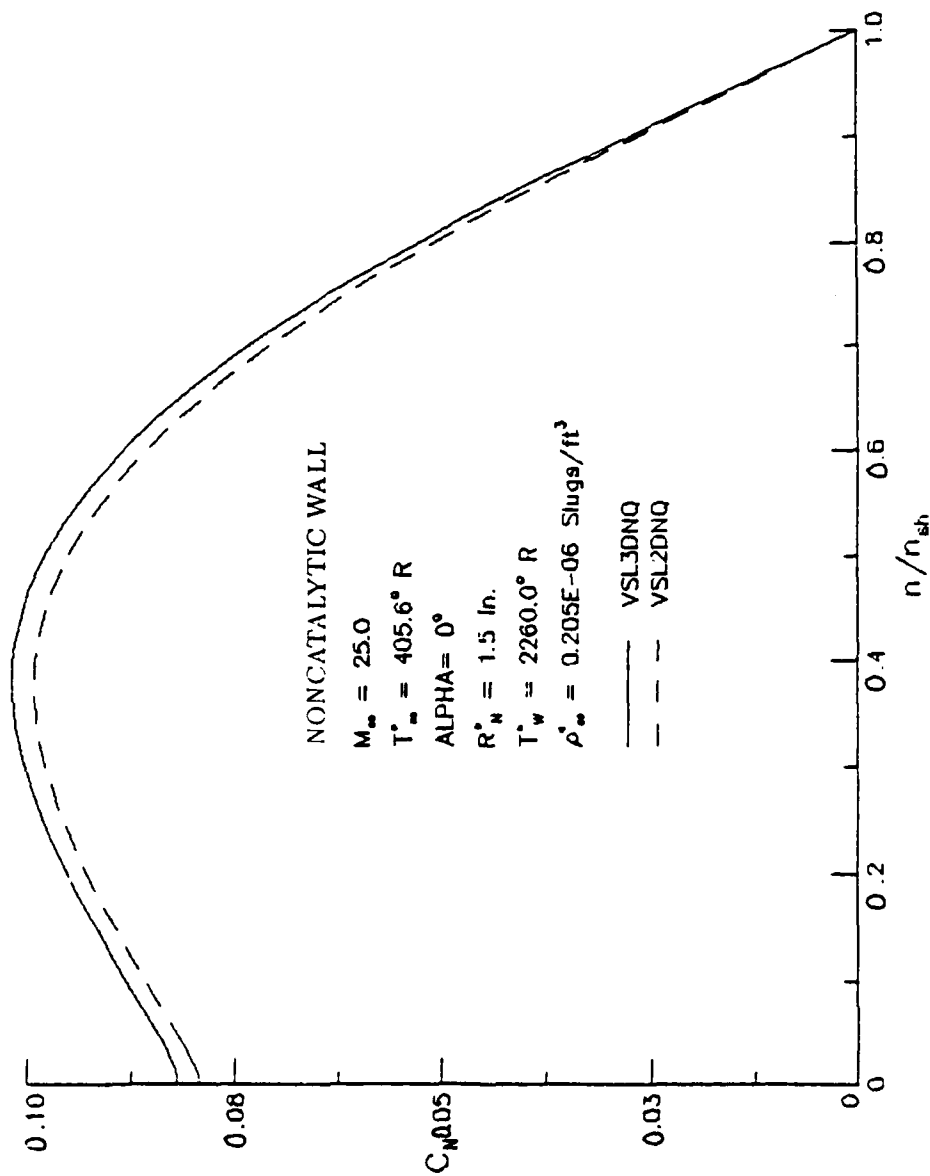


Figure 17 . COMPARISON OF MASS FRACTION DISTRIBUTION OF ATOMIC NITROGEN AT $s=0.0$ FOR A 20° SPHERE-CONE BETWEEN 2-D AND 3-D NON-EQUILIBRIUM CODES

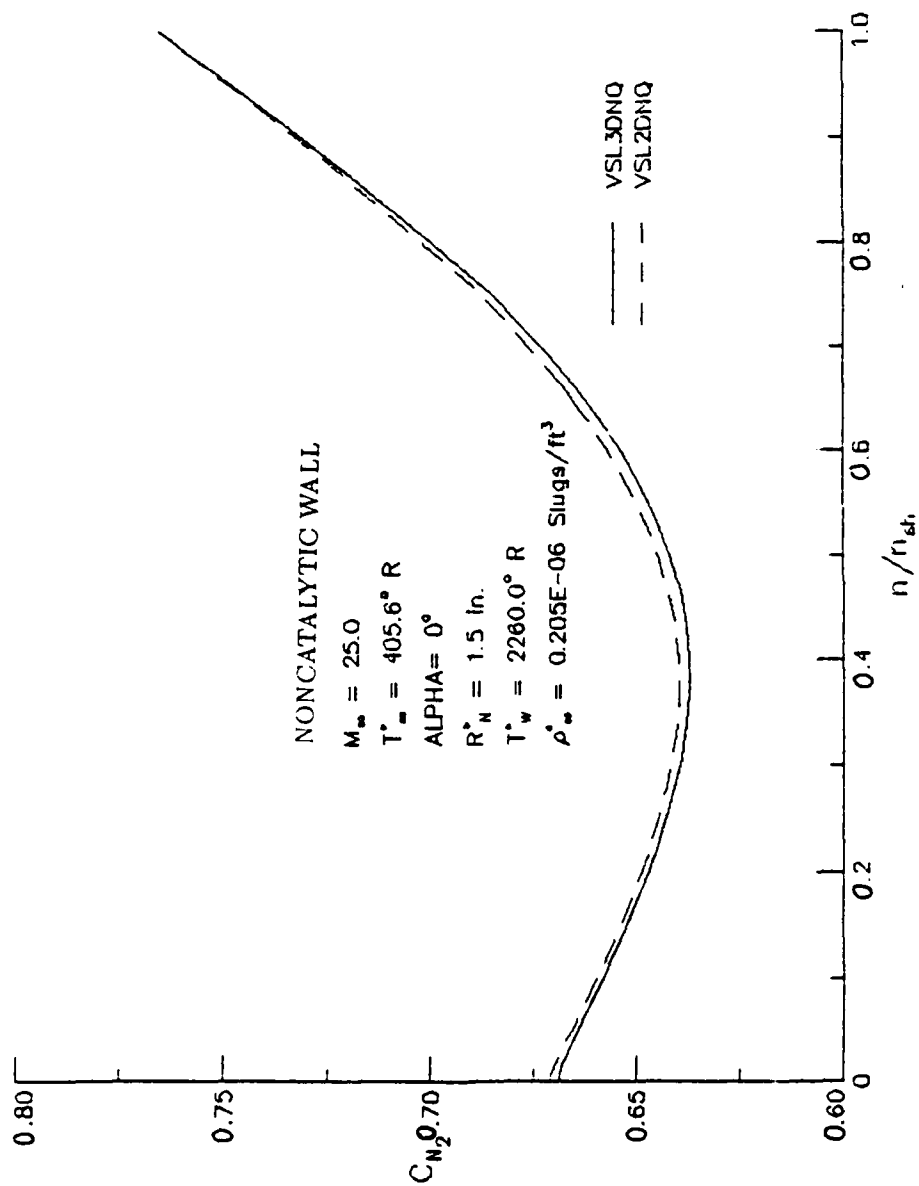


Figure 18 . COMPARISON OF MASS FRACTION DISTRIBUTION OF MOLECULAR NITROGEN AT $s=0.0$ FOR A 20° SPHERE-CONE BETWEEN 2-D AND 3-D NON-EQUILIBRIUM CODES

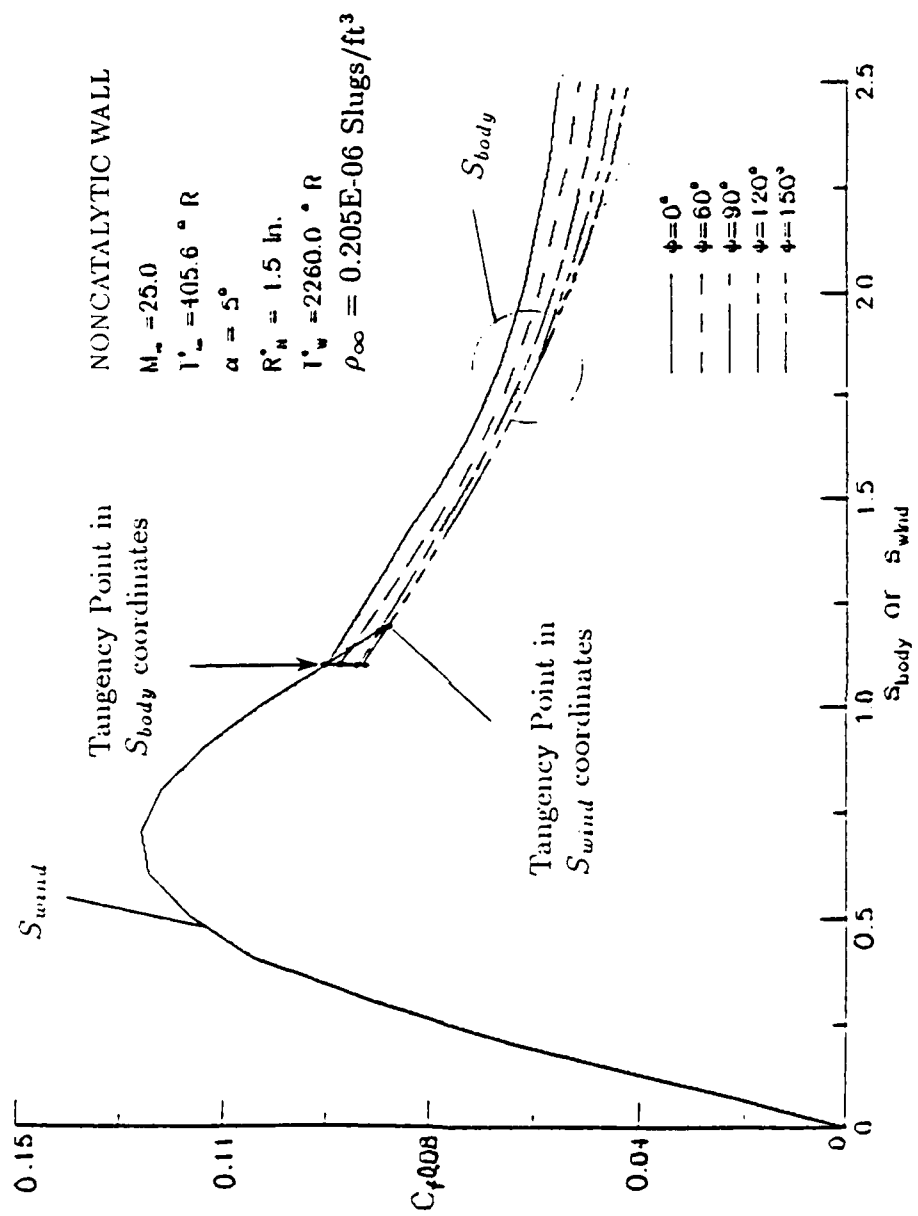


Figure 19. SKIN-FRICTION COEFFICIENT FOR A 20° SPHERE-CONE AT DIFFERENT CROSSFLOW PLANES - NO SLIP

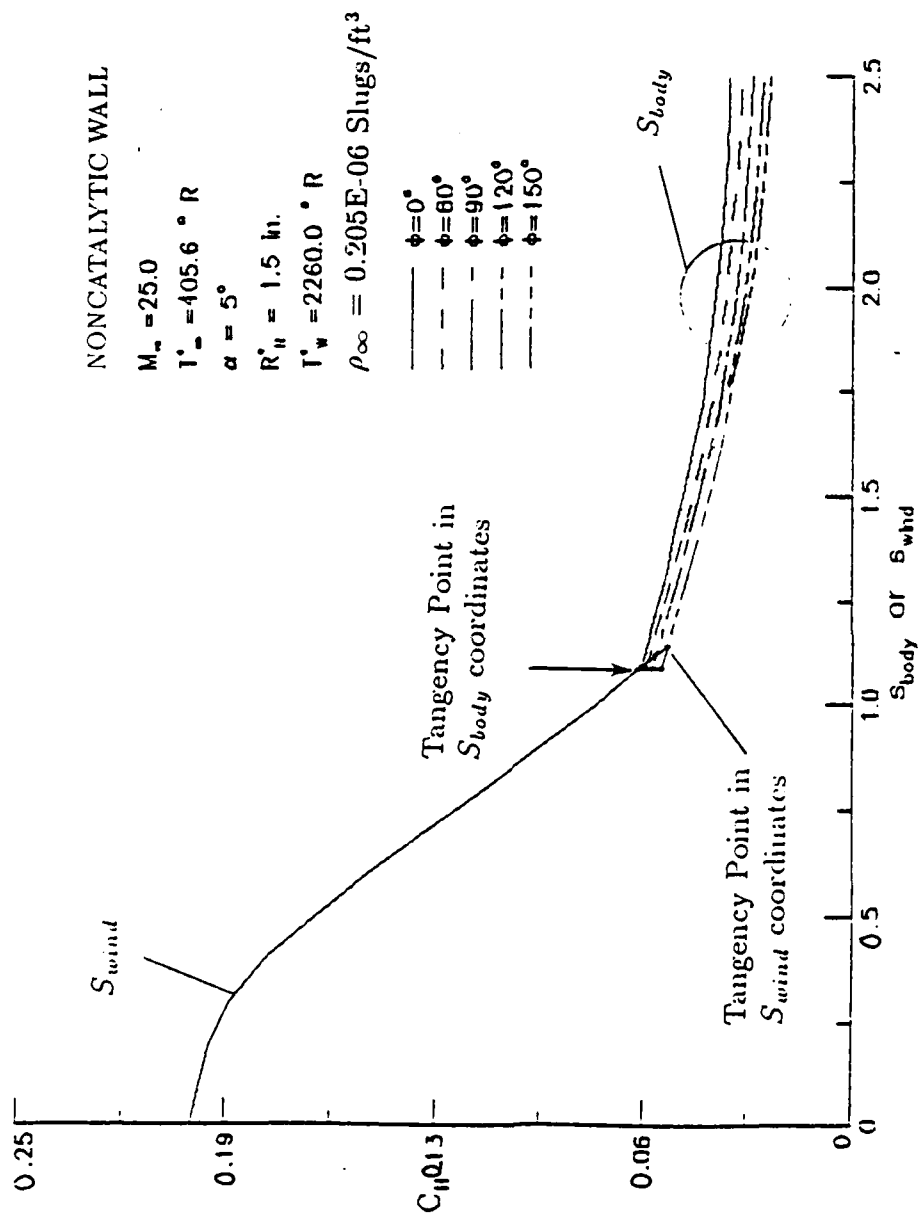


Figure 20 . SURFACE HEAT TRANSFER COEFFICIENT FOR A 20° SPHERE-CONE AT DIFFERENT CROSSFLOW PLANES - NO SLIP

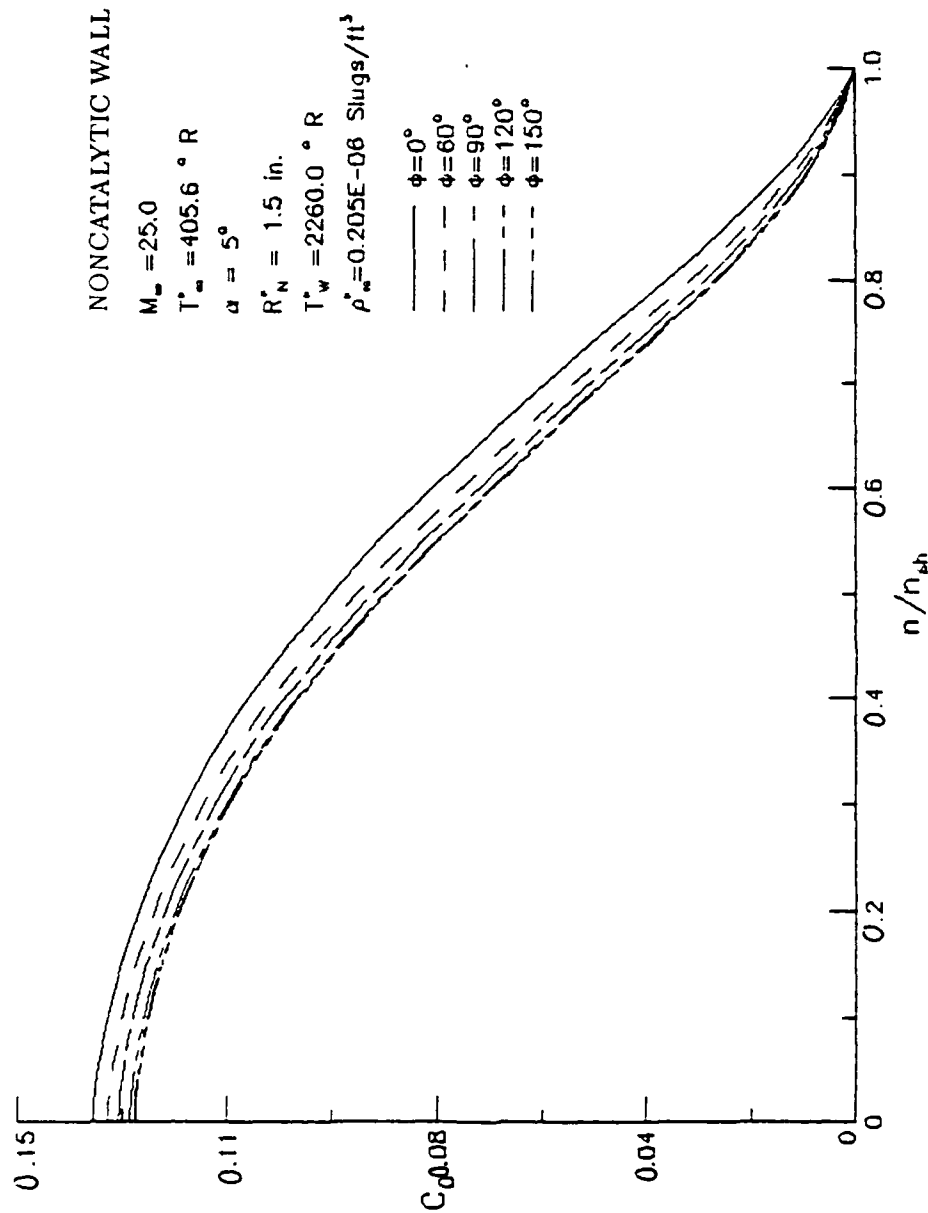


Figure 21. MASS FRACTION DISTRIBUTION FOR ATOMIC OXYGEN AT $s=2.02$ FOR A 20° SPHERE-CONE AT DIFFERENT CROSSFLOW PLANES-NO SLIP

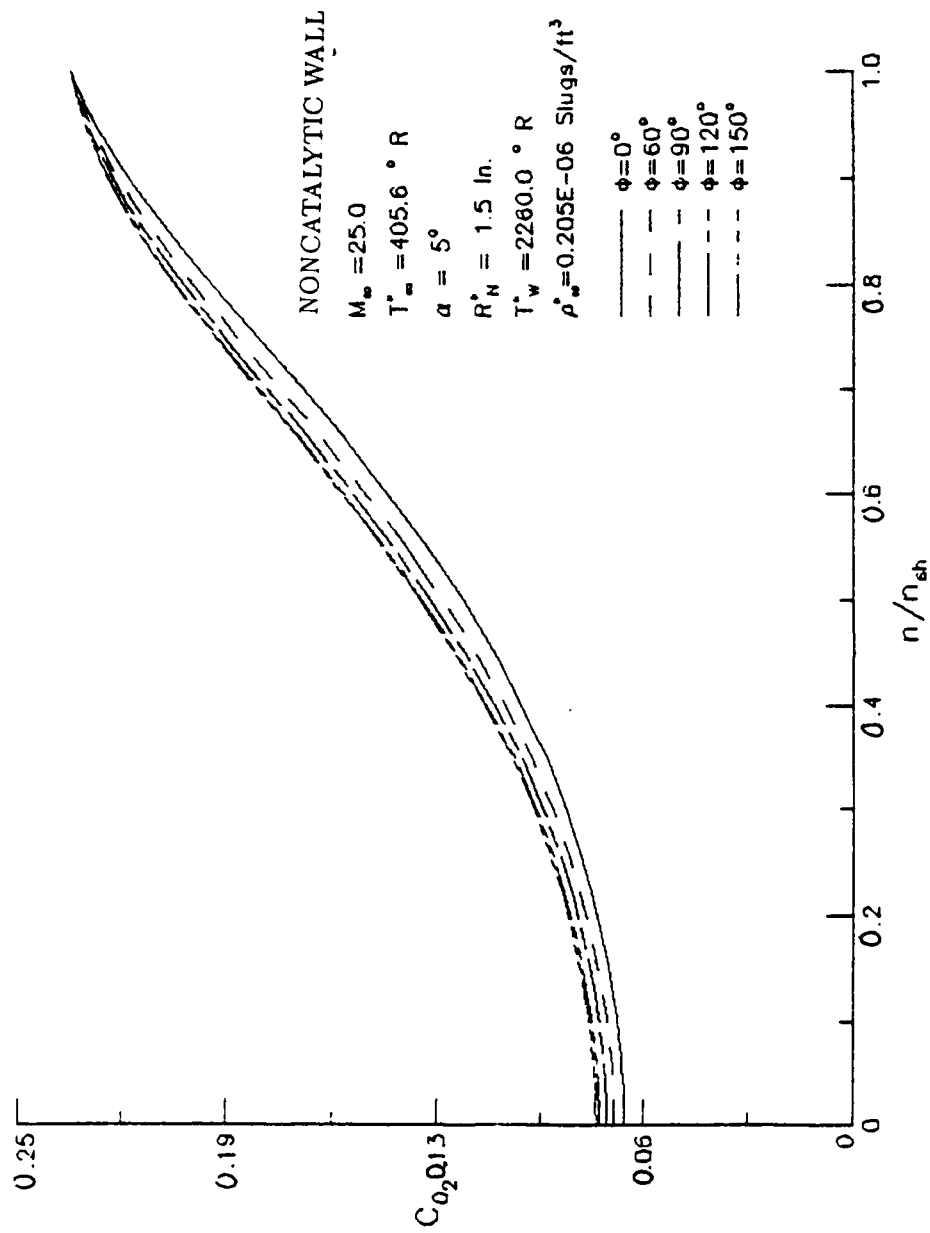


Figure 22. MASS FRACTION DISTRIBUTION FOR MOLECULAR OXYGEN AT $s=2.02$ FOR A
20° SPHERE-CONE AT DIFFERENT CROSSFLOW PLANES-NO SLIP

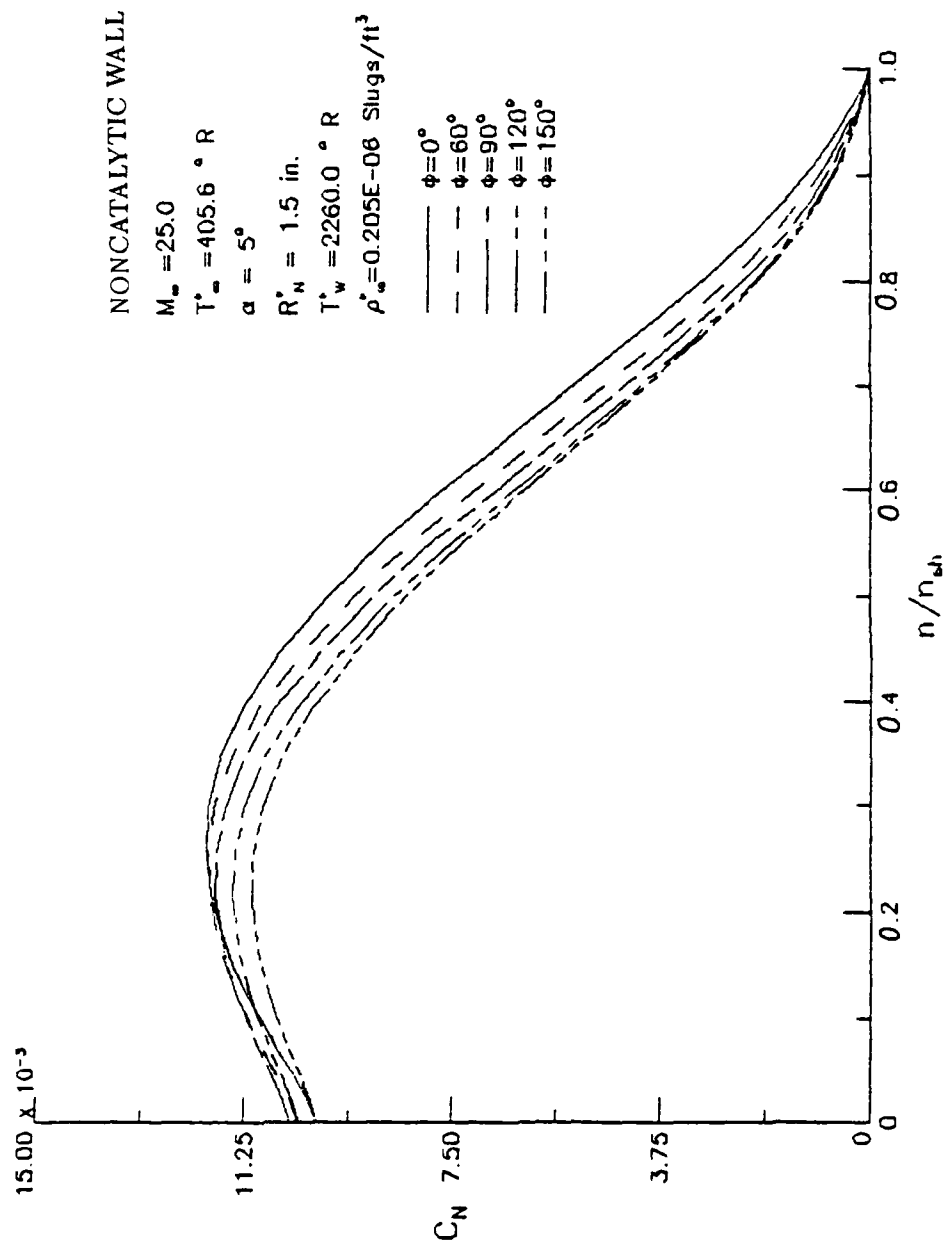


Figure 23. MASS FRACTION DISTRIBUTION FOR ATOMIC NITROGEN AT $s=2.02$ FOR A
 20° SPHERE-CONE AT DIFFERENT CROSSFLOW PLANES-NO SLIP

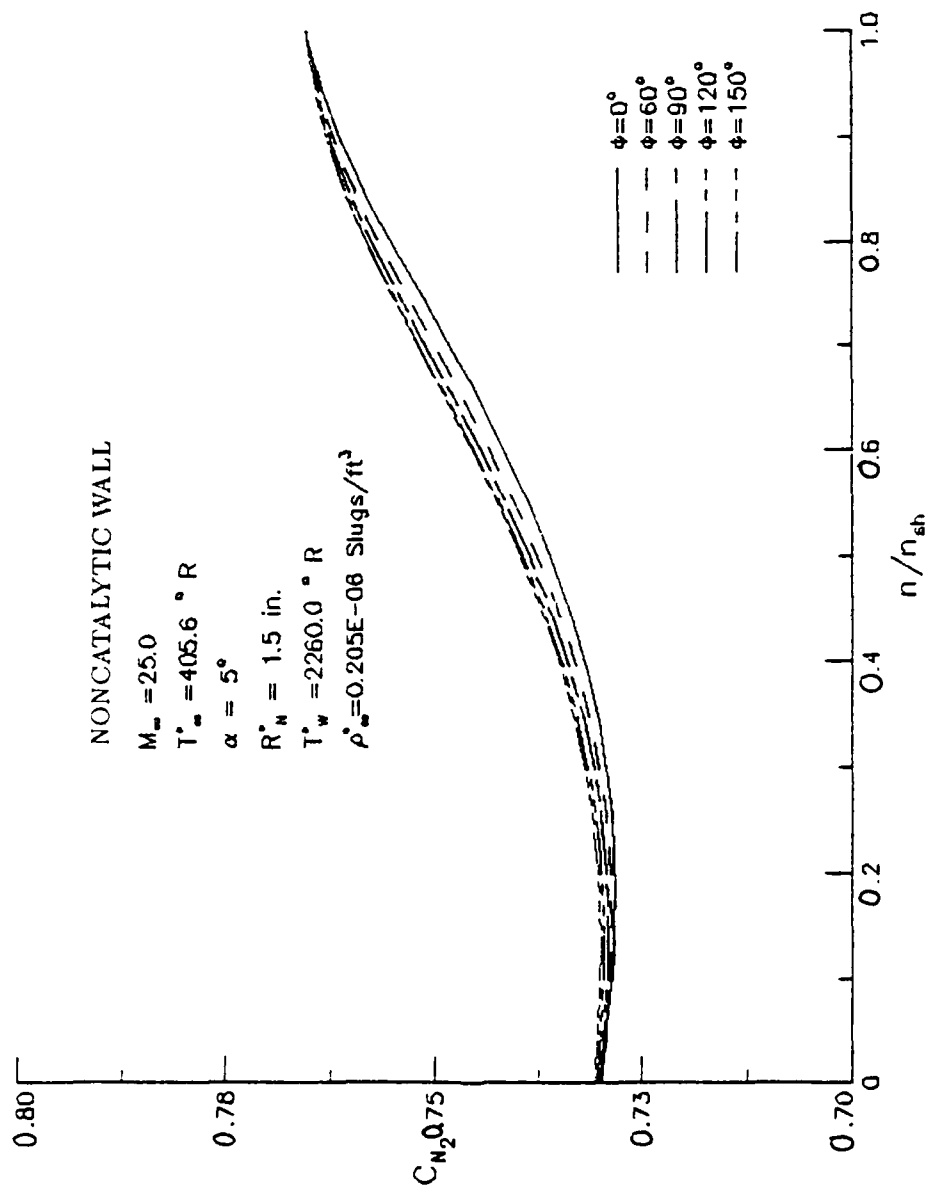


Figure 24. MASS FRACTION DISTRIBUTION FOR MOLECULAR NITROGEN AT $s=2.02$ FOR
A 20° SPHERE-CONE AT DIFFERENT CROSSFLOW PLANES-NO SLIP

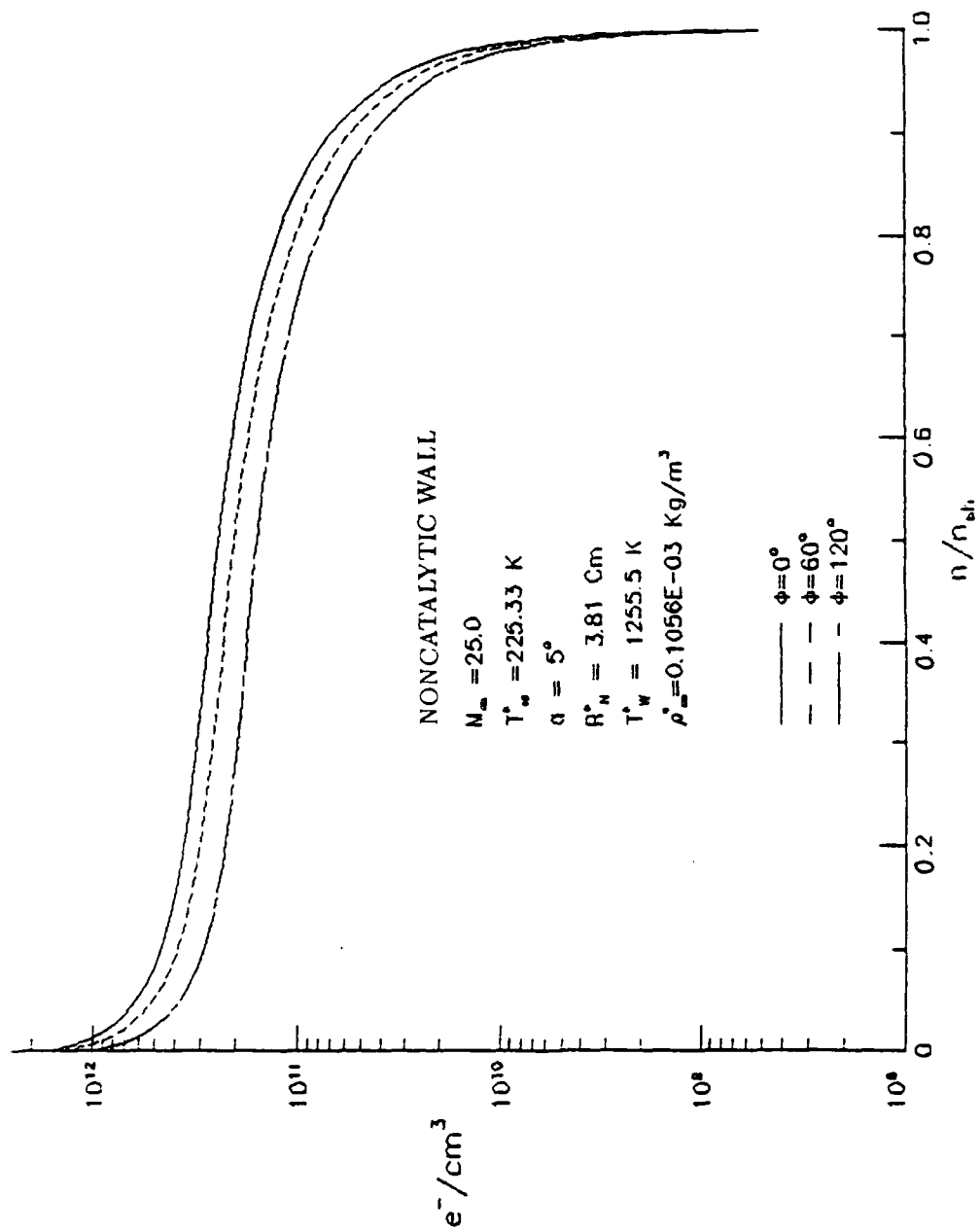


Figure 25. ELECTRON NUMBER DENSITIES AT $s=2.02$ FOR A 20° SPHERE-CONE
AT DIFFERENT CROSSFLOW PLANES

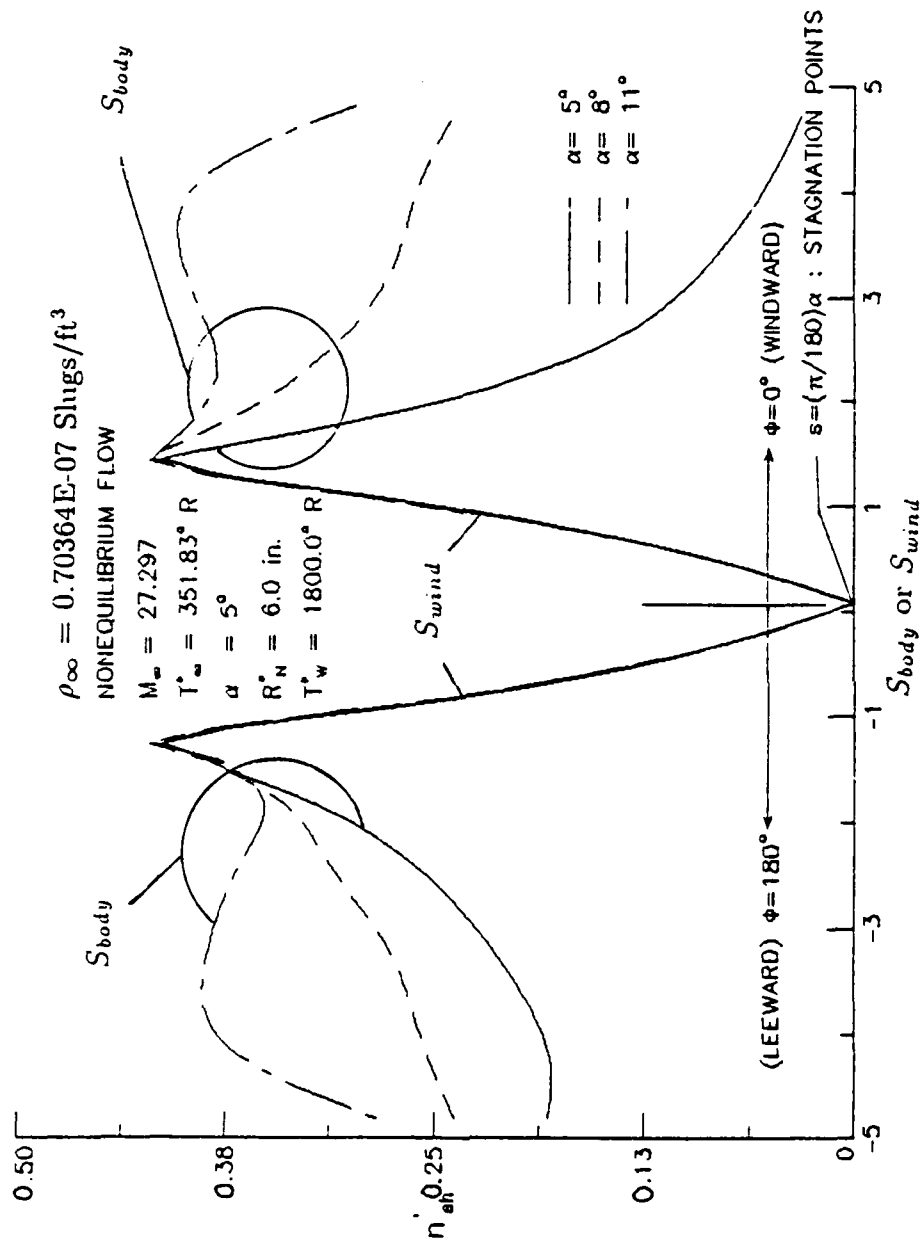


Figure 26 . COMPARISON OF SHOCK LAYER THICKNESS GRADIENT FOR A 9° SPHERE-CONE AT DIFFERENT ANGLES OF ATTACK

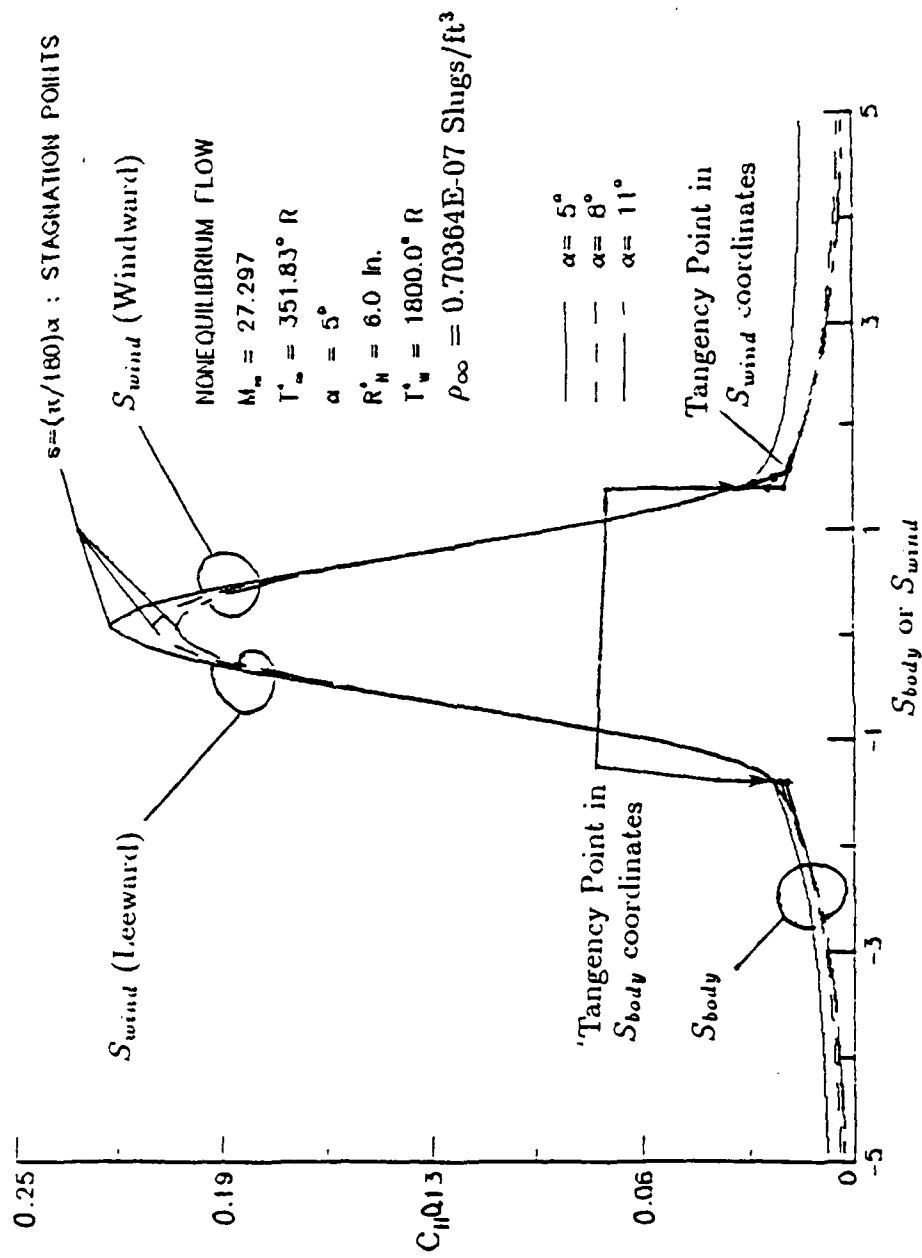


Figure 27 . COMPARISON OF HEAT TRANSFER COEFFICIENT FOR A 9° SPHERE-CONE AT DIFFERENT ANGLES OF ATTACK

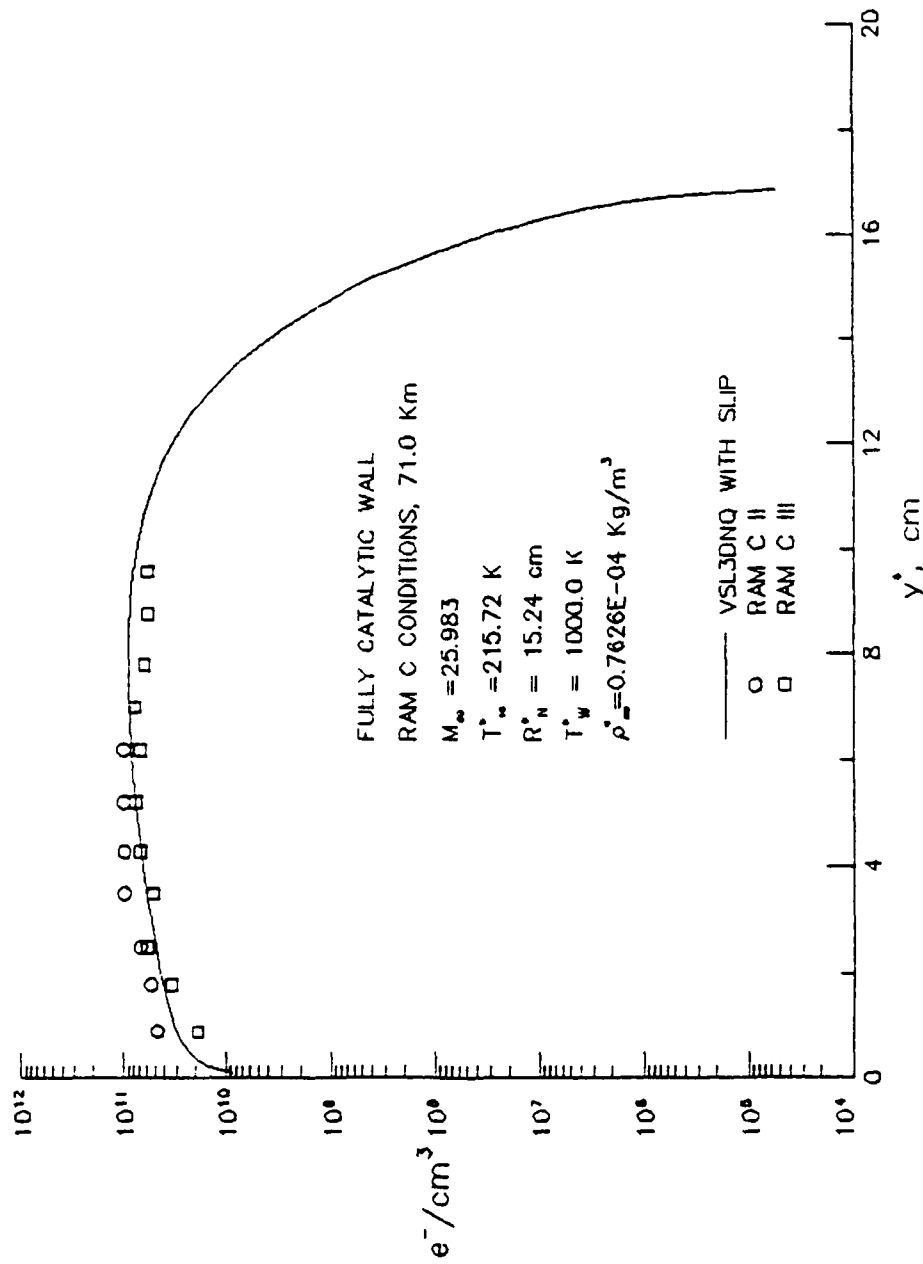


Figure 28. COMPARISON OF ELECTRON NUMBER DENSITY DISTRIBUTION AT $s=8.8$ FOR
A 9° SPHERE-CONE BETWEEN NUMERICAL AND EXPERIMENTAL VALUES FOR
RAM C CONDITIONS

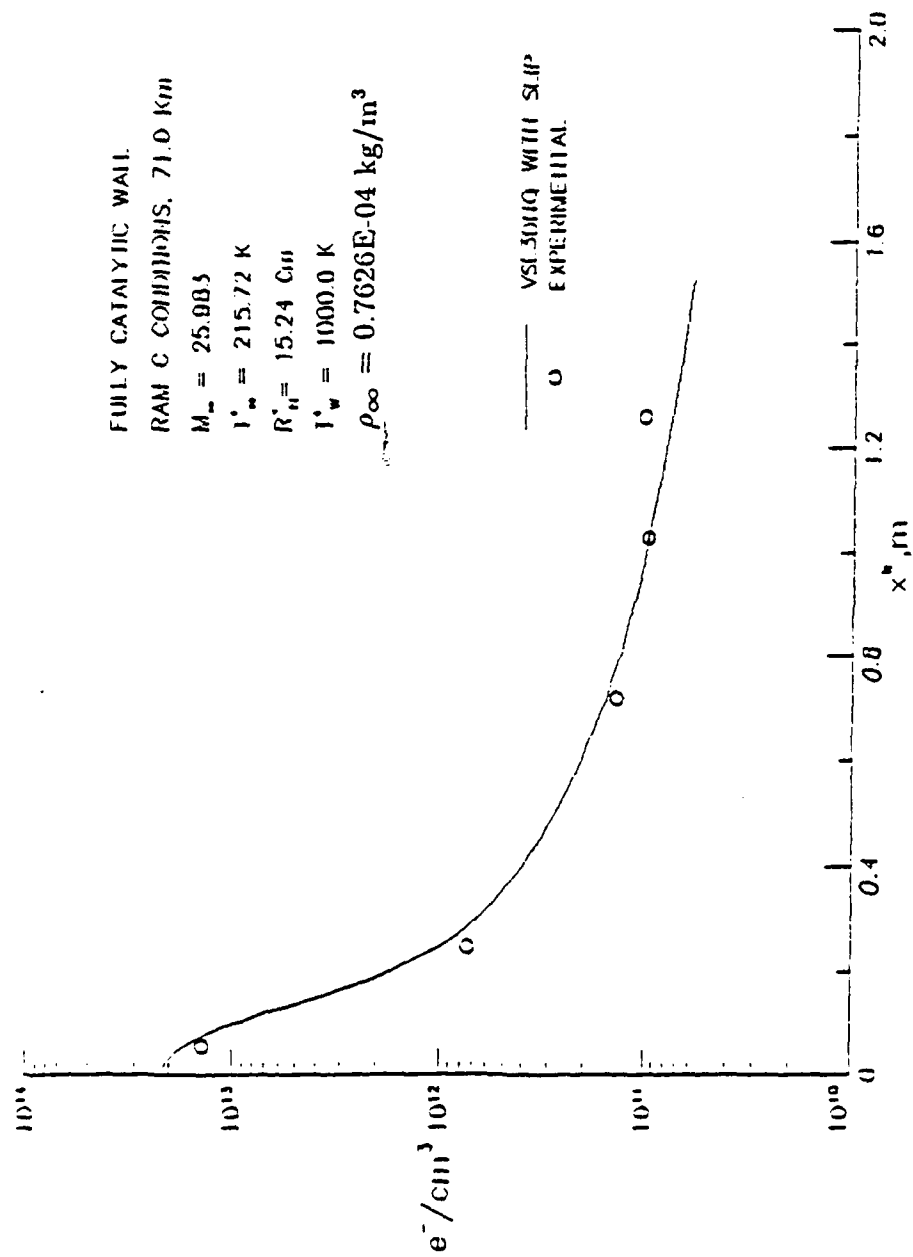


Figure 29. COMPARISON OF PEAK ELECTRON NUMBER DENSITIES WITHIN THE SHOCK LAYER ALONG A 9° SPHERE-CONE BETWEEN NUMERICAL AND EXPERIMENTAL VALUES FOR RAM C CONDITIONS

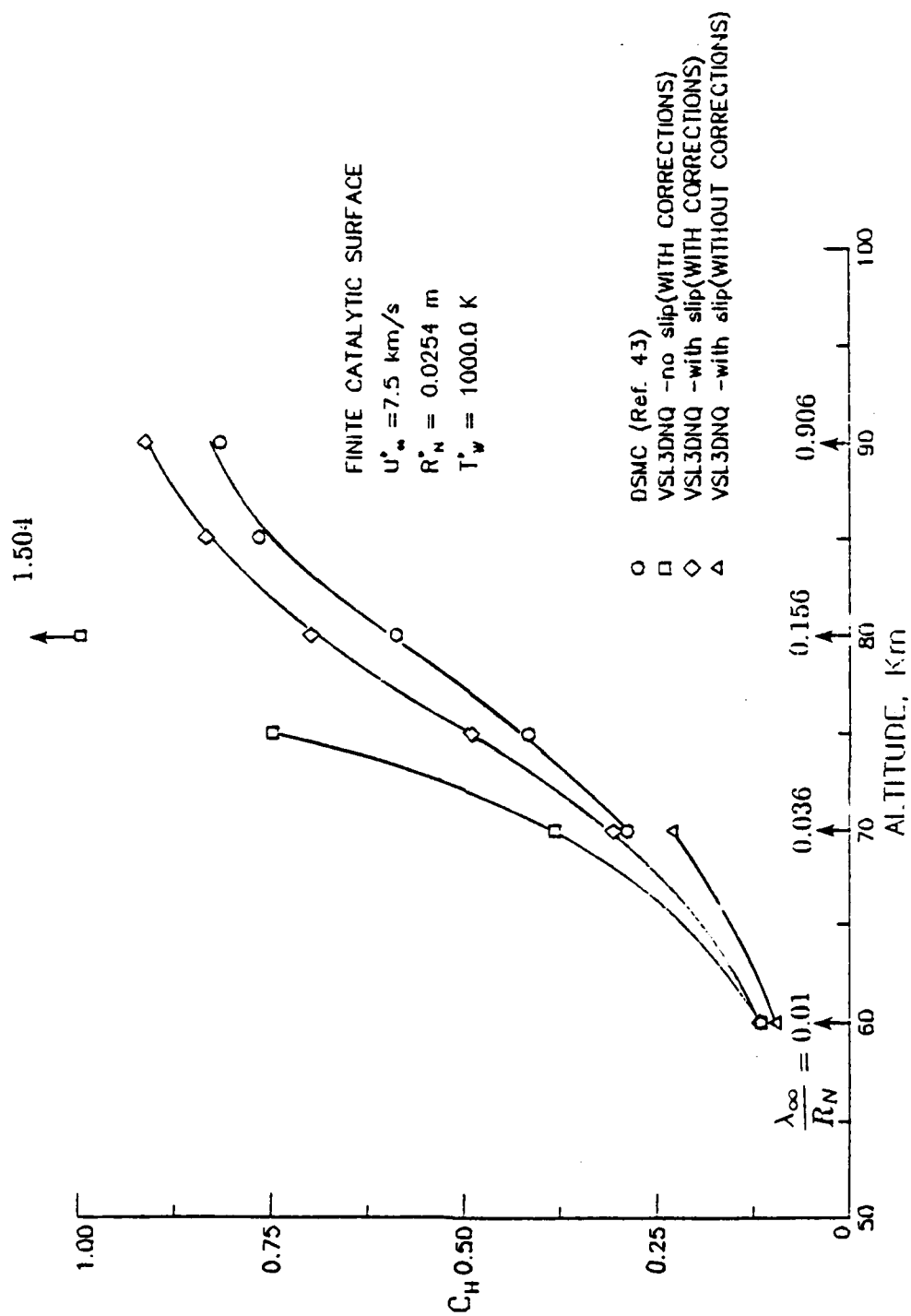


Figure 30. COMPARISON OF SURFACE HEAT TRANSFER COEFFICIENT AT DIFFERENT ALTITUDES FOR A 5° BLUNTED CONE WITH DIRECT SIMULATION MONTE CARLO METHOD

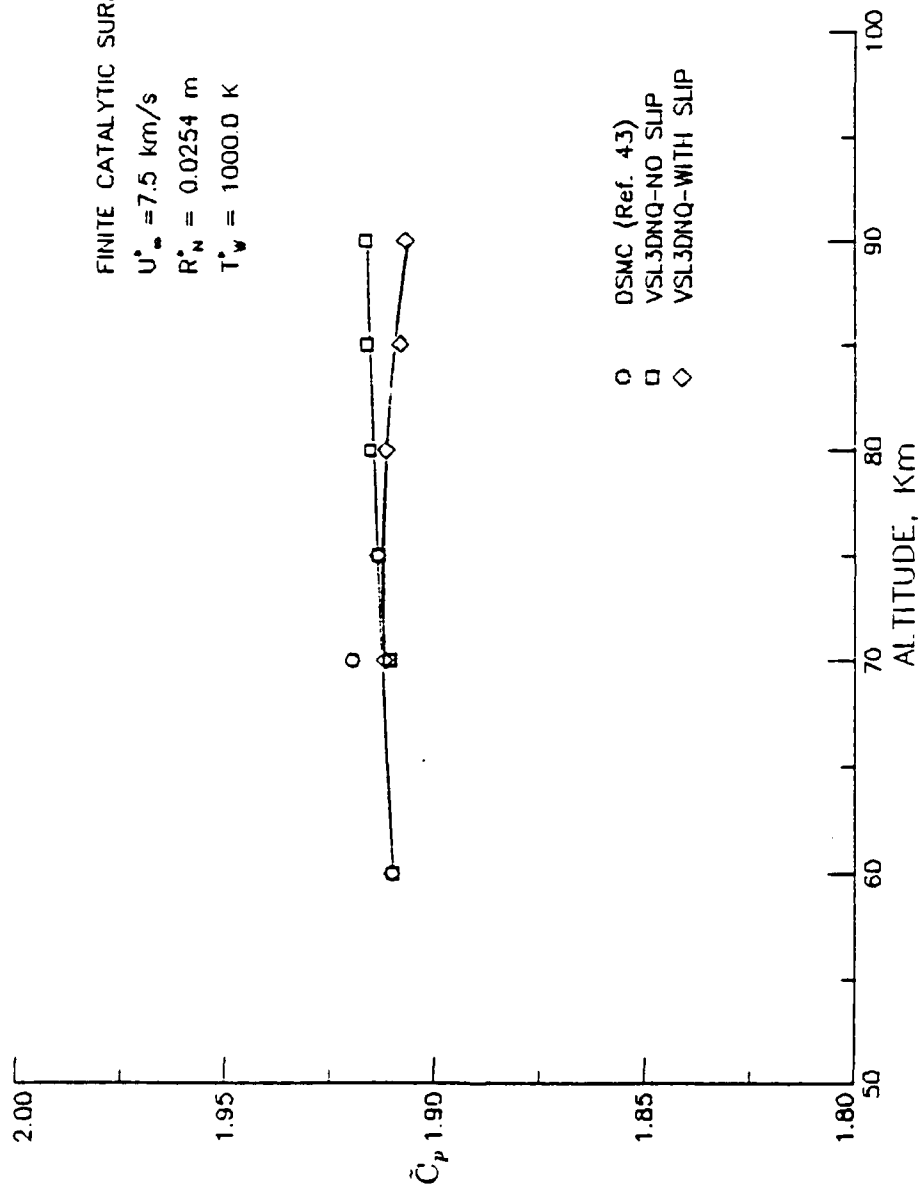


Figure 31. COMPARISON OF SURFACE PRESSURE COEFFICIENT AT DIFFERENT ALTITUDES FOR A 5° BLUNTED CONE WITH DIRECT SIMULATION MONTE CARLO METHOD

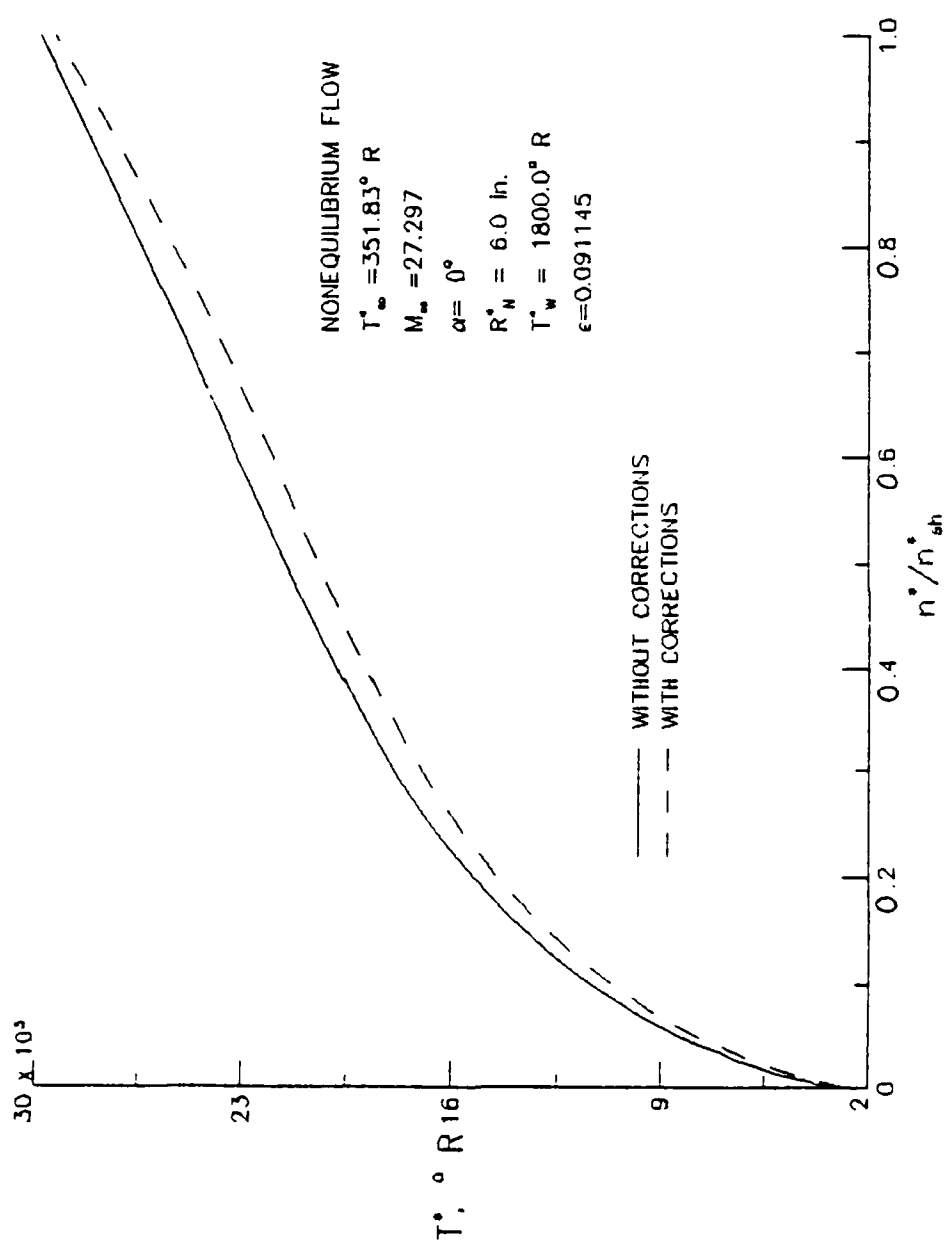


Figure 32. COMPARISON OF STAGNATION REGION TEMPERATURE PROFILES (WITH SLIP)

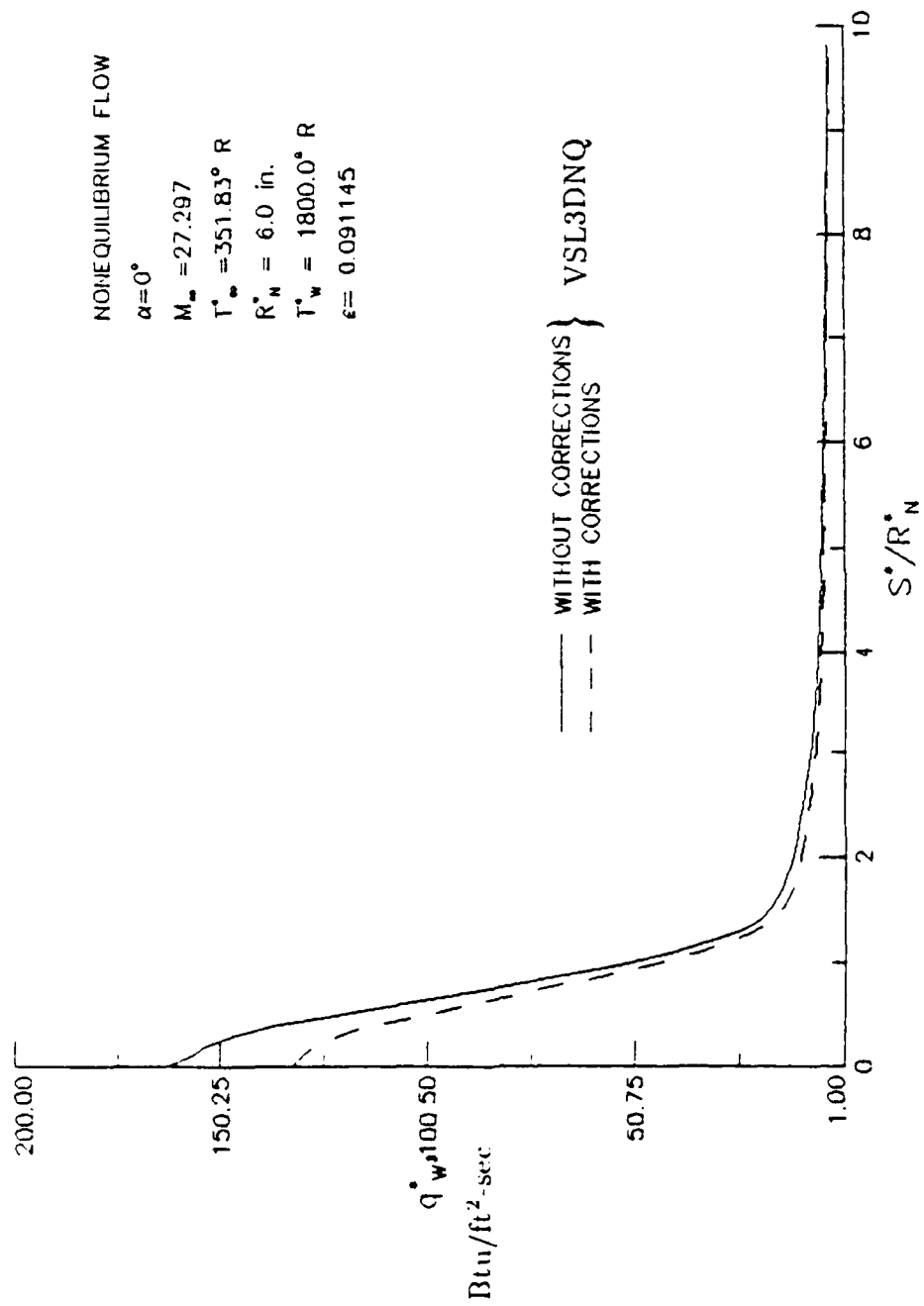


Figure 33. COMPARISON OF SURFACE HEAT TRANSFER DISTRIBUTION FOR A 9° SPHERE-CONE (WITH SLIP)

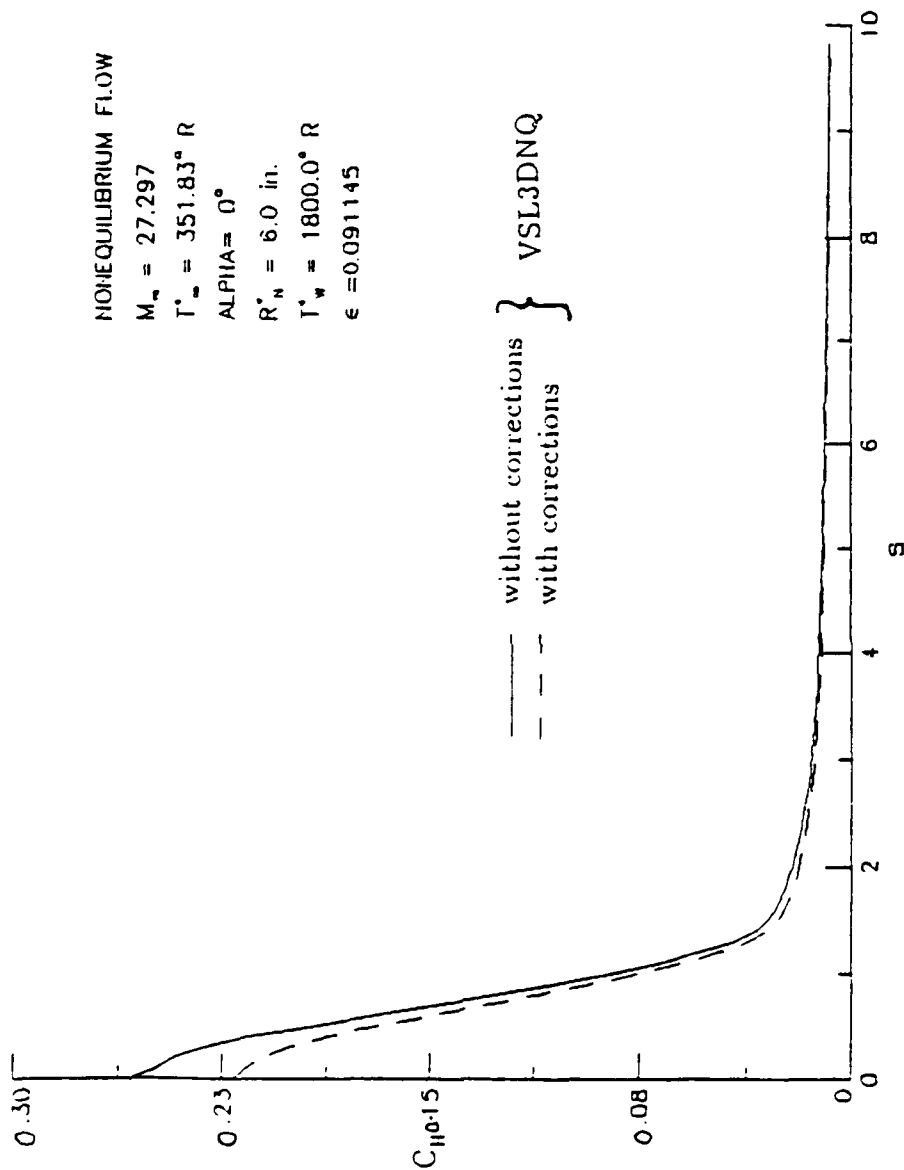


Figure 34. COMPARISON OF SURFACE HEAT TRANSFER COEFFICIENT FOR A 9° SPHERE-CONE (WITH SLIP)

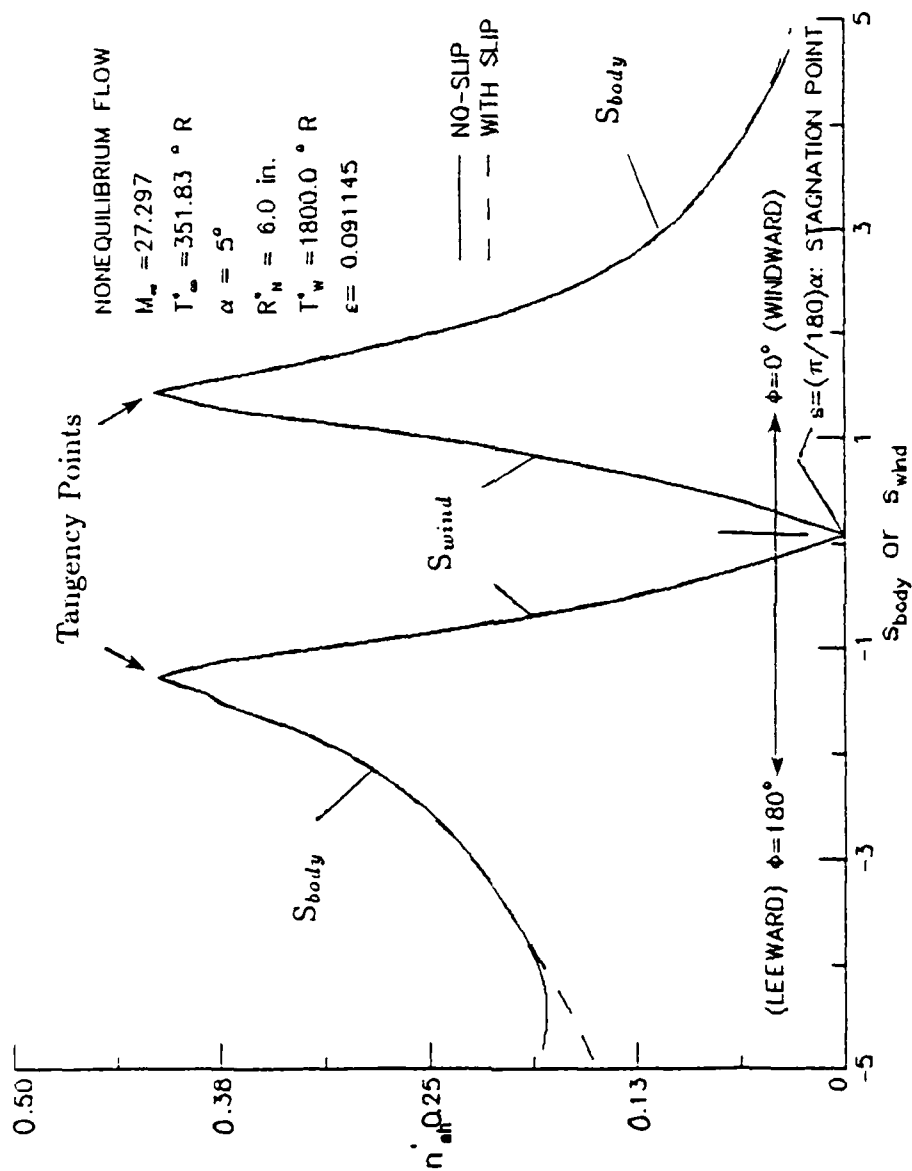


Figure 35. COMPARISON OF SHOCK LAYER THICKNESS GRADIENT FOR A 9° SPHERE-CONE WITH AND WITHOUT SLIP

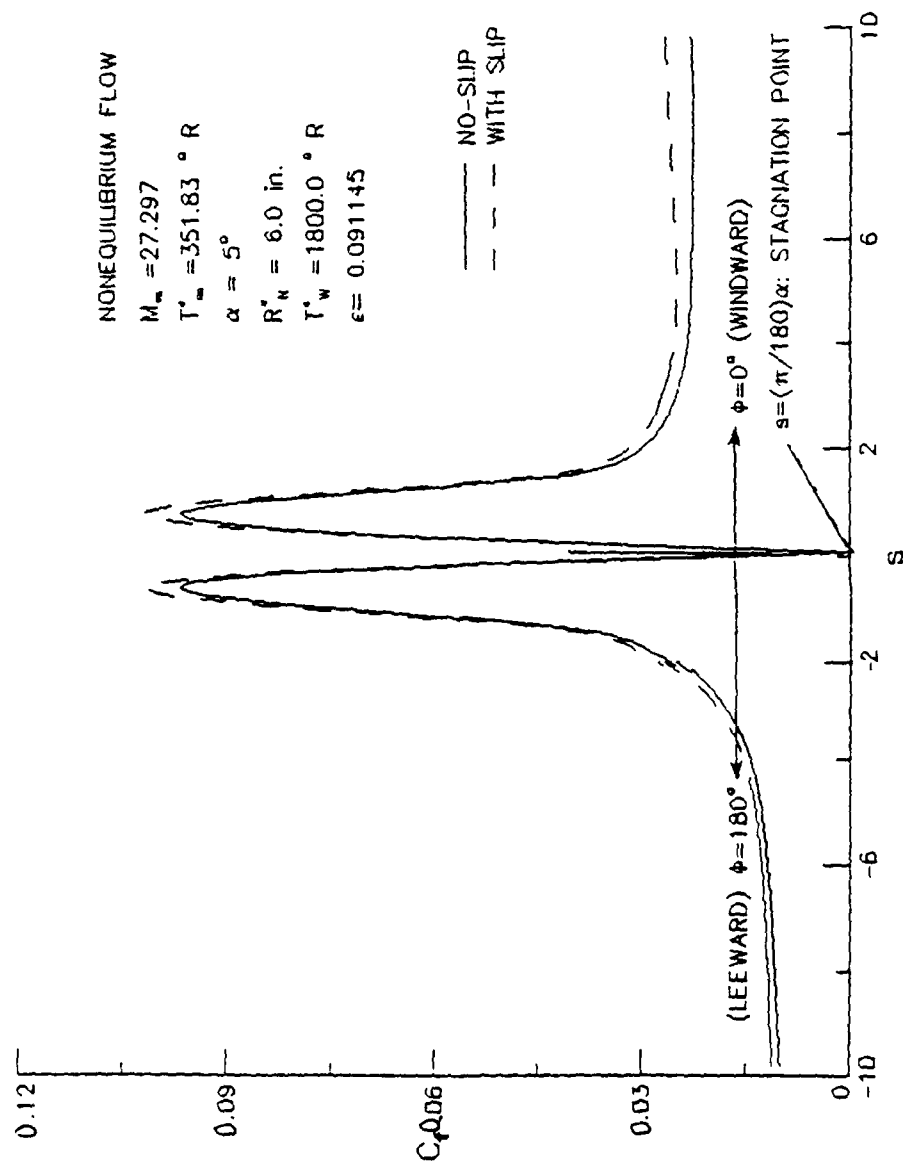


Figure 36 . COMPARISON OF SKIN-FRICTION COEFFICIENT FOR A 9°
 SPHERE-CONE WITH AND WITHOUT SLIP

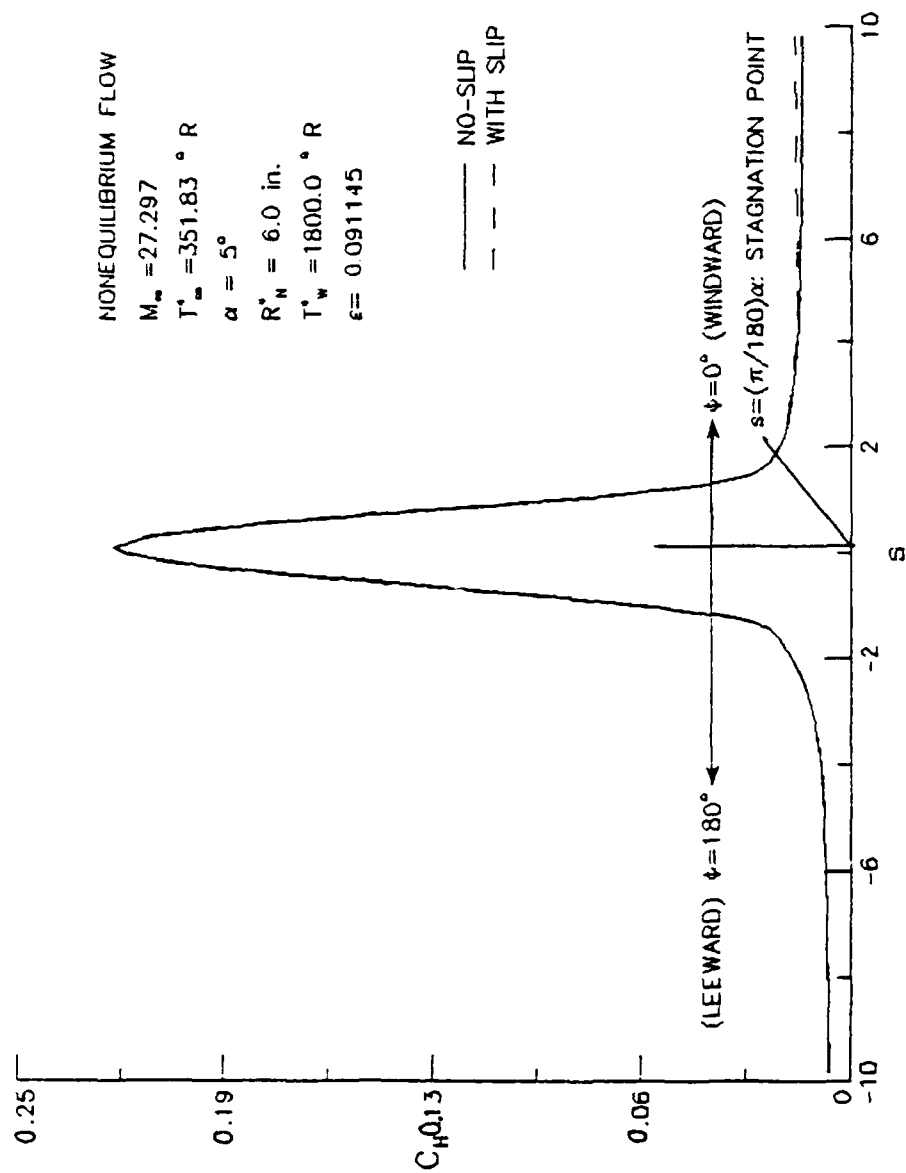


Figure 37 . COMPARISON OF HEAT TRANSFER COEFFICIENT FOR A 9°
 SPHERE-CONE WITH AND WITHOUT SLIP

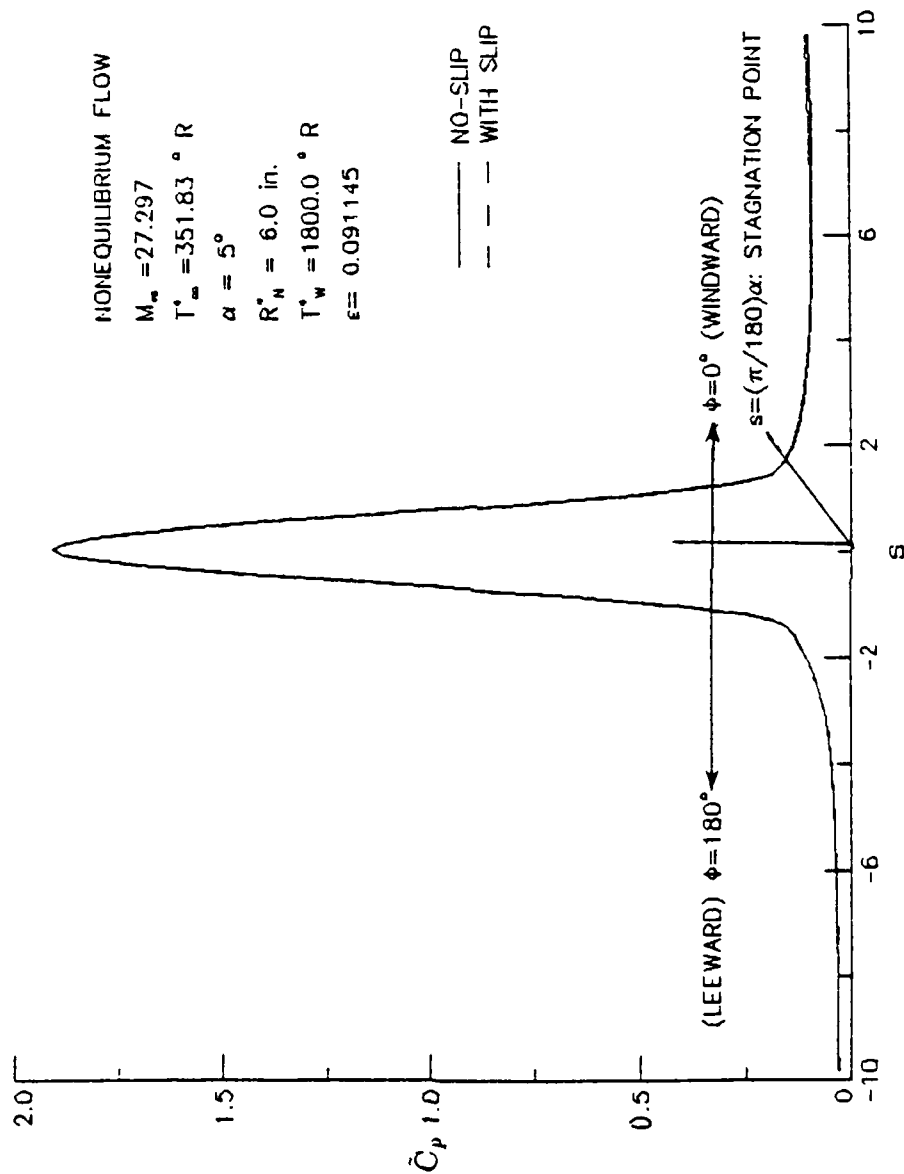


Figure 38 . COMPARISON OF SURFACE PRESSURE COEFFICIENT FOR A 9°
 SPHERE-CONE WITH AND WITHOUT SLIP

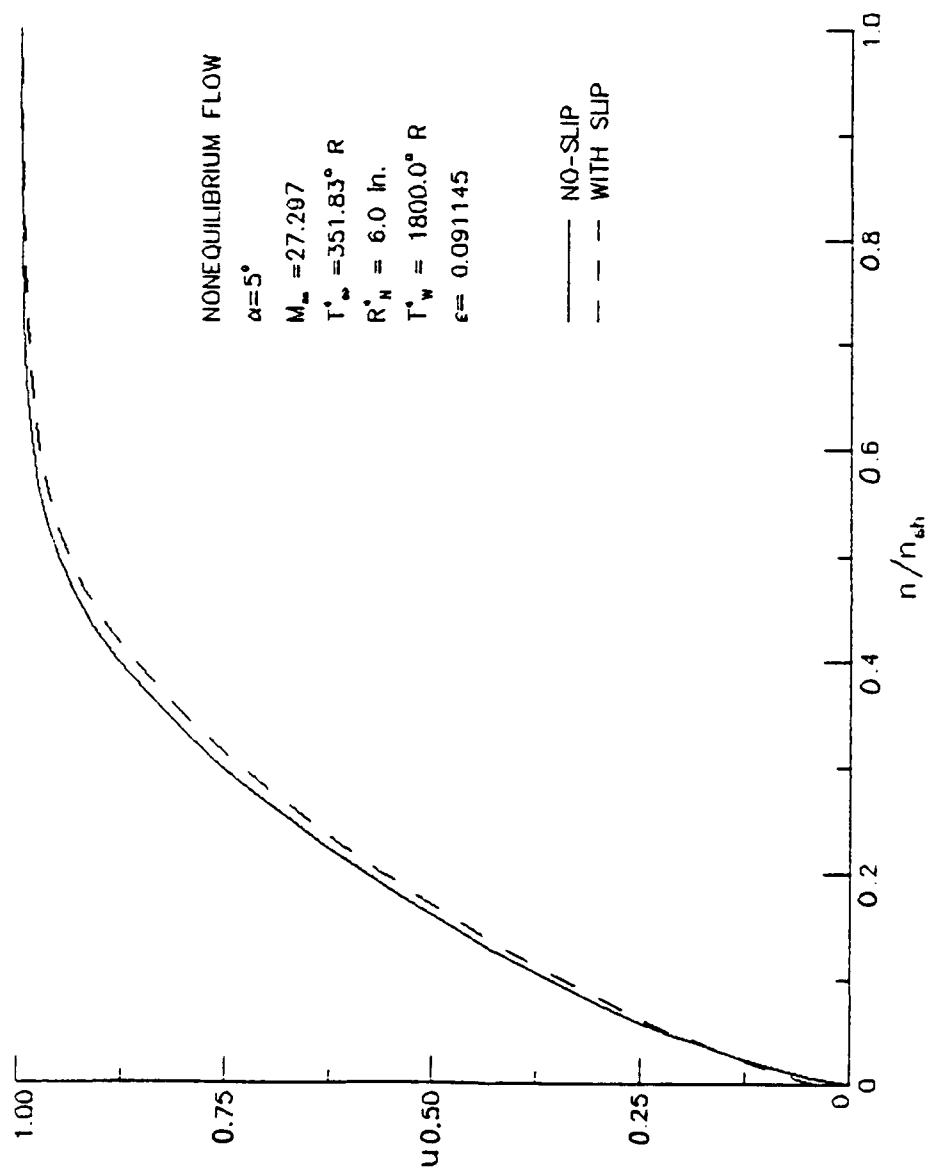


Figure 39. COMPARISON OF STREAMWISE VELOCITY DISTRIBUTION FOR A 9° SPHERE-CONE AT $a=8.8$ WITH AND WITHOUT SLIP FOR $\phi=0^\circ$

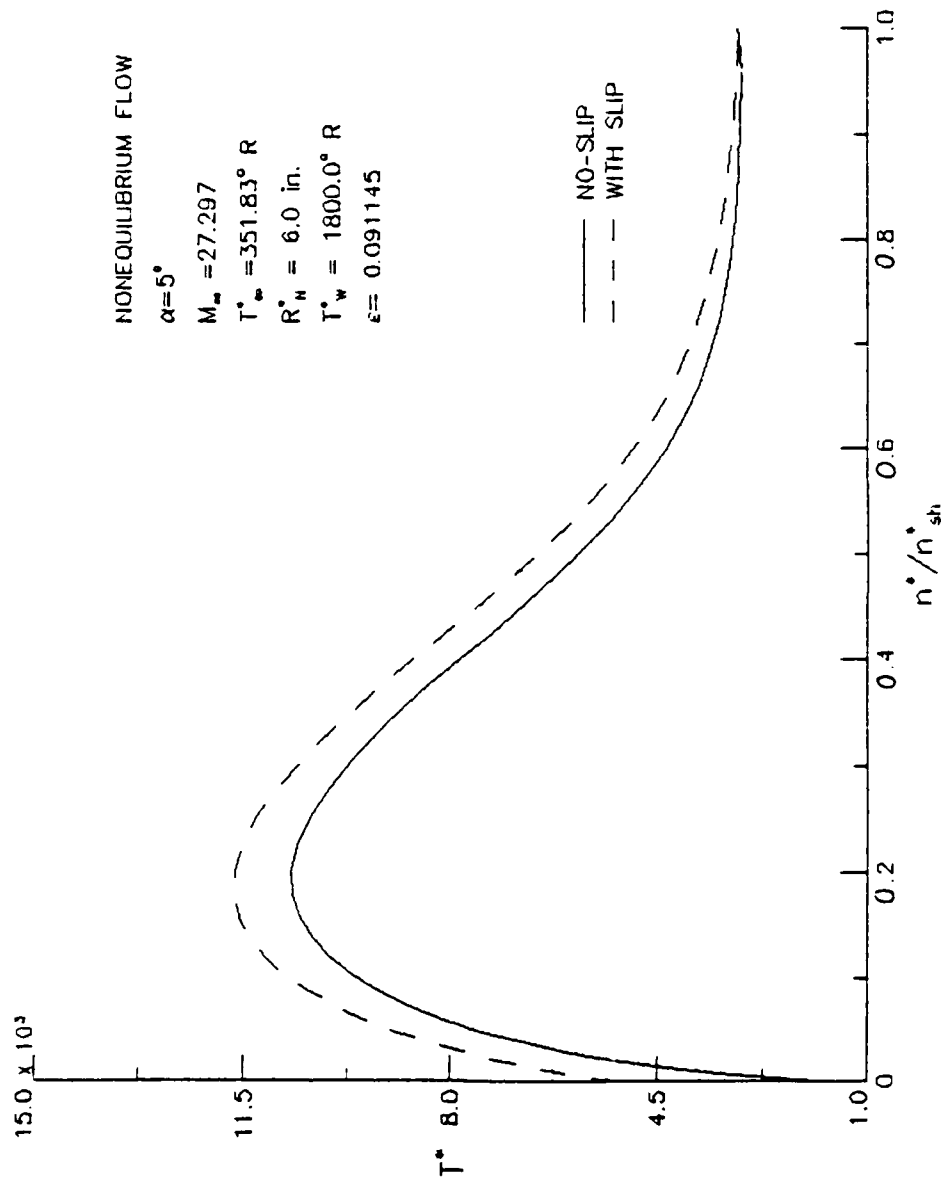


Figure 40. COMPARISON OF TEMPERATURE DISTRIBUTION FOR A 9° SPHERE-CONE
AT $\epsilon=8.8$ WITH AND WITHOUT SLIP FOR $\phi=0^\circ$

NONEQUILIBRIUM FLOW

$$\alpha = 5^\circ$$

$$M_\infty = 27.297$$

$$T_\infty^* = 351.83^\circ \text{ R}$$

$$R_N^* = 6.0 \text{ in.}$$

$$T_w^* = 1800.0^\circ \text{ R}$$

$$\epsilon = 0.091145$$

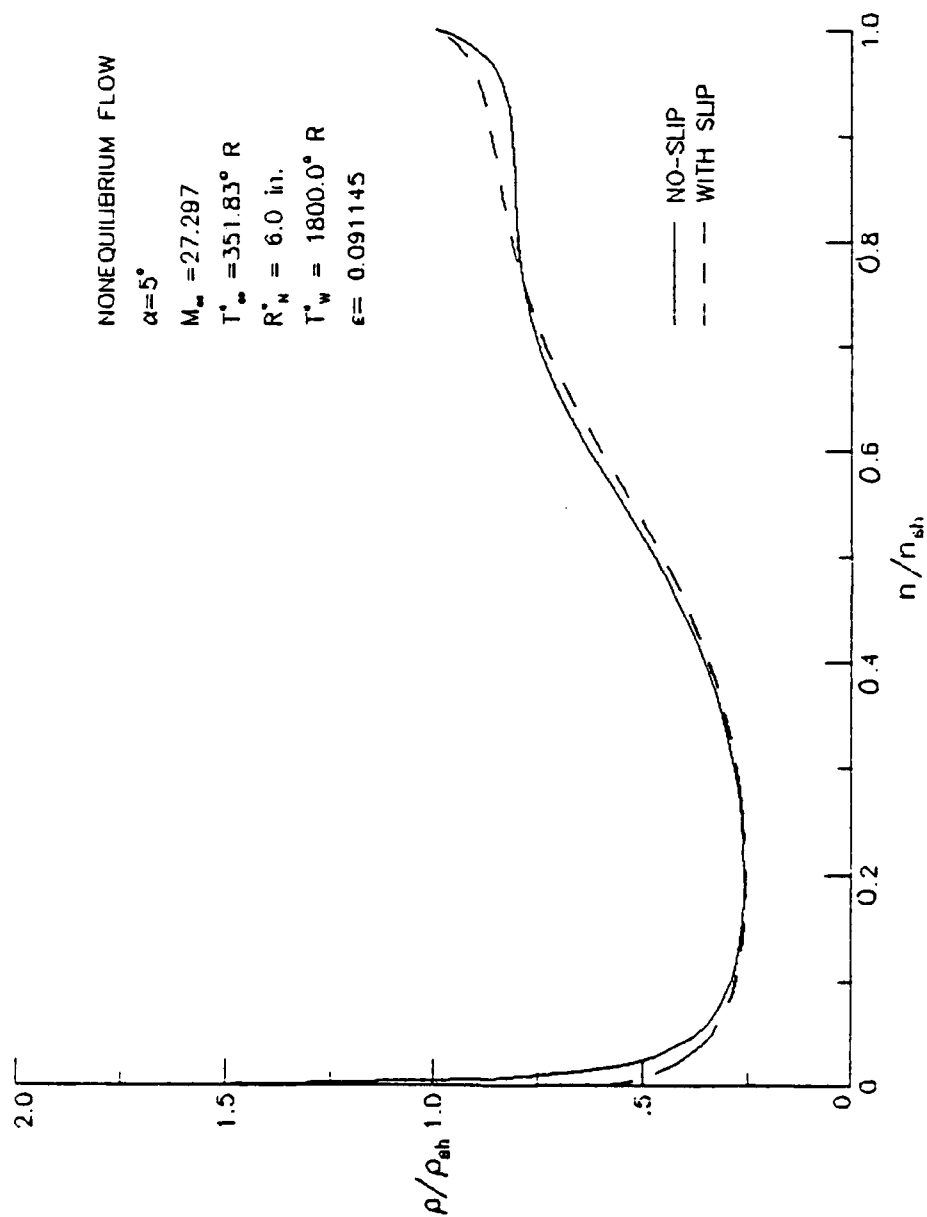


Figure 41. COMPARISON OF DENSITY DISTRIBUTION FOR A 9° SPHERE-CONE
AT $a=8.8$ WITH AND WITHOUT SLIP FOR $\phi=0^\circ$

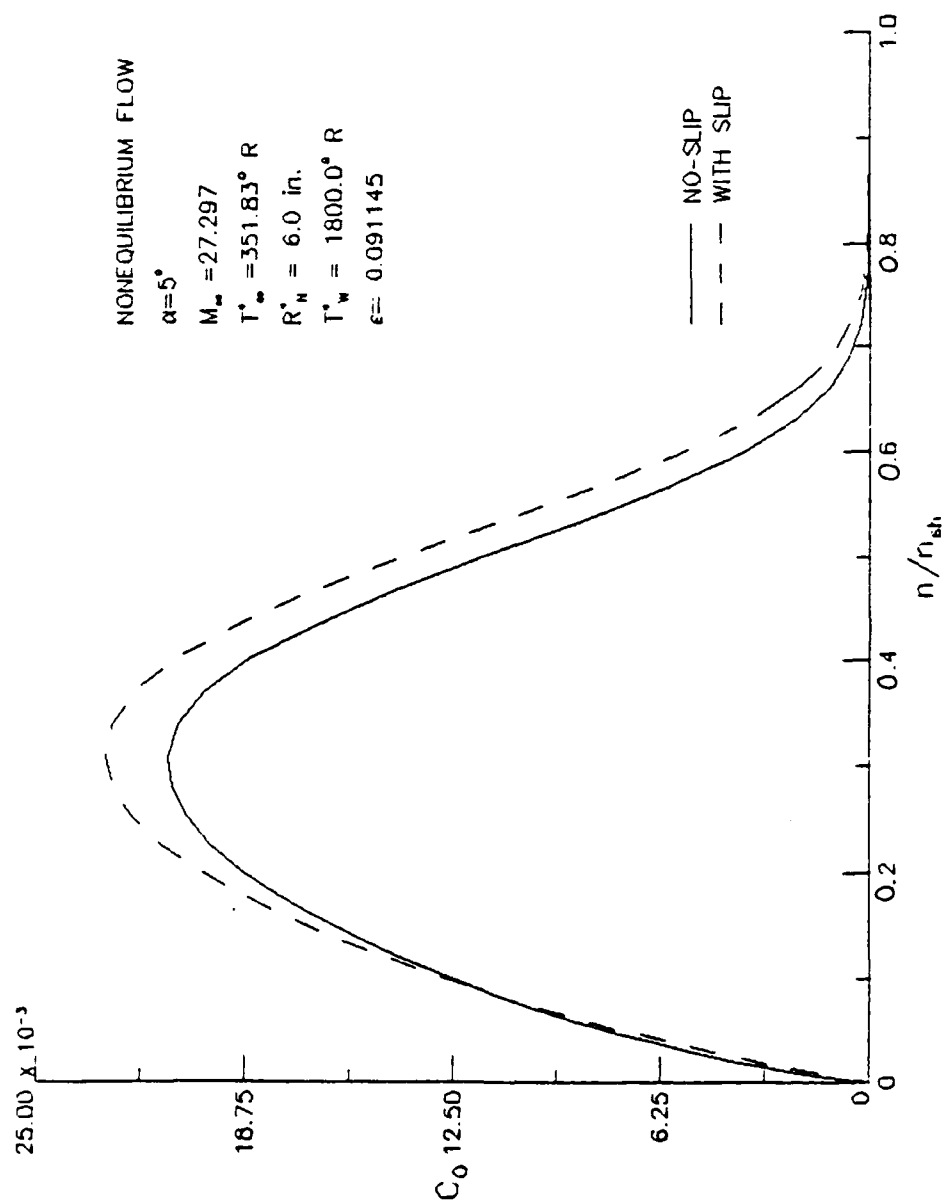


Figure 42. COMPARISON OF MASS FRACTION DISTRIBUTION FOR ATOMIC OXYGEN FOR
 A 9° SPHERE-CONE AT $\alpha = 8.8$ WITH AND WITHOUT SLIP FOR $\phi = 0$

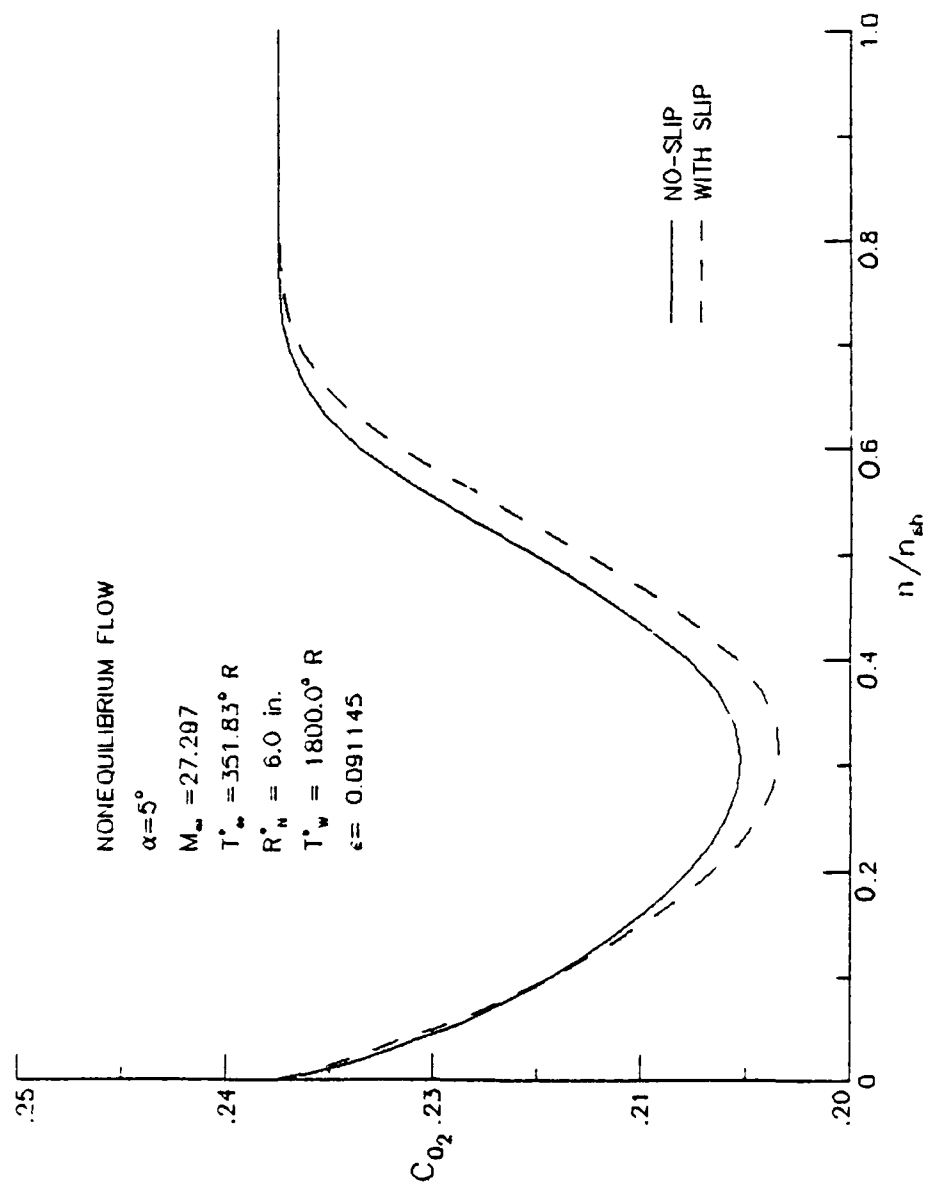


Figure 43. COMPARISON OF MASS FRACTION DISTRIBUTION FOR MOLECULAR OXYGEN FOR
 A 9° SPHERE-CONE AT $a=8.8$ WITH AND WITHOUT SLIP FOR $\phi=0$

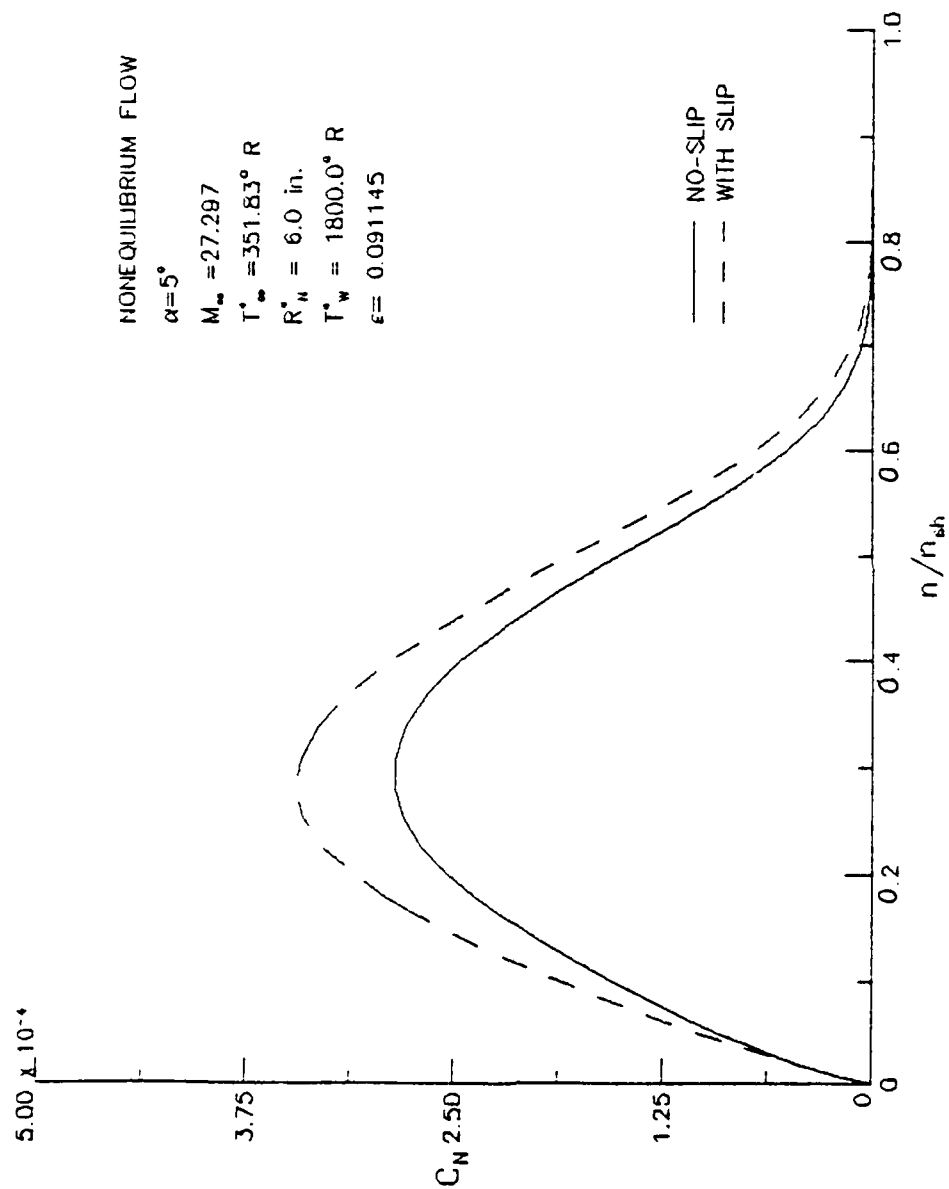


Figure 44. COMPARISON OF MASS FRACTION DISTRIBUTION FOR ATOMIC NITROGEN FOR
A 9° SPHERE-CONE AT $a=8.8$ WITH AND WITHOUT SLIP FOR $\phi=0$

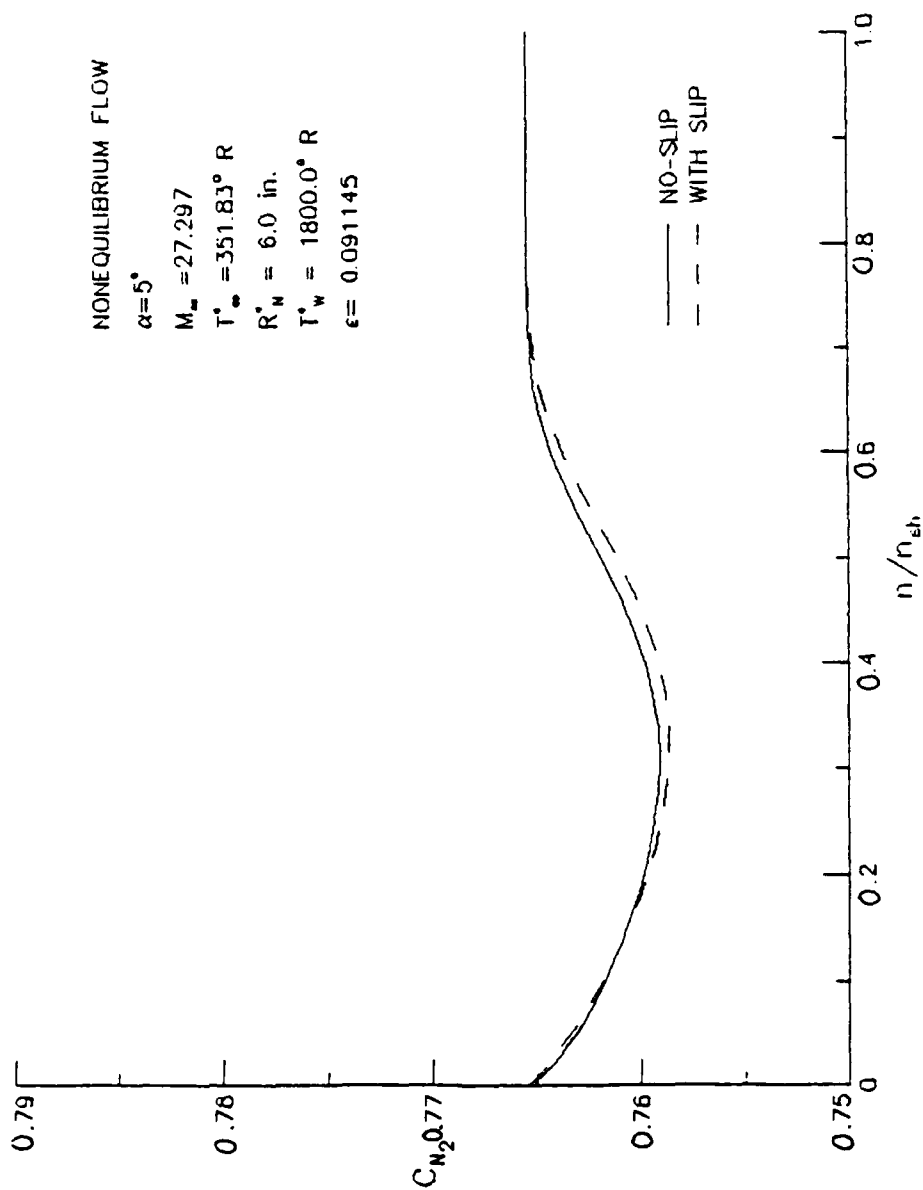


Figure 45. COMPARISON OF MASS FRACTION DISTRIBUTION FOR MOLECULAR NITROGEN
FOR A 9° SPHERE-CONE AT $\epsilon=8.8$ WITH AND WITHOUT SLIP FOR $\phi=0$

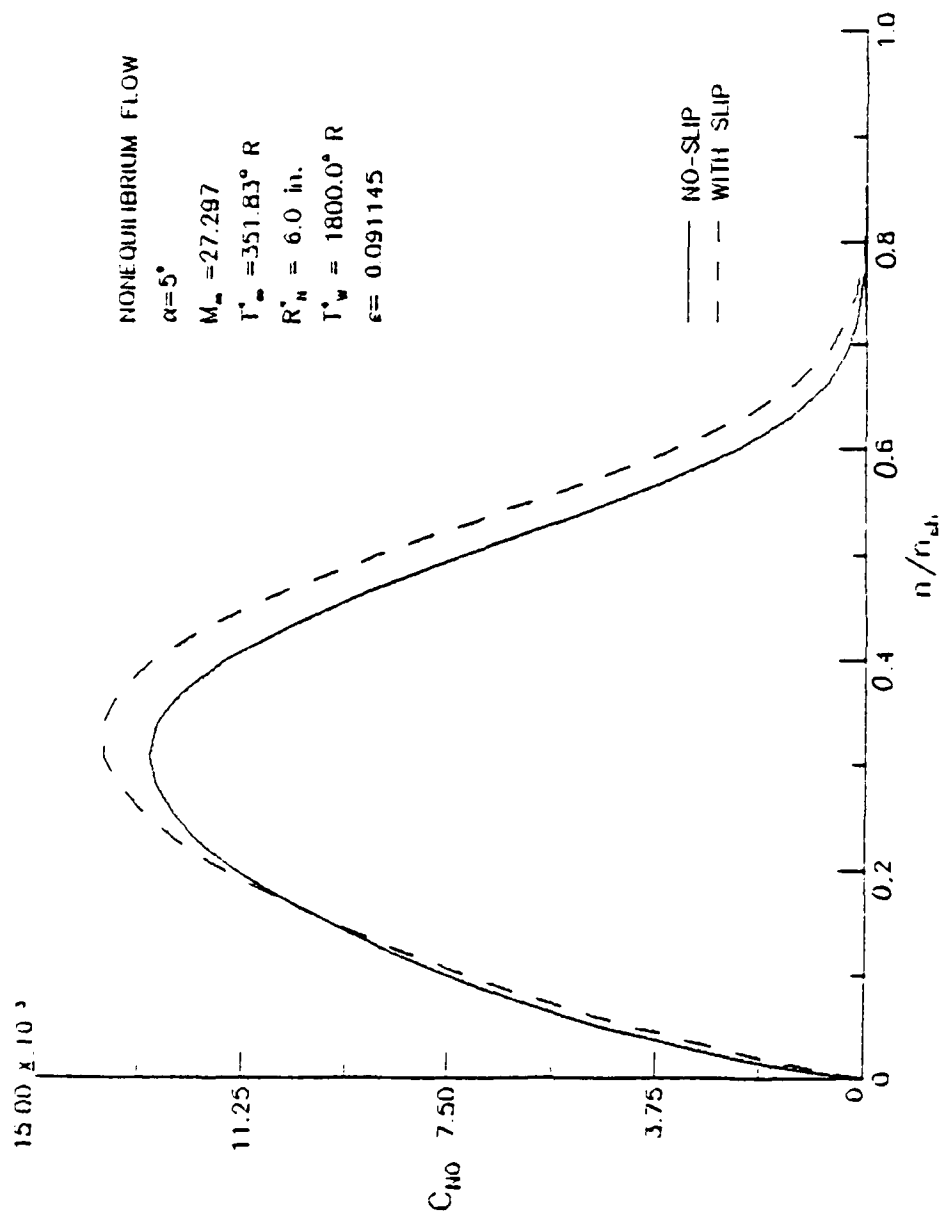


Figure 46. COMPARISON OF MASS FRACTION DISTRIBUTION FOR NITROGEN OXIDE FOR A
 9° SPHERE-CONE AT $\alpha=8.8$ WITH AND WITHOUT SLIP FOR $\phi=0$

END